



Umberto Cassará de Castellammare Scott Siciliano

**Exploring the Influence of High Temperature and
Pressure on Geopolymer Properties**

Tese de Doutorado

Thesis presented to the Programa de Pós-Graduação em Engenharia Civil of PUC-Rio in partial fulfillment of the requirements for the degree of Doutor em Ciências – Engenharia Civil.

Advisor: Prof. Flávio de Andrade Silva

Co-advisor: Dr. Ana Carolina Constâncio Trindade

Rio de Janeiro
February 2024



Umberto Cassará de Castellammare Scott Siciliano

**Exploring the Influence of High Temperature and
Pressure on Geopolymer Properties**

Thesis presented to the Programa de Pós-Graduação em Engenharia Civil of PUC-Rio in partial fulfillment of the requirements for the degree of Doutor em Ciências – Engenharia Civil. Approved by the Examination Committee.

Prof. Flávio de Andrade Silva

Advisor

Civil and Environmental Engineering Department – PUC-Rio

Dr. Ana Carolina Constâncio Trindade

Co-advisor

Department of Biosystems Engineering - USP

Prof. Lourdes Maria Silva de Souza

Civil and Environmental Engineering Department – PUC-Rio

Prof. Antonio Acacio de Melo Neto

Civil Engineering Department - UFPE

Prof. João Claudio Bassan de Moraes

Civil Engineering Division - ITA

Prof. João Adriano Rossignolo

Department of Biosystems Engineering - USP

Rio de Janeiro, February 19th, 2024

All rights reserved. Total or partial reproduction of the work without the authorization of the university, author and advisors is prohibited.

Umberto Cassará de Castellammare Scott Siciliano

Undergrad in Metallurgical Engineering at Universidade Federal do Rio de Janeiro in 2014 and obtained the M.Sc degree in Nuclear Science and Technology from the Comissão Nacional de Energia Nuclear in 2017.

Bibliographic data

Siciliano, Umberto Cassará de Castellammare Scott

Exploring the influence of high temperature and pressure on geopolymer properties / Umberto Cassará de Castellammare Scott Siciliano ; advisor: Flávio de Andrade Silva ; co-advisor: Ana Carolina Constâncio Trindade. – 2024.

155 f. : il. color. ; 30 cm

Tese (doutorado)–Pontifícia Universidade Católica do Rio de Janeiro, Departamento de Engenharia Civil e Ambiental, 2024.
Inclui bibliografia

1. Engenharia Civil e Ambiental - Teses. 2. Geopolímero. 3. Metacaulim. 4. Pressão. 5. Temperatura. 6. Adições híbridas. I. Silva, Flávio de Andrade. II. Trindade, Ana Carolina Constâncio. III. Pontifícia Universidade Católica do Rio de Janeiro. Departamento de Engenharia Civil e Ambiental. IV. Título.

CDD: 624

For my grandmother, Maria Helena Scott Siciliano.
(in memoriam)

Acknowledgments

This study was financed in part by the Coordenação de Aperfeiçoamento de Pessoal de Nível Superior – Brasil (CAPES) – Finance Code 001.

To PUC-Rio, for the support granted, without which this work could not have been carried out.

I would like to express my gratitude to the advisor, Prof. Flávio de Andrade Silva, for the opportunity granted and for all the scientific contribution given to this thesis and also to co-advisor, Ana Carolina Constâncio Trindade, for the knowledge shared and all the time spent to help me.

To the entire Laboratory of Structures and Materials team, especially the technical support provided by: Anderson, Euclides, Jhanssen, José Nilson, Marques and Rogério. Also thank the laboratory team of the Rock Mechanics Laboratory at PUC-Rio: Alexandr, Bruno, Gabriel, Larissa and Victor.

I would like to thank the members of other PUC-Rio laboratories who contributed with analyses: Prof. Roberto Avillez and Prof. Sonia Letichevsky from the Department of Chemical and Materials Engineering (DEQM); Ana Maria Percebom from Macromolecules & Nanoparticles Laboratory (M&N Lab); Dr. Eliana Marín from the Rheology Group (GRéo).

Other partnerships external to PUC-Rio for the technical support: Luis Mantovano, from Materials and Chemistry Technology Service at the Nuclear Engineering Institute of the Nuclear Energy Commission (CNEN); Otávio da Fonseca Martins Gomes and Hudson Jean Bianquini Couto, from Mineral Technology Center (CETEM) and; Prof. Renata Simão from the Department of Metallurgical and Materials Engineering at the Federal University of Rio de Janeiro (UFRJ).

I also thank Jitong Zhao for the partnership research and analysis done at TU Dresden.

I would like to thank the Professors who participated in this thesis committee.

For the friendships shown over all these years, from: Allonso Curty, Igor Freitas, Juliana Xavier, Lívia Schabude, Marco Antônio and Monica Miguelote.

Special thanks to my parents, siblings and nephews.

Abstract

Cassará de Castellammare Scott Siciliano, Umberto; de Andrade Silva, Flávio (advisor). Constâncio Trindade, Ana Carolina (advisor). **Exploring the Influence of High Temperature and Pressure on Geopolymer Properties**. Rio de Janeiro, 2024. 155 p. Tese de Doutorado – Departamento de Engenharia Civil e Ambiental, Pontifícia Universidade Católica do Rio de Janeiro.

Geopolymers (GPs), classified as polysilicate-aluminates, represent inorganic polymers or chemically bonded ceramics with diverse applications determined by the Si:Al atomic ratio, including: fire-resistant components, sealants, mortar for reinforcing beams and oil well plugging. The exploration of GPs under varying temperature and/or pressure conditions gained momentum post-2001. The addition of chamotte into GP formulation only occurred in 2014, followed by subsequent investigations into the impact of adding carbon nanotubes and nanoclay a year later. The primary objective of this thesis was to assess the compressive strength of plain potassium-based GP cured at temperatures and pressures of up to 200°C and 70 MPa, respectively. This evaluation included comparative analysis with microstructural characterizations such as porosimetry and thermogravimetry. Initially, the study evaluated the reaction mechanisms of different GP formulations and determined the effects of alkali leaching on strength evolution under diverse curing conditions (dry and saturated). The results identified the K-waterglass composition with $\text{SiO}_2/\text{K}_2\text{O}=1.53$ and $\text{H}_2\text{O}/\text{K}_2\text{O}=8.69$ as presenting rapid strength gain, low leachability, and was thus selected. Curing temperature significantly impacted on the final properties, demonstrating a notable 144% improvement in compressive strength at 50°C, and an additional 37% improvement at 50°C under 20 MPa, attributed to enhanced microstructural densification. The thesis also explored the effect of adding micrometric (chamotte) and nanometric (nanometakaolin, nanoclay and carbon nanotubes) particles under extreme curing conditions (150°C and 40 MPa). Preliminary results indicated satisfactory

dispersion of carbon nanotubes using a simple, low-energy technique. Individual additions contributed to GP performance improvement, yet hybrid additions surpassed any separate addition results, yielding a formulation with enhanced reactivity. Under 150°C curing, GP with hybrid additions exhibited a remarkable 350% improvement in mechanical properties compared to plain GP. Under 40 MPa pressure, the mechanical performance was minimally affected by hybrid additions, confirming their efficacy in achieving the desired properties for high-temperature and pressure applications, including pore refinement, increased flexural strength, and reduced porosity.

Keywords

Geopolymer; Metakaolin; Pressure; Temperature; Hybrid additions.

Resumo

Cassará de Castellammare Scott Siciliano, Umberto; de Andrade Silva, Flávio (orientador). Constâncio Trindade, Ana Carolina (orientadora). **Explorando a influência de altas temperaturas e pressão nas propriedades de geopolímeros**. Rio de Janeiro, 2024. 155 p. Tese de Doutorado – Departamento de Engenharia Civil e Ambiental, Pontifícia Universidade Católica do Rio de Janeiro.

Geopolímeros (GPs), classificados como polissilicatos-aluminatos, representam polímeros inorgânicos ou cerâmicas quimicamente ligadas com diversas aplicações determinadas pela razão atômica Si:Al, incluindo: componentes resistentes ao fogo, selantes, argamassa para reforço de vigas e tamponamento de poços de petróleo. A exploração de GPs sob condições variadas de temperatura e/ou pressão ganhou impulso após 2001. A adição de chamotte à formulação GP ocorreu apenas em 2014, seguida de investigações subsequentes sobre o impacto da adição de nanotubos de carbono e nanoargila um ano depois. O objetivo principal desta tese foi avaliar a resistência à compressão do GP simples à base de potássio curado em temperaturas e pressões de até 200°C e 70 MPa, respectivamente. Esta avaliação incluiu análises comparativas com caracterizações microestruturais como porosimetria e termogravimetria. Inicialmente, o estudo avaliou os mecanismos de reação de diferentes formulações de GP e determinou os efeitos da lixiviação alcalina na evolução da resistência sob diversas condições de cura (seca e saturada). Os resultados identificaram a composição K-waterglass com $\text{SiO}_2/\text{K}_2\text{O}=1,53$ e $\text{H}_2\text{O}/\text{K}_2\text{O}=8,69$ como apresentando rápido ganho de resistência, baixa lixiviabilidade, e por isso foi selecionada. A temperatura de cura teve um impacto significativo nas propriedades finais, com demonstrando uma melhoria notável de 144% na resistência à compressão a 50°C, e uma melhoria adicional de 37% a 50°C sob 20 MPa, atribuída à maior densificação microestrutural. A tese também explorou o efeito da adição de partículas micrométricas (chamotte) e nanométricas (nanomemetacaulim, nanoargila e nanotubos de carbono) sob condições extremas

de cura (150°C e 40 MPa). Resultados preliminares indicaram dispersão satisfatória de nanotubos de carbono usando uma técnica simples e de baixa energia. As adições individuais contribuíram para a melhoria do desempenho do GP, mas as adições híbridas superaram quaisquer resultados de adição separada, produzindo uma formulação com maior reatividade. Sob a cura a 150°C, o GP com adições híbridas exibiu uma melhoria notável de 350% nas propriedades mecânicas em comparação com o GP simples. Sob pressão de 40 MPa, o desempenho mecânico foi minimamente afetado pelas adições híbridas, confirmando sua eficácia em alcançar as propriedades desejadas para aplicações de alta temperatura e pressão, incluindo refinamento de poros, aumento de resistência à flexão e redução de porosidade.

Palavras-chave

Geopolímero; Metacaulim; Pressão; Temperatura; Adições híbridas.

Table of contents

Abstract	6
Resumo	8
Table of contents	10
List of figures	14
List of tables	19
1. Introduction	22
1.1. Goals	24
1.2. Thesis organization	24
1.3. References	25
2. Literature review	27
2.1. Geopolymers	27
2.2. Geopolymer vs Other Materials	28
2.3. Aluminosilicate Sources	29
2.4. Geopolymer Design	31
2.5. Curing Conditions	33
2.5.1. Temperature Effect	34
2.5.2. Pressure Effect	36
2.5.3. Coupled Effect of Temperature and Pressure	36
2.6. Particulate Reinforcement Use	37
2.6.1. Microparticles	37
2.6.2. Nanoparticles	38
2.7. Literature Findings	41
2.8. Applications	47

	11
2.9. References	49
3. Potassium-waterglass (K-WG) Influence on Geopolymer Strength Development & Leaching in Different Curing Environments	59
3.1. Introduction	59
3.2. Experimental Program	62
3.2.1. Materials and geopolymer design	62
3.2.2 Testing Methods	64
3.2.2.1 Calorimetry	64
3.2.2.2 Non-destructive compressive strength evolution	65
3.2.2.3 pH measurement	66
3.2.2.4 Uniaxial compressive strength	66
3.3 Results and discussions	67
3.3.1 Chemical properties	67
3.3.2. Transient state properties	72
3.3.3. Hardened properties	74
3.4. Conclusions	76
3.5. References	77
4. Influence of Curing Temperature and Pressure on the mechanical and microstructural development of metakaolin-based geopolymers	81
4.1. Introduction	81
4.2. Experimental Program	84
4.2.1. Materials and geopolymer design	84
4.2.2. Testing Methods	87
4.2.2.1. Non-destructive compressive strength evolution	87
4.2.2.2. Autoclave curing	88
4.2.2.3. Uniaxial compressive strength	89
4.2.2.4. Thermal stability	89
4.2.2.5. Porosity	89
4.2.2.6. Morphological analysis	89
4.3. Results and discussions	90
4.3.1. Transient state properties	90

	12
4.3.2. Hardened properties	92
4.3.2.1. Temperature effect	92
4.3.2.2. Pressure effect	94
4.3.2.3. Combination of temperature and pressure effects	95
4.3.2.4. Correlation with sonic strength	97
4.3.4. Thermal Analysis	98
4.3.5. Porosimetry	100
4.3.6. Microstructure	104
4.4. Conclusions	109
4.5. References	110
5. Optimizing high-temperature and pressure performance of metakaolin-based geopolymers through the inclusion of hybrid particulate reinforcements	115
5.1. Introduction	115
5.2. Experimental Program	119
5.2.1. Materials and Alkaline Solution Preparation	119
5.2.2. Mix design and fresh properties	126
5.2.3. Casting	129
5.2.4. Curing	129
5.2.5. Mechanical tests	130
5.2.6. Porosimetry	131
5.2.7. Thermal stability	131
5.2.8. X-ray diffraction analysis	131
5.2.9. Microscopic analyzes	132
5.3. Results and discussions	132
5.3.1. Carbon nanotube dispersion	132
5.3.2. Fresh and transient-state properties	134
5.3.2. Hardened properties	136
5.3.2.1. Additions effect	136
5.3.2.2. Temperature effect	140
5.3.2.3. Pressure effect	143
5.3.2.4. Combination of temperature and pressure effects	145

	13
5.3.3. Microstructure	148
5.4. Conclusions	149
5.5. References	149
6. Conclusions and Suggestions for Future Works	154
6.1. Conclusions	154
6.2. Suggestions for future works	155

List of figures

- Figure 2.1 – Bibliographical production referring to geopolymers over time showing (a) number of total publications and (b) annual production; (c) quantity of work on specific subjects and (d) annual production of specific subjects. (Data extracted by consultation in Periodicals CAPES on December 21, 2023). 42
- Figure 2.2 - Values obtained in the literature for geopolymer, Portland Cement and alkali-activated cement referring to compressive strength after curing (a) at room temperature (21 to 28°C), (b) at temperatures above 50°C, (c) at temperature and pressure and; (d) flexural strength values. 43
- Figure 2.3 - Microstructure obtained in Assaedi et al. [55] for: (a) plain geopolymer; (b) 2 %wt. nanoclay. 46
- Figure 2.4 - Microstructure obtained by Saafi et al. [24] for: (a) plain geopolymer; (b) 0.1 wt.% MWCNTs. 46
- Figure 2.5 - MWCNTs acting as crack bridging with a concentration of (a) 0.3 %wt. and (b) 1.5 %wt. [113]. 47
- Figure 3.1 - (a) Heat flow of different geopolymer compositions as a function of curing time; (b) GP4 polycondensation peak; (c) Heat flux between 3 and 7 days of curing; (d) Cumulative heat for all geopolymers design. 67
- Figure 3.2 - Adjustment by JMAK model for (a) GP1; (b) GP2; (c) GP3; (d) GP4. 69
- Figure 3.3 - Evolution of the compressive strength for all geopolymer formulations obtained from ultrasonic pulse measurements. 72
- Figure 3.4 - Relationship between sonic strength and accumulated heat released for GP4. 73
- Figure 3.5 - Sonic strength data for GP4 adjusted, based on Kamali et al. [28]. 74
- Figure 3.6 - (a) Compressive strength for all unary GP at 28 days; (b) Compressive strength of GP4 subjected to different curing mediums and

	15
time.	75
Figure 4.1 – X-ray diffraction (XRD) pattern for (a) metakaolin and (b) silica fume, showing a high degree of amorphicity.	85
Figure 4.2 – (a) Metallic molds coated with non-stick adhesive tape and (b) Mold filled with fresh geopolymer.	87
Figure 4.3 - Set used for autoclave curing: stacked metal molds (on the right) and metal compartment for inserting the molds (on the left).	88
Figure 4.4 – (a) Compressive strength gain as a function of curing time at various curing temperatures (21°C, 50°C, 90°C, 150°C, and 200°C) at 1 atm and (b) zoomed portion to demonstrate the difference in initial setting from 50°C to 200°C.	90
Figure 4.5 – Formation of microcracks in the geopolymer after testing in the UCA at (a) 150°C and (b) 200°C.	91
Figure 4.6 – Compressive strength gain at room temperature (21°C) as a function of curing time at various curing pressures (0.1 MPa, 20 MPa, 40 MPa, 70 MPa).	92
Figure 4.7 – Compressive strength at different curing temperatures (21°C, 50°C, 90°C, 150°C, 200°C) at ambient pressure (0.1 MPa) for (a) 1-day curing and (b) 3-day curing.	93
Figure 4.8 – Compressive strength at different curing pressures (0.1 MPa, 20 MPa, 40 MPa, 70 MPa) at 21°C for (a) 1-day curing and (b) 3-day curing.	94
Figure 4.9 – Compressive strength for different combinations of temperature and curing pressures at (a) 1-day curing and (b) 3-day curing.	95
Figure 4.10 - Stress-strain curves illustrating the behavior of select specimens subjected to uniaxial compression testing.	97
Figure 4.11 – Compressive strength gain at different curing temperatures and pressures, corrected by an adjustment made by Kamali et al. [20].	98
Figure 4.12 – Thermogravimetric curves of specimens cured for 1 day at (a) different temperatures and (b) under different pressures.	98
Figure 4.13 – DTG curves of specimens cured for 1 day at (a) different temperatures and (b) under different pressures.	99

- Figure 4.14 – (a) TGA and (b) DTG curves for geopolymer cured for 1 day at 50°C under different pressures. 100
- Figure 4.15 – (a) Cumulative pore volume and (b) pore size distribution for geopolymer cured for 1 day at different temperatures (21°C, 50°C, 90°C, 150°C, 200°C) at 1 atm. 101
- Figure 4.16 – (a) Cumulative pore volume and (b) pore size distribution for geopolymer cured for 1 day at different pressures (0.1 MPa, 20 MPa, 40 MPa, 70 MPa). 101
- Figure 4.17 – (a) Cumulative pore volume and (b) pore size distribution for geopolymer cured for 1 day at 50°C different pressures (0.1 MPa, 20 MPa, 40 MPa); (c) Cumulative pore volume and (d) pore size distribution for geopolymer cured for 1 day at 150°C different pressures (0.1 MPa, 20 MPa). 103
- Figure 4.18 – Microstructure of samples cured at 21°C in (a) 1-day curing and (b) 28-days curing. 104
- Figure 4.19 – Microstructure of samples cured for 1 day at (a) 50°C, (b) 90°C, (c) 150°C, (d) 200°C. 105
- Figure 4.20 – Microstructure of the geopolymer cured at 200°C showing the presence of (a) debris (marked by red rectangles); (b) a debris in detail; (c) EDS map and (d) EDS spectrum. 106
- Figure 4.21 – Microstructure of the geopolymer 1-day cured at 21°C under the pressure of (a) 0.1 MPa (atmospheric pressure); (b) 20 MPa; (c) 40 MPa; (d) 70 MPa. 107
- Figure 4.22 – Microstructure of the geopolymer 1-day cured at 50°C under the pressure of (a) 20 MPa; (b) 40 MPa. 108
- Figure 4.23 – Microstructure of the geopolymer 1-day cured at 150°C under the pressure of (a) 20 MPa; (b) 40 MPa. 108
- Figure 5.1 – Particle size distribution for (a) Metakaolin and (b) Chamotte70 (before and after grinding). 120
- Figure 5.2 – Visual comparison: (a) Chamotte70 in its original state as supplied, and (b) after the grinding process. 120
- Figure 5.3 – XRD pattern for Chamotte70 as supplied and after grinding

	17
(Chamotte70-G).	121
Figure 5.4 – Visual contrast: (a) nanoclay in its original state as supplied, and (b) nanoclay after heating at 750°C for 2 hours.	123
Figure 5.5 – XRD pattern for nanoclay in its original state as supplied and nanoclay after heating at 750°C for 2 hours.	123
Figure 5.6 – Microscopic images provided by the manufacturer (NanoView), showing: (a) a singular functionalized MWCNT; (b) the multiple walls of MWCNTs within a single particle; (c) an ensemble of MWCNTs; and (d) the varied multiple walls of different MWCNTs.	125
Figure 5.7 – X-ray diffraction (XRD) pattern of MWCNT.	126
Figure 5.8 – Optical microscopy analysis of MWCNT clusters in alkali solution for (a) non-functionalized MWCNTs and (b) functionalized MWCNTs. MWCNTs dispersed in alkali solution considering: (c) non-functionalized MWCNTs and (d) functionalized MWCNTs.	132
Figure 5.9 – MLS results for: functionalized MWCNTs dispersed in alkali solution: (a) transmitted light and (b) backscattered light; non-functionalized MWCNTs dispersed in alkali solution: (c) transmitted light and (d) backscattered light.	133
Figure 5.10 – Vicat test at room temperature (21°C) for plain geopolymer (GP-0) and geopolymer with: chamotte (GP-Cha), nano-metakaolin (GP-NMK), carbon nanotubes (GP-CNT) and all these additions together (GP-H).	134
Figure 5.11 – (a) Heat flow of different geopolymer compositions as a function of curing time; (b) Polycondensation peak; (c) Heat flux between 1 and 7 days of curing; (d) Cumulative heat for all geopolymers design	136
Figure 5.12 – Compressive strength values for different geopolymer formulations molded into 10 mm cubes cured under 21°C and 150°C, at atmospheric pressure.	137
Figure 5.13 – XRD patterns for (a) GP-CNT cured at 21°C and 150°C, for 1 day; (b) GP-0 cured at 21°C for 1 and 28 days; (c) GP-0 and GP-H cured at 21°C for 28 days.	138
Figure 5.14 – (a) Cumulative pore volume and (b) pore size distribution for geopolymer cured for 1 day at 21°C, considering different geopolymer	

- formulations; (c) Cumulative pore volume and (d) pore size distribution for geopolymer cured for 1 day at 150°C, considering different geopolymer formulations. 139
- Figure 5.15 – Load x CMOD curves obtained by 3-point bending tests for plain geopolymer (GP-0) and geopolymer with hybrid additions (GP-H) cured at 21°C and 150°C. 141
- Figure 5.16 – Samples after subjected to 3-point bending tests: (a) GP-0 and (b) GP-H, cured at 21°C for 7 days; (c) GP-0 (cracked completely during curing) and (d) GP-H, cured at 150°C for 1 day; (e) GP-0 and (f) GP-H, cured at 21°C for 28 days. 142
- Figure 5.17 – (a) Cumulative pore volume and (b) pore size distribution for GP-0 and GP-H cured at 21°C and 150°C. 142
- Figure 5.18 – (a) TGA and (b) DTG curves for geopolymer cured for GP-0 and GP-H cured at 21°C and 150°C for 1 day. 143
- Figure 5.19 – Compressive strength for 21°C and 40 MPa for plain geopolymer (GP-0) and geopolymer with hybrid additions (GP-H). 144
- Figure 5.20 – (a) Cumulative pore volume and (b) pore size distribution for GP-0 and GP-H cured at 21°C and 40 MPa. 144
- Figure 5.21 – (a) TGA and (b) DTG curves for geopolymer cured for GP-0 and GP-H cured at 21°C and 40 MPa. 145
- Figure 5.22 – Compressive strength for GP-0 and GP-H molded into 50.8 mm cubes cured at 150°C and 40 MPa. 146
- Figure 5.23 – (a) Cumulative pore volume and (b) pore size distribution for GP-0 and GP-H cured at 150°C and 40 MPa. 147
- Figure 5.24 – (a) TGA and (b) DTG curves for GP-0 and GP-H cured at 150°C and 40 MPa. 147
- Figure 5.25 – Microstructure of geopolymer with hybrid additions (GP-H) samples cured at (a) 21°C; (b) 40 MPa; (c) 150°C; (d) 21°C (28 days). 148

List of tables

Table 2.1 - Formulations and curing conditions for the results indicated in Figure 2.2, for geopolymers.	45
Table 2.2 - Formulations and curing conditions for the results indicated in Figure 2, for Portland cement and alkali-activated systems.	45
Table 3.1 - Composition for formulating 1000 g of waterglass and quantity of resulting products: detailed breakdown by weight of components.	63
Table 3.2 - Composition (% wt.) of metakaolin MetaMax from BASF determined by XRF.	63
Table 3.3 - Geopolymer design: detailed breakdown by weight of components.	64
Table 3.4 - Geopolymers tested in uniaxial compression tests as a function of time and curing medium.	67
Table 3.5 - Avrami's parameters for all geopolymers design.	70
Table 3.6 - pH values for different unary geopolymers considering the two curing conditions (dry and saturated).	71
Table 3.7 - pH values of the curing water at 1 and 3 days, after GP4 curing stages.	72
Table 4.1 – Composition of metakaolin determined by X-ray fluorescence (XRF), expressed in weight percentages (%wt.).	85
Table 4.2 – Physical properties of metakaolin and silica: BET, density, and average particle size.	85
Table 4.3 – Composition of geopolymer formulation: detailed breakdown by weight of components.	86
Table 4.4 – Porosity (%) measurements for geopolymers submitted to different curing regimes (temperature and pressure) after 1 day of curing.	103

Table 5.1 – Composition of raw materials determined by X-ray fluorescence (XRF), expressed in weight percentages (%wt.).	121
Table 5.2 – Mass distribution and lattice parameters of crystalline phases obtained by XRD analysis for Chamotte70 and Chamotte70-G.	122
Table 5.3 – Mass distribution of crystalline phases obtained by XRD analysis for nanoclay and nanoclay-C.	124
Table 5.4 – Physical properties of the nanoclay provided by the manufacturer.	124
Table 5.5 – Physical and chemical properties of the MWCNTs provided by the manufacturer.	126
Table 5.6 – Chemical composition of MWCNT expressed in weight percentages (%wt.) provided by the manufacturer.	126
Table 5.7 – Geopolymer design guided by the alkali solution/metakaolin mass ratio and the mass fraction of components, expressed in weight percentages (%wt.).	127
Table 5.8 – Fresh properties of the geopolymer (consistency and flowability).	134
Table 5.9 – Setting times determined from the curves obtained by the Vicat test for plain geopolymer (GP-0) and geopolymer with: chamotte (GP-Cha), nano-metakaolin (GP-NMK), carbon nanotubes (GP-CNT) and all these additions together (GP-H).	135
Table 5.10 – Mass distribution and lattice parameters of crystalline phases obtained by XRD analysis for GP-H cured at 21°C for 28 days.	138
Table 5.11 – Porosity and mean pore diameter (d_{50}) for different geopolymer formulations cured at 21°C and 150°C for 1 day.	140
Table 5.12 – Fracture toughness (K_{IC}) and flexural strength (σ_f) values obtained by 3-point bending tests for plain geopolymer (GP-0) and geopolymer with hybrid additions (GP-H).	141
Table 5.13 – Porosity and mean pore diameter (d_{50}) for GP-0 and GP-H cured at 21°C and 40 MPa.	144

“Deus é fiel com o justo, e justo com o infiel.”
Juarez Alves

1. Introduction

Geopolymers are polysilicate-aluminates, inorganic polymers or chemically bonded ceramics [1] and can be used as binding materials in civil construction applications, oil well cementing and as refractory linings. Compared to Portland cement-based materials, it presents lower drying shrinkage and excellent resistance to salt attack [2]. The curing temperature has a significant influence on the final properties of the geopolymer as it acts directly on the geopolymerization process [3]. Moreover, pressure curing has demonstrated the ability to enhance the engineering properties of geopolymer composites [4].

Geopolymer (GP) achieves a substantial portion of its strength within the first three days of curing, with around 80% of the final compressive strength attained during this period [5]. There is no significant difference in strength between 7 and 28 days [6, 7]. Therefore, the rapid kinetics of geopolymers at early ages can pose a challenge when aiming at improved mechanical performance and durability [8], especially when curing at high temperatures. As the chemical reactions become accelerated, they lead to rapid shrinkage, which can cause high stress gradients, rendering the material more prone to severe cracking, due to the increase in the rate of water evaporation.

Thus, plain geopolymers tend to crack during drying if liquid removal is carried out at high rates, producing a heterogeneous microstructure with larger pore sizes [9]. Two alternatives are proposed to mitigate the effects of drying shrinkage of geopolymers at high temperatures: the use of an alkaline solution based on potassium, as Nadir *et al.* [10] showed that it leads to more stable GPs compared to Na, or the addition of reinforcing phases.

In this sense, the incorporation of nanoparticles (NPs) stands out, as they enable the production of a binder with greater strength and durability and there is no need to change the paste formulation, such as increasing the amount of reactive material or reducing the amount of solution, which would directly impact the rheological properties. Furthermore, NPs make it possible to add functionalities to the GP, such as self-sensing, self-cleaning, self-healing capabilities [11-13]. NPs

can act as embedded sensors, with carbon nanotubes (CNT) standing out due to their excellent durability in a highly corrosive environment [14].

NPs can influence mechanical properties through different effects: as reinforcements, reactive particles and sites for product nucleation [11, 13]. For reinforcement, multi-walled carbon nanotubes are often used [15], and it was shown by Rabiaa *et al.* [16] that the tensile and flexural performance of GPs with NPs as reinforcements was comparable to the use of steel fibers. The high surface area to volume ratio favors greater chemical reactivity [12, 13]. The elevated surface energy of the material also promotes its role as favorable sites for product nucleation, contributing to the densification of the microstructure and the formation of an interfacial transition zone (ITZ) [6, 13]. These factors collectively enhance the durability of the geopolymer.

However, some challenges must be overcome before proposing the use of NPs in the field, including dispersion, scale-up and reduction of the cost-benefit ratio [13]. The introduction of an optimal amount of NPs can result in substantial enhancements in material properties. However, an excess of NPs can lead to agglomeration, negatively impacting the material [6, 11, 13], since clusters can act as stress concentrators, for example. Studies have demonstrated that achieving optimal dosage, coupled with the combination of various micro- and nanomaterials, ensures the superior properties [11].

Adequate dispersion can be obtained by methods such as high-speed melting mixing, surface treatment of NPs, and sonication of NPs in aqueous solution with a surfactant. However, high-speed melting mixing is difficult to apply in the field and can deteriorate the properties of NPs. Additionally, some surfactants have adverse effects on the piezoresistivity of carbon nanofibers (CNF) composites [12].

GPs are promising for oil well cementing applications due to their fast-setting times and rapid early strength gain [17]. This makes them a viable alternative to Portland cement, which has limitations in harsh downhole environments with varying pressure, temperature, and chemical conditions across different geographic locations [18].

An understanding of physical and chemical processes at the micro- and nanoscale is fundamental for controlling macroscale properties and performance, as well as formulating long-term predictions [13], as the stability of GP is a critical factor before proposing its widespread application.

1.1. Goals

The main goal of this thesis is to understand the curing effects at elevated temperatures (up to 200°C) and pressures (up to 70 MPa) on the properties of metakaolin-based geopolymers. For this, the following specific goals have been defined:

- Evaluate the reaction mechanisms of metakaolin-based geopolymers during the initial curing stages by comparing four different potassium waterglass formulations;
- Determine the effects of alkali leaching on the strength evolution of geopolymers under different curing media (dry and saturated conditions);
- Examine the influence of elevated temperatures and pressures (200°C and 70 MPa) on the chemical reactions within metakaolin-based geopolymers;
- Analyze the mechanical behavior through uniaxial compression and 3-point bending tests of geopolymers cured at high temperatures and/or pressures;
- Evaluate the effect of adding micrometric (chamotte) and nanometric (nanoclay, carbon nanotubes) reinforcements in the chemical reactions, porosity and mechanical properties of the geopolymer

1.2. Thesis organization

This thesis is structured into several chapters, each serving a distinct purpose, where:

- (i) Chapter 1 provides a brief introduction to the topic, outlining its scope, objectives, and relevance;
- (ii) Chapter 2 encompasses a comprehensive literature review, delving into the definition of geopolymers, their differentiation from alkali-activated systems, formulation techniques, curing conditions, addition of reinforcements, key findings in the existing literature, and potential applications;

Chapters 3 to 5 are presented in article format, respectively:

- (iii) Chapter 3 focuses on evaluating the reaction mechanisms of geopolymers and the effects of alkali leaching on the strength evolution under different curing media (dry and saturated conditions);

(iv) Chapter 4 explores the influence of high temperatures and pressures (200 °C and 70 MPa) on chemical reactions in geopolymers and their resulting mechanical behavior;

(v) Chapter 5 examines the effect of adding micrometric (chamotte) and nanometric (nanoclay, carbon nanotubes) particles on the properties of the geopolymer after curing in extreme conditions (150°C and 40 MPa);

(vi) Chapter 6 concludes the thesis by summarizing the main findings and offering suggestions for future research endeavors.

1.3. References

1. Ling, Y., Wang, K., Wang, X., Hua, S. (2019). Effects of mix design parameters on heat of geopolymerization, set time, and compressive strength of high calcium fly ash geopolymer. *Construction and Building Materials*, 228
2. Slaty, F., Khoury, H., Rahier, H., Wastiels, J. (2015). Durability of alkali activated cement produced from kaolinitic clay. *Applied Clay Science*, 104. pp. 229–237.
3. Salehi, S., Khattak, M.J., Rizvi, H., Karbalaei, S.F., Kiran, R. (2017). Sensitivity analysis of fly ash geopolymer cement slurries: Implications for oil and gas wells cementing applications. *Journal of Natural Gas Science and Engineering* 37, 116-125.
4. Zivica, V., Balkovic, S., Drabik, M. (2011). Properties of metakaolin geopolymer hardened paste prepared by high-pressure compaction. *Construction and Building Materials* 25. pp. 2206–2213.
5. Rouyer, J., Benavent, V., Frizon, F., Poulesquen, A. (2017). Influence of geopolymer formulation parameters on the elastic and porous properties over a one-year monitoring. *Materials Letters*, 207. pp. 121–124.
6. Alvi, M.A.A., Khalifeh, M., Agonafir, M.B. (2020). Effect of nanoparticles on properties of geopolymers designed for well cementing applications. *Journal of Petroleum Science and Engineering* 191. pp. 107-128.
7. Ferone, C., Colangelo, F., Roviello, G., Asprone, D., Menna, C., Balsamo, A., Prota, A., Cioffi, R., Manfredi, G. (2013). Application-Oriented Chemical Optimization of a Metakaolin Based Geopolymer. *Materials*, 6, 1920-1939.
8. Liang, G., Yao, W., She, A. (2023). New insights into the early-age reaction kinetics of metakaolin geopolymer by ¹H low-field NMR and isothermal calorimetry. *Cement and Concrete Composites*, 137.
9. Djangang, C.N., Tchamba, A.B., Kamseu, E., Melo, U.C., Elimbi, A., Ferrari, A.M., Leonelli, C. (2014). Reaction sintering and microstructural

- evolution in metakaolin metastable alumina composites. *J Therm Anal Calorim* 117:1035–1045.
10. John, S.K., Nadir, Y., Cascardi, A., Arif, M.M., Giriya, K. (2023). Effect of addition of nanoclay and SBR latex on fly ash-slag geopolymer mortar. *Journal of Building Engineering* 66.
 11. Abdalla, J.A., Thomas, B.S., Hawileh, R.A., Yang, J., Jindal, B.B., Ariyachandra, E. (2022). Influence of nano-TiO₂, nano-Fe₂O₃, nanoclay and nano-CaCO₃ on the properties of cement/geopolymer concrete. *Cleaner Materials* 4.
 12. Lu, S-N., Xie, N., Feng, L-C., Zhong, J. (2015). Applications of Nanostructured Carbon Materials in Constructions: The State of the Art. *Journal of Nanomaterials*.
 13. Sanchez, F., Sobolev, K. (2010). Nanotechnology in concrete – A review. *Construction and Building Materials* 24. 2060–2071.
 14. McCoy, M., Betts, J., Norris, A., Saafi, M. Nanotechnology In Construction: Nano Materials And Devices Offer Macro Improvements In Concrete Materials.
 15. Khater, H.M., Abd el Gawaad, H.A. (2016). Characterization of alkali activated geopolymer mortar doped with MWCNT. *Construction and Building Materials* 102. 329–337.
 16. Rabiaa, E., Mohamed, R. A. S., Sofi, W. H., Tawfik, T.A. (2020). Developing Geopolymer Concrete Properties by Using Nanomaterials and Steel Fibers. *Advances in Materials Science and Engineering*.
 17. Adjei, S., Elkatatny, S., Sarmah, P., Abdelfattah, A. M. (2021). Evaluation of calcined Saudi calcium bentonite as cement replacement in low-density oil-well cement system. *Journal of Petroleum Science and Engineering*, 205.
 18. Kamali, M., Khalifeh, M., Saasen, A., Godøy, R., Delabroy, L. (2021). Alternative setting materials for primary cementing and zonal isolation – Laboratory evaluation of rheological and mechanical Properties. *Journal of Petroleum Science and Engineering*, 201.

2. Literature Review

2.1. Geopolymers

Geopolymers (GPs) are inorganic polymers generally produced at temperatures below 100°C, formed by chains linked by covalent bonds as a result of dissolution of an aluminosilicate source in alkali solution. The final structure can be amorphous or semi-crystalline [1, 2].

GPs differ from gels due to their defined macromolecular structure (size and molecular weight) [3]. Composed of alumina, silica, and alkali metal oxides, GPs form a nanoparticulate array [4].

Geopolymerization requires a considerably rapid silica-alumina reaction under alkali conditions, resulting in a three-dimensional polymeric chain of Si-O-Al-O bonds, in the form of the basic structure of geopolymers: silicon-oxygen tetrahedron connected by an atom of oxygen to an aluminum-oxygen tetrahedron [5].

The higher dissolution rate of aluminosilicate leads to a higher Si:Al ratio in the product. Si-O-Si bonds have greater strength compared to Al-O-Al and Si-O-Al bonds and, thus, a Si:Al ratio leads to a stronger GP [6], however the formation of Si-O-Al bonds is thermodynamically more favorable than the formation of Si-O-Si bonds [7].

In the synthesis of GPs, the hydroxyl groups, $Si(OH)_4$ and $Al(OH)_4^-$, dissolved from the aluminosilicate source are connected to produce new Si-O-Si and Si-O-Al bonds. This type of reaction can continue to build larger molecules, forming a continuous polymer network. In the reorganization process, there is the formation of an Al-rich phase and a Si-rich phase [8].

Thus, the geopolymerization mechanism is based on dissolution-precipitation and polycondensation, where alkali ions act as network ligands and charge balancers. The alkaline solution governs the dissolution and polycondensation process and consequently influences the strength gain. During

geopolymerization the following sequence occurs: dehydration, dehydroxylation, densification and final plastic deformation due to water evaporation [9].

During setting, the aluminosilicate precipitates coexist with silicate species in solution and unreacted aluminosilicate particles, and the three-dimensional network structure is not completely formed. As geopolymerization progresses, the entangled agglomerated units progressively connect, increasing stiffness [7].

A characteristic of geopolymers is the repeatability and reversibility of thixotropy, as physical restructuring of the paste occurs after subjecting it to extremely high shear, due to the physical rearrangement and attraction of Si and Al tetrahedra. Thus, the initial changes in viscosity are not entirely the result of the chemical reaction of geopolymerization [10].

2.2. Geopolymer vs Other Materials

In the geopolymerization process, water acts as a transport medium for dissolved substances and does not participate in the reaction, as in the case of Portland cement [11]. Thus, the geopolymerization do not follow the mechanisms of pozzolanic and hydration reactions [12].

There is a similarity between the chemical composition of cement and slag, as both have a high content of CaO, necessary for the formation of calcium silicate hydrated (C-S-H) gel and calcium aluminosilicate hydrated (C-A-S-H) gel [13]. Slags are more reactive under moderately alkaline pH relative to low calcium aluminosilicate sources and activation can be obtained from several activators [14], such as those based on metal alkali carbonates and sulfate [15]. Activation of slag produces a low-calcium amorphous alkaline aluminosilicate hydrate, N-A-S-H or K-A-S-H gel, as well as C-A-S-H gel [4, 16, 17].

Compared to PC concrete (PCC), alkali activated slag concrete (AASC) has better properties and durability, such as compressive strength [18-20], splitting tensile strength [19, 21], drying shrinkage (except for curing under high relative humidity) [22], high temperature resistance and the smallest pores reduce the penetration of aggressive ions [19, 21, 23]. The elastic modulus of AASC is around 10% lower than PCC at 28 days [18, 23] and this type of concrete is more susceptible to carbonation [23].

GPs can be considered much better substitutes for PCs due to several

benefits such as chemical stability [24-26], rapid strength gain [24], more refined pores [13], low shrinkage and high freeze-thaw resistance [24] and for applications up to 1100°C [9, 27]. However, GPs tend to be more brittle than PCs [24].

In GP concrete (GPC), the flexural strength can reach 12 MPa, representing 20 to 25% of the compressive strength, while for PC concrete (PCC) the values reach 10 MPa and 10 to 15%, respectively [28]. This may be due to the fact that GPC exhibits similar or better adhesion properties than PCC [29, 30], including at high temperatures [30]. For this reason, Sarker *et al.* [31] observed that GPC failed in a more brittle way than PCC, probably as a result of the higher bond strength for GP and the higher crack propagation threshold observed by Kanesan *et al.* [26].

However, Ding *et al.* [32] found that GPC presented greater ductility than PCC with similar compressive strength, caused by a greater number of cracks generated in the GPC.

In GPs, autogenous shrinkage is the result of self-desiccation and chemical shrinkage, the former as a result of continuous water removal through the capillary pores and the latter as a result of polymerization and reorganization in the fresh state. In geopolymers, volume variation is mainly due to drying shrinkage [33] and when compared to PC, GP showed a lower or similar drying shrinkage after 180 days [8].

GP mortar can equal or even surpass cement mortar in terms of compressive strength [34], as Kamali *et al.* [35] showed that the compressive strength of class G cement had a slight decrease during the period from 7 to 28 days, under temperature and pressure, unlike GP where strength is constant over time.

The cement hydration process occurs much faster than the setting because in GPs aluminosilicate source absorb less water, which increases the fluidity and thus slows down the chemical reaction [36]. There is no retention of water by the reaction products in GP unlike cement hydrates and, thus, the aging effect of GP is not associated with the release of structural water, but with the density of tetrahedra per unit volume which will be significantly reduced if part of the products crystallizes [37].

2.3. Aluminosilicate Sources

As discussed, slags cannot be used for the production of GP, as they

generally meet the criteria of activated alkali systems, which corresponds to any material containing reactive Ca, Si and Al [38-40]. One way to check whether a given source of aluminosilicate is suitable to produce GP is to check its CaO content, which when greater than 10% will be classified as pozzolan, according to ASTM C618 [41] and, therefore, not suitable for the production of GP.

There are several sources of aluminosilicate with potential for use in GP formulations, including: fly ash, calcined clays, kaolin, illite/smectite and metakaolins [42]. The chemical and mineralogical compositions of these sources, in addition to the fineness, are key factors for their reactivity [2]. The different sources of aluminosilicates do not affect the crystallization temperature or lead to the formation of distinct phases [43]. Among the most used are metakaolin (MK) and fly ash (FA).

The MK derives from the removal of hydroxyl groups from layered kaolinite, a well-crystallized structure [44], from thermal activation of clay minerals between 500 to 800°C [42, 45], with temperature being a function of the purity and degree of crystallinity of the clay [45]. It then becomes a material with an amorphous structure [44, 45], consisting of assembled layers of aluminate and silicate, with silicon in coordination 4 and aluminum in a mixture of coordination 4, 5 and 6 [44]. MK is highly reactive [4] as a result of the distortion in the bond network induced by thermal dehydroxylation in which the aluminum coordination number is changed [44]. However, when produced from sources of good quality white kaolinite clay achieves the highest reactivity [12], although it was shown by Kuenzel *et al.* [46] that an MK with a higher level of impurities allowed the GP to set in about 15 h, different from an MK of high purity, where setting occurred in 42 h, probably because the impurities acted as sites for the nucleation and growth of the reaction products.

The high fineness of MK requires a large amount of liquid phase to be dissolved [28] and also to adapt the rheology for use in some applications, which can generate shrinkage due to excessive drying [47]. However, MK is generally preferable as it easily participates in the geopolymerization reaction as it is a purer system [45, 48]. Furthermore, the dissolution rate of MK is faster than that of FA at the same temperature, because MK particles are plate-shaped and thus there is a larger contact area with the alkaline solution compared to spherical FA particles. The disrupted molecular structure of the MK particle versus the slightly deformed

structure of FA ensures greater reactivity [33].

The low reactivity of FA normally requires curing at temperatures above 40°C, creating difficulties for in-situ application [8, 49-51]. Also, the mechanical properties are inferior to MK-GP due to the generation of fewer reaction products and the larger volume of large pores, while the porosity of MK-GP involves pores smaller than 100 nm [52]. The large pores also explain the fact that FA-GP presents superior permeability to cement paste, at the same curing age, being more pronounced at advanced ages [51].

2.4. Geopolymer Design

The main variables that influence the mechanical properties of GP are: type [11, 26, 53] and concentration [11, 16, 26, 53] of the alkali solution, ratio of alkali solution to reactive aluminosilicate [26, 53] and curing age. Some authors [53, 54] have demonstrated that the alkali/binder ratio is the most significant parameter. However, it must be considered that compactness strongly affects strength [55].

The M:Al ratio (where M is an alkali metal) considered ideal is one, [56]. Furthermore, the presence of metallic alkali oxides is harmful for the production of strong $Al_2O_3 \cdot SiO_2$ systems, being critical to choose the correct amount of alkali in relation to the Si:Al ratio for good thermal resistance [9].

High alkalinities are generally preferable, however there is a maximum value that must be used, depending on the type of alkali solution and the aluminosilicate source, as excessive alkalinity impair the mechanical properties [16], due to: reduce the geopolymerization [11, 57], faster gel formation on aluminosilicate particles, suppressing further dissolution [58]; increase sensitivity to drying shrinkage [32, 56]; reduce flowability and workability [28] and; increase gel pore volume [59]. In turn, the optimal level of alkalinity is crucial for: thermal stability [52]; solubility [28, 32, 54, 58-61]; hardening, since the alkali ions act as balancers of the negative charge of the aluminate groups [4, 28]; reduce the setting time [12, 19]; reduce the porosity and refine the pores [22, 51].

Increasing the ratio of water to binder acts to: delay geopolymerization [32, 53, 57]; reduce viscosity [62]; delay setting [46]; increase porosity [32, 47, 53, 58, 63, 64]; reduce the geopolymerization by weakening alkalinity [49, 63]. Strength increases with decreasing water/binder ratio, but is not a dominant criterion for

potassium-based alkaline solutions [11]; for sodium-based solutions Pacheco-Torgal *et al.* [28] showed that a H_2O/Na_2O molar ratio below 9.5 is beneficial for increasing strength, with the optimum value being 8.9.

The variation of cations leads to important modifications in terms of formation and structure of the final products [65, 66]. The AlO_4^- pairs affect the sensitivity to drying shrinkage, being that K^+ can better stabilize the charge of AlO_4^- [56]. Therefore, silicate monomers and smaller dimers favor ion pairing with Na^+ , while K^+ favors ion pairing with larger silicate oligomers [62]. For this reason, Na-based begin to polycondense and harden faster than K-based [60, 62], due to difference between their ionic diameters [11].

Kamali *et al.* [35] demonstrated that a K-GP formulation does not set until about 40 h under $90^\circ C$; however, a stoichiometric K-based MK-GP formulation ($K_2O \cdot Al_2O_3 \cdot 4SiO_2 \cdot 11H_2O$) used by Brandvold *et al.* [10], presented an initial setting close to 15 h and a final setting time of 25 h, at $21^\circ C$.

Regardless, above Si:Al=1.5, the compressive strengths for Na- and K-based GPs are comparable, but in general, K-based has a less porous and more homogeneous structure, because it is a less viscous alkali solution, ensuring better mixing and removal of air bubbles [62]. However, the acid resistance of Na-based is better than K-based due to the more stable cross-linked aluminosilicate polymeric structure [65], as Na^+ have better zeolitization capabilities compared to K^+ , due to the greater charge density and ability to migrate due to smaller dimensions [53]. K-based systems, in turn, exhibit better thermal stability compared to Na-based systems [66].

The greater presence of silica in solution can favor an increase in the Si:Al ratio in the products [11], as silicate species already available favors the polycondensation [53, 57, 58, 67, 68], intensifying the reaction [11, 67] and increase the number of larger species [67, 69]. Dissolution and condensation can occur simultaneously [7]. Greater condensation between oligomeric silicates and aluminates favors the formation of the rigid 3D polymeric structure [11, 67, 70].

Furthermore, a greater amount of dissolved silicon leads to a lower total porosity and finer pore system [22, 51] in addition to delay and even, prevent crystallization [11, 37]. However, high contents of silicon can be harmful, as it may be present in structurally distinct polymeric forms (oligomers) and even under the monomer form, affecting the structure formation [11], as a consequence of

incomplete reactions [67], delay in the dissolution and prolongation of the geopolymerization process [57] and, prevention of water evaporation [11].

The Si:Al ratio governs the compressive strength [49, 53, 55, 62, 67, 70], with more product formation expected as this ratio increases [56]. In terms of mechanical properties, the ideal Si:Al molar ratio is considered to be around two [56], with Ferrone *et al.* [69] suggesting a value of 1.75 to have the best compromise between mechanical performance and low shrinkage. Si:Al values greater than 2 showed greater amounts of unreacted MK, as very viscous formulations prevent uniform mixing [45, 62], along with the greater volume of trapped air [56].

2.5. Curing Conditions

Curing conditions influence the microstructural development, among which temperature stands out as one of the most significant factor [11], where maximum strength is generally obtained under initial curing at 60°C [49].

For a given Si:Al ratio, there is generally not much difference in reaction product contents independent of the curing regime [49], as the degree of reaction in GP increases with aging [34, 40, 62, 67]. It is worth noting that the rate of strength gain with curing time is independent of the quantity of aggregates, when used [34].

The relative humidity is another factor that affects the geopolymerization velocity because it affects the removal of free water [71, 72]. Water-cured GPs showed lower flexural and compressive strength compared to dry curing [73, 74], attributed to water absorption that generates additional stress when penetrating cracks and defects [74]. The dissolution of alkali can be another cause for the reduction in the strength [75].

Analysis of alkali leaching in GPs demonstrated that the mechanism is mainly controlled by diffusion [76] and long cracks act as pathways for leaching. Thus, two diffusion coefficients were proposed: D_{app} , which is governed by GP chemistry (depends mainly on free alkalis) and, D_{eff} , which is a function of porosity and pore connectivity [77]. However, GP prepared with 8M alkali solution showed greater alkali leaching compared to GP formulated with 10M and after 4 months the latter no longer showed leaching, unlike 8M [78], which probably had a greater number of open pores and a lower degree of geopolymerization. Temperature is another factor that must be considered, as submerged samples

showed significantly lower alkali leaching at higher temperatures [73], which may be a result of the increased velocity of geopolymerization.

FA-GP systems result in higher alkali releases compared to MK-GP systems, due to the former's lower reaction rate [76], demonstrated by D_{app} for FA-GP mortar about 45 times compared to MK-GP mortar, as a result of more free alkalis in the pore solution. It is worth noting that for the same aluminosilicate source, mortars generally have less leaching than pastes because the inclusion of aggregates makes the paths for leaching more tortuous [77].

Water curing is not recommended for FA-GP as the compressive strength values at 28 days were around 53.3% lower than dry curing; in saline solutions it showed better results, with greater strength for higher concentrations, but they remained inferior by around 27.8% to the dry condition [79]. The saline environment favors the continuity of the reaction in the GP due to the dissolution of salts [25], which can potentially replace the leached alkali ions [56]. As for MK-GP, leaching does not affect compressive strength, even being shown by [73] that there was a gain even when curing in water compared to dry curing.

2.5.1. Temperature Effect

Curing GP at high temperature can cause cracks and even changes in the structure [50], due to the increase in the velocity and intensity of polycondensation [12, 26, 29, 43, 49, 52, 57, 70, 80, 81]. Proof of this is that Alvi *et al.* [82] showed that the maximum strength of GP was reached on the first day at temperatures between 50 and 70°C and Ridha *et al.* [83] found that around 70% of the strength is obtained within 3 to 4 h at high temperatures.

The increase in the intensity of geopolymerization was shown by Singh and Subramaniam [49], where for curing at 60°C the Si:Al ratio in the reaction product increased from 2.5 to 3.3 and the compressive strength was from 60 to 74 MPa, compared to 25°C. The improvement in strength can also be associated with a more refined pore structure by extending the curing time under temperature [51, 84], having been demonstrated by Zhao *et al.* [84] that between 50°C and 75°C, mesopores and macropores tend to gradually lead to nano-sized pore structure, however at 75°C the microstructure was more porous.

However, Muñoz-Villareal *et al.* [85] showed that GP cured between 30 and

90°C showed greater porosity compared to 20°C. But at 60°C the steps or events of the geopolymerization process occurred in a favorable way, leading to the highest compressive strength value. The same conclusion was obtained by Kajarathan *et al.* [86], Samantasinghar and Singh [87] and Salehi *et al.* [88]: the optimal curing temperature for plain GP is 60 °C.

GP cured at 90°C showed several heterogeneous areas and the presence of crystalline structures [87]. Zhao *et al.* [84] also observed a less ordered and more porous structure when GP was cured quickly at elevated temperature.

Above 100°C, water loss through micropores causes drying shrinkage due to capillary effects [89]. This effect causes deterioration in mechanical properties, as shown by Khalifeh *et al.* [90], at 125°C in 1 day, the compressive strength reached a maximum value and after this period a reduction occurred. This process is even more severe in unsealed conditions, as evaporation will occur more quickly [87].

The damage caused to the GP depends on curing temperature as this can cause shrinkage, attributed to capillary deformation phenomena, dehydroxylation reactions and viscous sintering, depending on the temperature range [45].

The shrinkage between 100 and 300°C is attributed to the loss of water [43] which was under three states: physically bound, chemically bound and hydroxyl group [91]. This phenomenon is called dehydration and will cause the formation of cracks as well as a substantial reduction in the modulus of elasticity [43]. The water lost before drying shrinkage occurs is referred to as free water and removed through the open macropore network [56].

Between 300 and 600°C the shrinkage is attributed to de-hydroxylation, which corresponds to the condensation of the chemically linked silicon-hydroxyl group to form shorter T-O-T bonds (where “T” is an aluminum or silicon atom) with water loss [43, 45, 55, 91].

From 600°C to 900°C the viscous sintering phenomenon predominates [27], accompanied by volumetric shrinkage due to the collapse of interparticle spaces in the reaction product [92].

Above 900°C the shrinkage tends to accelerate, a phenomenon called viscous sintering [43], the main characteristic is the increase in crystallinity [9] driven by free alkalis [52]. Typical crystalline phases for K-GP are leucite and kalsilite [3, 43] and, nepheline and albite for Na-GP. Upon cooling, at around 650

to 680°C, the transformation of cubic to tetragonal leucite occurs, resulting in volumetric contraction [3].

Thus, monolithic GPs can lose part of their strength to high temperatures mainly due to dehydration cracking [3]. Therefore, the addition of a reinforcing phase is essential to maintain structural integrity under elevated temperatures.

2.5.2. Pressure Effect

Pressure curing increases the FA reactivity by weakening the Si-O-Si bond of the crystalline component (quartz). High pressure conditions do not allow the crystallization of FA-GP activated by sodium silicate, as the silica dissolved in the alkali solution inhibits crystallization. Regardless of the composition of the alkaline solution, crystallization is unlikely for pressure-cured MK-GP systems [37].

The microstructure of pressure-cured GP shows a narrower pore size distribution and towards the refinement of dimensions [61], a trend resulting from the elimination of trapped air bubbles [71].

Paiva *et al.* [89] showed that curing under 10 MPa for 48 h had no effect on mechanical properties. Alvi *et al.* [82] found that the setting time was not affected by a pressure level equal to 14 MPa.

Few studies have been carried out on curing using pressure alone, as it is the combined effect of pressure and temperature that made it possible to improve compressive strength by up to 600% [71].

2.5.3. Coupled Effect of Temperature and Pressure

Curing under high temperature and pressure enables the crystallization of reaction products that will remain embedded in the original phase, forming a GP with a denser and more uniform structure [93]. Crystallization depends on the GP design, having been reported to occur under curing at 200°C and 24.4 MPa, 300°C and 48.7 MPa, 300°C and 73 MPa, 350°C and 98.6 MPa [72], increasing the compressibility of the matrix.

Curing GP under pressure and temperature also allows, in addition to the formation of zeolites, the redistribution of the basic structural units (SiO_4^{4-} and

AlO_4^{5-}) of GP and the activation of the crystalline component (quartz) of the aluminosilicate source. Crystallization up to a certain level improves mechanical properties by forming support networks, but after 4 days of aging the formation of other crystalline phases impairs the bonds between individual structures [66].

The autoclave treatment also allowed the SiO_2 content present in the red mud to become reactive and therefore suitable for dissolution in an alkali solution for the production of GP [74, 93].

Pressure thermal curing improves the transmission channel of the pore structure and refines its sizes [94]. For temperatures below 250°C, compressive strength is dependent on both temperature and pressure. The compact and uniform morphology obtained allows for better stress distribution and consequently the initiation of crack formation is postponed [72].

2.6. Particulate Reinforcement Use

The use of particles aims to improve strength, durability and volumetric stability. For purely reinforcing purposes, particles that are inert in the high alkalinity of the mixture should be chosen [3, 95]. The use of particulate reinforcements might change the microstructure, especially the ITZ [76], without introducing processing complexities [3]. Achieving an appropriate size distribution is essential to improve particle packing and mitigate drying shrinkage [96].

2.6.1. Microparticles

The addition of sand is an option to reduce drying shrinkage [33]. A support network formed by sand particles occurs in volumetric fractions greater than 25% [47]. Xiang *et al.* [96] showed that the addition of sand with Fuller-FS distribution to the GP reduced the pore volume from 0.18149 to 0.1032 cm^3/g . However, as shown by Trindade *et al.* [95], from at 500°C, all GPs reinforced with sand showed greater degradation compared to those that incorporated refractory particles. Furthermore, Kuenzel *et al.* [47] observed the formation of microcracks around sand particles, which may be due to low compatibility with GP binder.

Other reinforcements were suggested, such as: dolomite particles

($CaMg(CO_3)_2$), where the addition of 20 wt% made it possible to increase flexural strength from 7 to 16 MPa [97]; glass powder, which densified the microstructure and acted to reduce the rate of water loss at early ages [81] and; microsilica, which made it possible to increase stiffness and significantly improve compressive strength [89].

But for GPs it is suggested to use particles that have high percentages of SiO_2 and Al_2O_3 [13], with higher alumina contents performing better at high temperatures [9, 13], easily verified through the ternary phase diagram, where the region of high alumina concentration in the $K_2O \cdot Al_2O_3 \cdot SiO_2$ system develops more refractoriness. The interfaces between GP matrix and alumina grains at high temperature appear to be more stable [9]. In this context, it appears as a suitable alternative the chamotte.

Chamotte is kaolinite grade clay calcined from 1350°C [3, 44] to produce 38% crystalline mullite, as well as metastable cristobalite and quartz. It has a low aspect ratio and irregularly shaped grains. Its extremely low coefficient of thermal expansion reduces tensions between it and the GP at high temperatures. The inclusion of particulate chamotte reinforcement slightly reduced the crystallization temperature, as a result of the availability of sites for nucleation of reaction products [3, 52]. GP filled with chamotte leads to low shrinkage [43] (less than 1% up to 1200°C [52]), high heat resistance [43, 52], while providing pathways for faster and more complete dehydration [3]. However, this particulate has a good connection only with MK-GP and not with FA-GP, being ineffective in the latter case [52]. At 1000°C, GP reinforced with chamotte reaches 19.82 MPa of strength [95].

2.6.2. Nanoparticles

The particle size affects the development of ITZ, where smaller sizes lead to: greater homogeneity [63], lower porosities [98, 99] and pore refinement [99]. Among the nanoparticles (NPs) used as reinforcement are: single-walled carbon nanotubes (SWCNTs), multi-walled carbon nanotubes (MWCNTs) and carbon nanofibers (CNFs), which are materials based on highly structured graphene rings with very large aspect ratios (>1000) and high specific surface area [100], with excellent electrical and thermal properties [101]. Graphene, another carbon nanostructure, showed good dispersion and adhesion in GP in addition to acting as

a site for geopolymerization [102].

In turn, nanoclay allows the formation of a more dimensionally stable GP [91] and promises to improve mechanical performance and densification [100]. When adding nanoclay, the ideal curing temperature found by Sikandar *et al.* [16] was 90°C, very different from the value of 60°C found for plain GP.

NPs are also interesting for a reactive function, as dissolution occurs more easily for smaller particles [11, 13, 46]. This fact results from the greater surface area to volume ratio, making the particle more reactive [103, 104].

However, smaller particles are more susceptible to agglomeration due to the increased influence of van der Waals forces [104]. The better the dispersion, the more efficient the nano addition [105], as agglomeration can act as a barrier to the formation of the three-dimensional network and generate other problems, such as increased porosity [106].

In high-speed melt mixing process the dispersion of carbon nanomaterial is carried out under high shear mixing which can compromise its structure and is not easy to carry out in the field [107]. Dispersing in solution with the aid of sonication is widely used [39, 105, 108, 109, 110] but it requires a cooling system for long times and is also challenging in field conditions. A promising method is surface treatment of nanoparticles, such as nanostructured carbon functionalization, in which compatibility between binder and functional group plays a key role [82, 100, 107, 111].

The alkali solution used to process GPs has the potential to improve the interaction of MWCNTs with the GP, the first is due to the fact that alkali hydroxide acts as a surfactant and the second is to act on ionic conductivity [24]. It was found that the alkali solution played an important role in dispersion uniformity and long-term stability [24, 98, 102].

The carbon nanotube (CNT) most commonly used as reinforcement are MWCNT, consisting of many aligned cylinders [109]. They are nanoparticles with high thermal stability as disintegration only occurs above 850°C [112]. But one of the main challenges is the adequate dispersion of carbon nanotubes (as well as nanofibers) due to their high hydrophobicity [100]. The agglomeration of CNT in the GP can trigger several problems, such as hindering the propagation of the geopolymeric reaction [109, 113], acting as stress concentrators [105, 110].

For this reason, several researchers have evaluated different methodologies

to disperse CNTs: Brandão *et al.* [105] carried out dispersion directly on MK particles using absolute ethanol; Davoodabadi *et al.* [39] found that the best long-term stability for dispersion was obtained using a surfactant with sodium metasilicate solution, as this due to the higher viscosity reduces the mobility of MWCNTs, through the mechanism called electrostatic stabilization. However, the use of surfactants generates foaming during ultrasonication and even in high shear mixing [39, 110]. One of the alternatives is to use functionalized CNTs, which in addition to improving dispersibility, make CNTs more flexible [82].

Authors who used CNTs as an addition in GP found different addition levels that optimized their properties, such as: 0.1 [105, 109, 110], 0.5 [24] and 0.6 wt.% [113]. These values differed mainly depending on the dispersion methodology used and the characteristics of the CNTs (such as the existence and type of functionalization).

The effects of adding CNTs to GP are diverse: promote geopolymerization [82, 109, 113], by offering extra sites for product nucleation and when functionalized, the density of the carboxyl group can influence chain lengths [109]; densification [39, 82, 109, 113] and; significantly reduce drying shrinkage [109].

Furthermore, CNTs preserved the amorphous structure of MK-GP [113]. As a result of this, several properties were improved, such as: flexural strength [24, 105, 110], obtaining a value of 6 MPa [110] and an improvement of up to 160% [24]; compressive strength, obtaining values of 45 MPa [110] and an increase of 40% [105]; improvement in Young's modulus equal to 109% and; increased toughness [24, 113] reaching a value of 275% [24]. Moreover, the electrical conductivity can be strongly improved and present piezoresistive effect [24].

CNTs also have a retardant effect on setting time, which means greater workability for a longer period [114]. This characteristic improved fluid loss, suggesting the adhesion of the MWCNTs to the oligomers, a fact arising from the hydroxyl groups on the MWCNT surface reacting with the GP structure [82]. Chen and Akono [113] proved that MWCNTs promote the hydroxylation of Si atoms in GP since Si-OH bonds were formed, and a reduction in Si-O bonds, promoting the formation of a stronger phase with porosity equal to 0.45%.

The high aspect ratio and high modulus of MWCNTs facilitate load transfer, ensured by their high adhesion, described by the shear-lag model. The role of MWCNTs as crack-bridging was verified, and the occurrence of sliding between

the inner and outer shells of the nanotubes was suggested, preventing their pull-out from the matrix [24]. Chen and Akono [113] found that for MK-based K-GP the bridging effects started to dominate from 1.5 wt.% of MWCNTs. Reinforcing GP with CNFs also acts in a similar way to MWCNTs, but the only drawback is that porosity is reduced due to the reduction in the fraction of micropores with an increase in the size of macropores, caused by the high viscosity of the paste [115].

A nano-reinforcement that has been used for GP is nanoclay. Nanoclays are crystal-lattice-layered mineral silicates consisting of 1 nm thick two-dimensional layers made of two tetrahedral silica plates fused to an edge-shaped octahedral sheet of alumina or magnesia [116], for the most part, they are highly hydrophilic [100].

A type of nanoclay similar to kaolin is nano-halloysite ($Al_2Si_2O_5 \cdot 2H_2O$), with hollow nanotube morphology [117]. The optimal addition content ranged from 2 [55] to 6 wt.% [91], generating several benefits: densification [55, 91], increased compressive [55, 91], flexure [55, 91] and tensile strengths (the latter with a gain of 29%) [91].

Nanoclay reduces the setting time, due to acting as nucleation sites and its nano filling effect [91]. A potential application for nanoclay is for high temperatures [55, 91], since after 200°C, the GP strength increased proportionally with the level and addition, both due to the formation of more products and the greater thermal stability of these products [91].

Calcination of nanoclay between 600 and 800°C lead to the destruction of the crystalline structure and formation of an amorphous phase, generating nano-metakaolin (NMK) [116]. Hassaan *et al.* [106] showed that NMK promoted the distortion of the intercalation of kaolinite chains and, consequently, increased its reactivity. Replacing part of the kaolin with NMK, even at levels as low as 1 wt.%, improves the morphological structure since NMK acts as a nucleation material for the geopolymerization, in addition to being a source of amorphous aluminum-silicate [16, 106, 116] and compressive strength of 80 MPa can be obtained [16].

2.7. Literature Findings

Publications about geopolymers date from 1981, however it is from the last 10 years that the number of publications has increased strongly (Figure 2.1(b)).

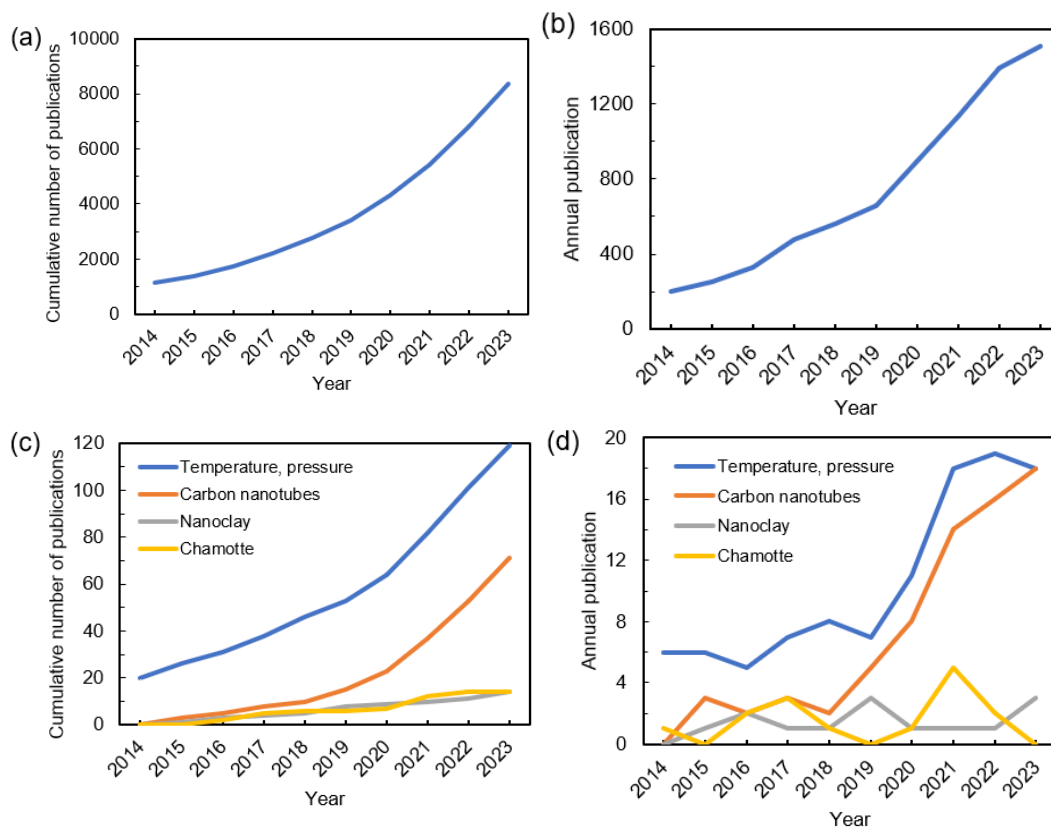


Figure 2.1 – Bibliographical production referring to geopolymers over time showing (a) number of total publications and (b) annual production; (c) quantity of work on specific subjects and (d) annual production of specific subjects. (Data extracted by consultation in Periodicals CAPES on December 21, 2023).

The evaluation of GP under temperature and/or pressure conditions aroused interest after 20 years, probably motivated by the interest in replacing Portland cement for oil well cementing applications. Research that aimed to evaluate the addition of refractory particle (chamotte) only began to be published in 2014 and one year later, started the publications on additions of carbon nanotubes and nanoclay. The number of publications on GP cured under temperature and/or pressure and also on the addition of carbon nanotubes is increasing (Figure 2.1(c)), but studies on the addition of chamotte and nanoclay are still scarce (Figure 2.1(d)).

In Figure 2.2 some results from the literature for GP, alkali-activated cement and PC are presented. Tables 2.1 and 2.2 present the formulations and curing conditions used by the authors.

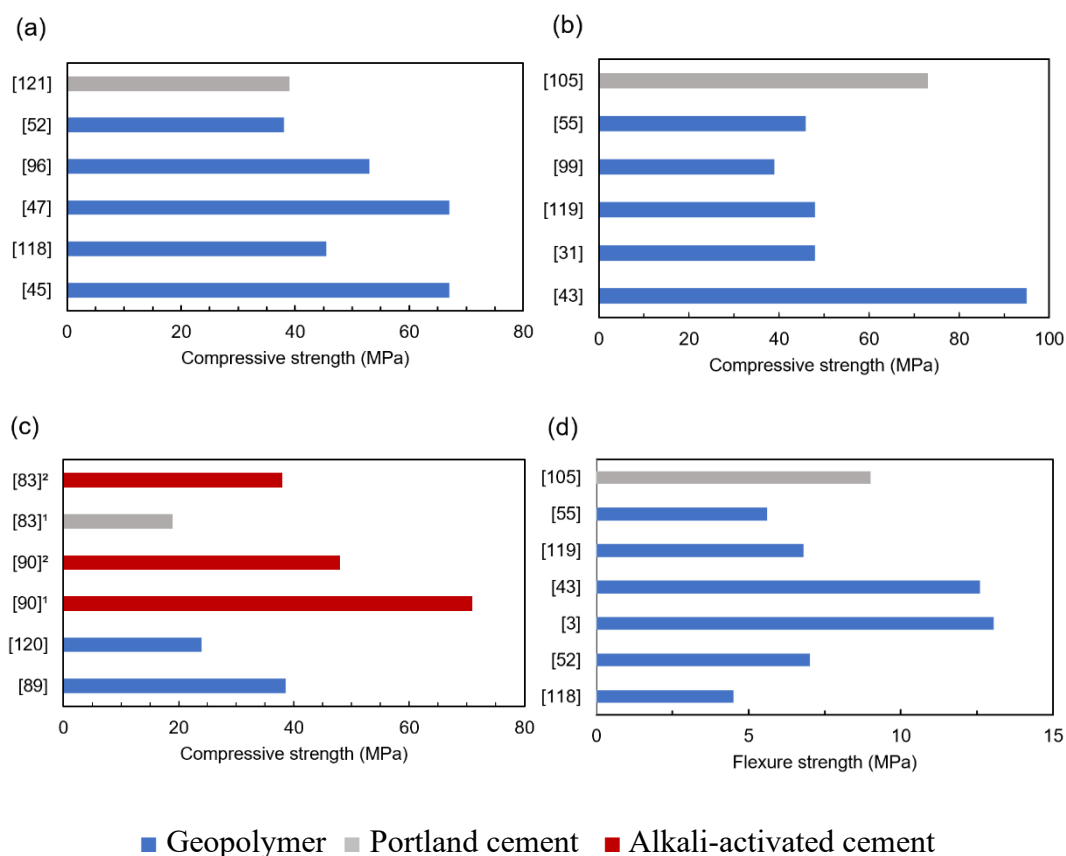


Figure 2.2 - Values obtained in the literature for geopolymer, Portland Cement and alkali-activated cement referring to compressive strength after curing (a) at room temperature (21 to 28°C), (b) at temperatures above 50°C, (c) at temperature and pressure and; (d) flexural strength values.

As can be seen in Figure 2.2(a), the performance of GP is similar to or surpasses PC under all curing conditions and/or formulations adopted. In Lahoti *et al.* [45] high strength was obtained because the Si:Al ratio was optimized as well as the concentration of the alkali solution. Kuenzel *et al.* [64] showed that sand can be an effective reinforcement, however it is worth highlighting that the curing temperature was only 22°C, a value at which it does not suffer degradation. It is possible to see that in Shekhovtsova *et al.* [118] dolomite does not perform as well as sand, but it is worth noting that curing was under 100% RH, which is unfavorable for FA-GP. The results obtained by Xiang *et al.* [96] show the importance of increasing the content of fine particles for reducing porosity and increasing strength. Although Rovnanik and Safrankova [52] used chamotte, the effect was not

as significant when curing at room temperature (Figure 2.2(a)) compared to curing at a higher temperature (Figure 2.2(b)).

Figure 2.2(b) shows that the addition of chamotte to GP made it possible to surpass the performance of PC with CNTs by almost 30%. The addition of nanoclay [55, 119] allowed GP to have performance comparable to GPC [31], even with the same performance even after curing at 80°C [55], which for a plain GP would already have deteriorated properties. The addition of nanoclay also allowed better performance compared to nanoalumina [99], probably as a result of the greater densification and interlocking effect between nanoclay and binder, due to its tubular morphology.

However, for applications under temperature and pressure (Figure 2.2(c)) alkali-activated cement outperformed PC and GP. Although GP showed better performance than PC, the values are much lower than those obtained for alkali-activated cement. In Liu *et al.* [120] this can be explained by the absence of the use a reinforcement. Paiva *et al.* [89] obtained better GP performance compared to Liu *et al.* [120], due to the addition of microsilica, but the gains may not have been enhanced as the pressure and temperature used were much lower than in researches that used alkali-activated slag.

The performance of GPs in bending (Figure 2.2(d)) showed that GP with chamotte [3, 43] when cured at a temperature equal or greater than 50°C outperformed PC with CNT [105] by approximately 35%, showing that both the temperature and the addition of refractory particles made it possible to optimize the properties of the GP through the refinement of the microstructure and the barrier effect to crack propagation carried out by the chamotte particles. The low performance in Shekhovtsova *et al.* [118] may be due to alkali leaching as the temperature below 40°C allowed more time for the FA-GP to lose alkali to the aqueous medium. The performance presented in Rovnanik and Safrankova [52] is due to the fact that curing at 22°C does not allow maximum densification of the MK-GP microstructure. The addition of nanoclay to GP [55, 119] made it possible to obtain good performance compared to the addition of chamotte at 22°C [52], with the performance in Assaedi *et al.* [55] being lower than the other two because the higher temperature favors faster water evaporation.

Table 2.1 - Formulations and curing conditions for the results indicated in Figure 2.2, for geopolymers.

Reference	Aluminosilicate source	Adittion	Alkali solution	Curing conditions
[45]	Metakaolin	-	Na-based	25°C, 7 days
[118]	Fly ash - F	Dolomite sand	Na-based	25°C, 100 % RH, 28 days
[47]	Metakaolin	Sand	Na-based	22°C, 75 days
[96]	Metakaolin	Sand Fuller-FS	Na-based	20°C, 28 days
[52]	Metakaolin	Chamotte	Na-based	22°C, 28 days
[3]	Metakaolin	Chamotte	K-based	50°C, 24 h
[43]	Metakaolin	Chamotte	K-based	60°C, 4 h
[31]	Fly ash - F	Crushed stone, sand	Na-based	60°C, 24 h
[119]	Fly ash - F	Reactive alumina, nanoclay	Na-based	60°C, 48 h
[99]	Metakaolin	Nanoalumina	Na-based	80°C, 24 h
[55]	Fly ash - F	Nanoclay	Na-based	80°C, 24 h
[89]	Metakaolin	Microsilica	K-based	50°C, 10 MPa, 48 h
[120]	Fly ash - F	-	Na+K-based	75°C, 20 MPa, 3 days

Table 2.2 - Formulations and curing conditions for the results indicated in Figure 2, for Portland cement and alkali-activated systems.

Reference	Binder	Adittion	Alkali solution	Curing conditions
[121]	Brazilian CP-V Portland Cement	Fly ash-C, sand	-	21°C, 14 days
[105]	Brazilian CP-V Portland cement	CNTs	-	60°C, 24 h
[90] ¹	Fly ash - C	-	Na-based	90°C, 35 MPa, 7 days
[90] ²	Fly ash - C	-	Na-based	125°C, 35 MPa, 7 days
[83] ¹	Class G Portland cement	-	-	130°C, 20 MPa, 24 h
[83] ²	Fly ash - C	-	Na-based	130°C, 20 MPa, 24 h

Due to the fact that the microstructure strongly impacts the performance of the GP in terms of durability and mechanical properties, some results found in the literature focusing on the addition of NPs are presented. Figure 2.3 shows the effect obtained by adding nanoclay, reported in Assaedi *et al.* [55].

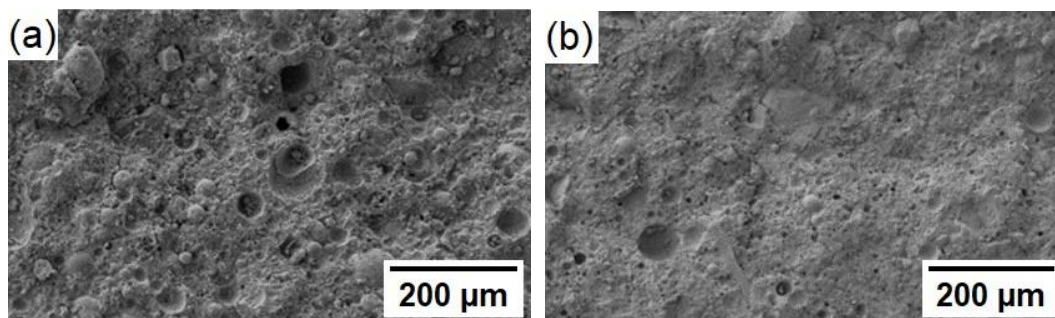


Figure 2.3 - Microstructure obtained in Assaedi *et al.* [55] for:

(a) plain geopolymer; (b) 2 %wt. nanoclay.

As can be seen in Figure 2.3, a denser microstructure was formed due to the addition of nanoclay and, in still, fewer FA particles are visible. This demonstrates the role of both nanofilling and product nucleation sites played by nanoclay. The same effect was also observed when adding CNTs (Figure 2.4), as evaluated by Saafi *et al.* [24].

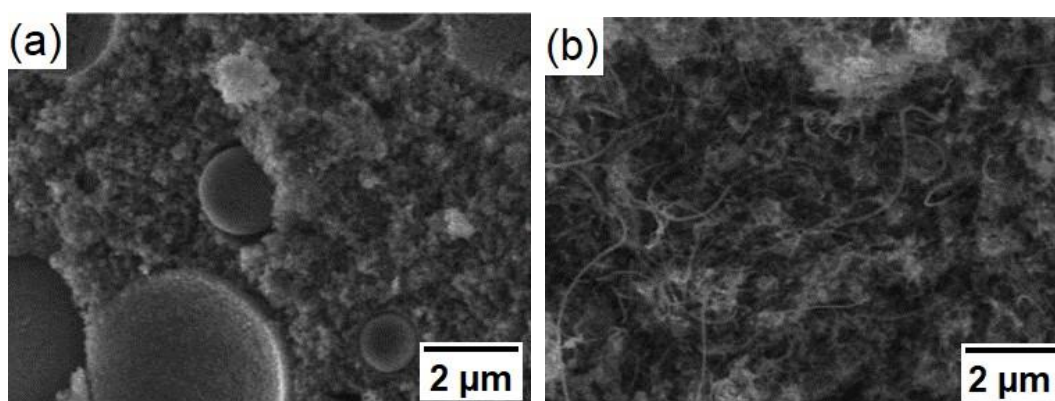


Figure 2.4 - Microstructure obtained by Saafi *et al.* [24] for:

(a) plain geopolymer; (b) 0.1 wt.% MWCNTs.

But in addition to these roles, CNTs can also act as bridges between cracks. This was verified by Chen and Akono [113] and is presented in Figure 2.5:

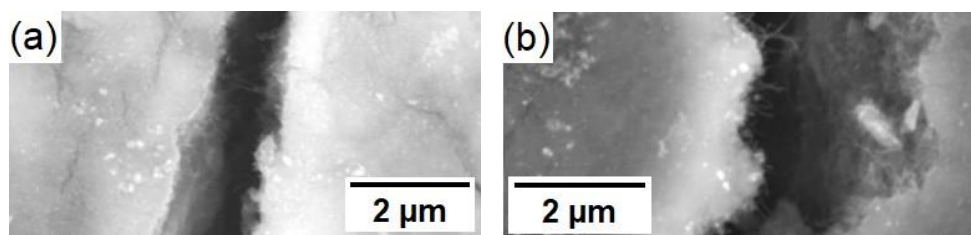


Figure 2.5 - MWCNTs acting as crack bridging with a concentration of (a) 0.3 % wt. and (b) 1.5 % wt. [113].

As can be seen in Figure 2.5, even at concentrations of 0.3 %wt. MWCNTs acted as fibrous reinforcements.

2.8. Applications

The applications of GPs are diverse, as they are determined by the Si:Al atomic ratio, which governs the chemical, physical and mechanical properties, including: fire-resistant components, sealants, encapsulation of toxic and radioactive waste [4]. MK-GP has been successfully introduced into several markets, including paints, mortar and ceramic-like products [12].

There are already options on the market to purchase aluminosilicate sources for GP production: Geo-Pol, a Brazilian company, developed binder with Si:Al=2 from natural geological materials; In the United Kingdom, Banah has the so-called banahCEM in its product line. In addition, there are options available for alkali hydroxide solutions and additives for GP formulations, sold by Woellner. Most GP applications aim to replace PC, such as: mortars for reinforcing beams [69]; permeable concretes with better properties, mainly due to the excellent binding property of GP [50]; acoustic insulation [122]; thermal insulation with better performance than PCC, attributed to the formation of a structure with more insulating pores [123].

One of the most notable applications is the use of GP as a refractory material. Keanel *et al.* [124] developed GP composites with the addition of chopped basalt fibers and low-melting glass, which can be made on scale and manufactured using high shear, similar to cements, but with the properties of ceramics after exposure to

a temperature of the order of 1200°C, called amorphous self-healing GP.

A recent approach to GP synthesis, which is similar to PC synthesis, is based on the one-part GP concept in which a reactive geopolymer precursor obtained by direct calcination of kaolin is mixed with a solution made of Na/K hydroxides and water [66, 110].

The addition of fibers to GP can result in an increase in the number of pores [89], due to the increase in the viscosity of the mixture [3]. However, Gulsan *et al.* [125] showed that the combined use of nanosilica and steel fibers increased the adhesion of the fibers to the GP, reducing porosity. In the same sense, Malik *et al.* [68] when combining PVA fibers with silica nanoparticles in the GP, was found that the NPs accelerated the geopolymeric reaction, leading to more complex 3-dimensional polymeric structures, densifying the microstructure and refining the pores. Compact and refined microstructure together with greater fiber-GP connection, improves flexural strength [98].

NPs emerge as an alternative to optimize some GP properties or make them suitable for some applications. The use of CNFs to manufacture heating elements in self-heating deicing pavement is shown to be advantageous in terms of chemical stability, electrical performance and heating efficiency; in the application of electromagnetic shielding, they lead to greater absorption efficiency; as well as for thermoelectric devices [107]. In the latter case, the use of SWCNTs allowed the creation of a super-efficient electrically conductive network [110]. The results of rheological tests on GPs with MWCNTs conducted by Chen and Akono [113] demonstrated the potential for application in 3D printing.

The use of nanoreinforcements, such as CNTs/CNFs, is promising due to the elastic modulus in the order of TPa and tensile strength in the order of GPa. Added to this, the surfaces of these NPs constitute potential sites for chemical and physical interactions, indicating the potential for crack bridging and increased load transfer [100].

Some authors have demonstrated the effect of NPs in adding some functionalities to GP. Syamsidar *et al.* [126] and Wardani *et al.* [127] showed that the inclusion of nano- TiO_2 enabled the development of material for functional surface applications, such as antifouling bricks. Nanoclay, depending on its structure, makes it possible to contain chemical agents (such as anticorrosive and antibacterial agents) providing GP with additional functions or the encapsulation of

aluminosilicate microcores to reduce the GP setting time [128]. More efficient control of the GP mortar setting time is essential for applications at high temperatures, such as oil wells plugging, as the paste remains workable for 1 to 2 h at temperatures in the range of 50 to 150°C, however the GP set in 10 to 30 min at this temperature and the encapsulation of the source of aluminosilicate ensures a significantly extended setting time.

2.9. References

1. Davidovits, J. (2011). *Geopolymers – chemistry & applications*. 3 ed. Saint-Quentin: Institute Géopolymère; p. 6.
2. Hu, W., Ma, Y., Koehler, M., Gong, H., Huang, B. (2021). Mix design optimization and early strength prediction of unary and binary geopolymer from multiple waste streams. *Journal of Hazardous Materials*, 403.
3. Musil, S.S., Kriven. W.M. (2014). In Situ Mechanical Properties of Chamotte Particulate Reinforced, Potassium Geopolymer. *J. Am. Ceram. Soc.*, 97 [3] 907–915.
4. Davidovits, J. (2018). Why Alkali-Activated Materials (AAM) are Not Geopolymers, Technical Paper #25, Geopolymer Institute Library. Disponível em: <www.geopolymer.org>.
5. Davidovits, J. (2008). *Geopolymer Chemistry and Applications*. Geopolymer Institute.
6. Babae, M; Khan, M. S. H; Castel, A. (2018). Passivity of embedded reinforcement in carbonated low-calcium fly ash-based geopolymer concrete. *Cement and Concrete Composites* 85. pp. 32-43.
7. Chen, Z; Wu, S; Xiao, Y; Zeng, W; Yi, M; Wan, J. (2016). Effect of hydration and silicone resin on Basic Oxygen Furnace slag and its asphalt mixture. *J. Clean. Prod.* 112, pp. 392-400.
8. Ma, Y; Ye, G. (2015). The shrinkage of alkali activated fly ash. *Cement and Concrete Research*, 68, 75–82.
9. Kamseu, E., Rizzuti, A., Leonelli, C., Perera, D. (2010). Enhanced thermal stability in K₂O-metakaolin-based geopolymer concretes by Al₂O₃ and SiO₂ fillers addition. *J Mater Sci* 45. 1715–1724.
10. Brandvold, A.S., Al-Chaar, G.K., Kriven, W.M. (2023). Isolating the effects of thixotropy in geopolymer pastes. *Journal of the American Ceramic Society*. pp. 2797-2807.
11. Komljenovic, M., Bascarevi, Z., Bradi, V. (2010). Mechanical and microstructural properties of alkali-activated fly ash geopolymers. *Journal of Hazardous Materials* 181. 35-42.
12. Davidovits, R., Pelegris, C., Davidovits, J. (2019), Standardized Method in Testing Commercial Metakaolins for Geopolymer Formulations, Technical Paper#26-MK-testing, Geopolymer Institute Library, www.geopolymer.org.

13. Ameri, F., Shoaiei, P., Zareei, S.A., Behforouz, B. (2019). Geopolymers vs. alkali-activated materials (AAMs): A comparative study on durability, microstructure, and resistance to elevated temperatures of lightweight mortars. *Construction and Building Materials* 222. 49–63.
14. Xin, L; Jinyu, X; Erlei, B; Weimin, L. (2012). Systematic study on the basic characteristics of alkali-activated slag-fly ash cementitious material system. *Construction and Building Materials* 29. pp. 482–486.
15. Provis, J. L. (2014). Geopolymers and other alkali activated materials: why, how, and what? *Materials and Structures*. n. 47. pp. 11–25.
16. Sikandar, M. A; Jo, B. W; Baloch, Z; Khan, M. A. (2019). Properties of Chemically Synthesized Nano-geopolymer Cement based Self-Compacting Geopolymer Concrete (SCGC). *Journal of Wuhan University of Technology-Mater. Sci.* Vol.34, n.1.
17. Yamany, H. E; Salamawy, M. A; Assal, N. T. (2018). Microstructure and mechanical properties of alkali-activated slag mortar modified with latex. *Construction and Building Materials* 191. pp. 32–38.
18. Farhan, N. A., Sheikh, M. N., Hadi, M. N. S. (2019). Investigation of engineering properties of normal and high strength fly ash based geopolymer and alkali-activated slag concrete compared to ordinary Portland cement concrete. *Construction and Building Materials*, 196, 26–42.
19. Chi, M. (2013). Effects of dosage of alkali-activated solution and curing conditions on the Properties and durability of alkali-activated slag concrete. *Construction and Building Materials* 35 (2012) 240–245
20. Ahdaya, M; Imqam, A. (2019). Fly ash Class C based geopolymer for oil well cementing. *Journal of Petroleum Science and Engineering* n. 179. pp. 750–757.
21. Mithun, B.M; Narasimhan, M.C. (2016) Performance of alkali activated slag concrete mixes incorporating copper slag as fine aggregate. *Journal of Cleaner Production* 112. pp. 837-844.
22. Ye, H; Cartwright, C; Rajabipour, F; Radlinska. (2017). Understanding the drying shrinkage performance of alkali-activated slag mortars. *Cement and Concrete Composites* 76. pp. 13-24.
23. Komljenović, M; Baščarević, M. Z; Marjanović, N; Nikolic, V. (2013). External sulfate attack on alkali-activated slag. *Construction and Building Materials* 49. 31–39.
24. Saafi, M., Andrew, K., Tang, P.L., McGhon, D., Taylor, S., Rahman, M., Yang, S., Zhou, X. (2013). Multifunctional properties of carbon nanotube/fly ash geopolymeric nanocomposites. *Construction and Building Materials* 49. 46-55.
25. Slaty, F; Houry, H; Rahier, H; Wastiels, J. (2015). Durability of alkali activated cement produced from kaolinitic clay. *Applied Clay Science*, 104. pp. 229–237.
26. Kanesan, D; Irawan, S; Ridha, S; Chandran, D; Azhar, N. A. B. (2018). The suitability of fly ash based geopolymer cement for oil well cementing applications: A review. *ARPN Journal of Engineering and Applied Sciences*. VOL. 13, n. 20, pp. 8296-8315.

27. Junaid, M. T; Khennane, A; Kayali, O; Sadaoui, A; Picard, D; Fafard, M. (2014). Aspects of the deformational behaviour of alkali activated fly ash concrete at elevated temperatures. *Cement and Concrete Research* 60. pp. 24–29.
28. Pacheco-Torgal, F; Moura, D., Ding, Y., Jalali, S. (2011). Composition, strength and workability of -alkali-activated metakaolin based mortars. *Constr. Build. Mater.* 25. pp. 3732–3745.
29. Salehi, S., Khattak, M.J., Bwala, A.H., Karbalaei, F. (2017). Characterization, morphology and shear bond strength analysis of geopolymers: Implications for oil and gas well cementing applications. *Journal of Natural Gas Science and Engineering* 38. 323-332.
30. Zhang, H. Y; Kodur, V; Wu, B; Yan, J; Yuan, Z. S. (2018). Effect of temperature on bond characteristics of geopolymer concrete. *Construction and Building Materials*, 163. pp. 277–285.
31. Sarker, P.K., Haque, R., Ramgolam, K.V. (2013). Fracture behaviour of heat cured fly ash based geopolymer concrete. *Materials and Design* 44. 580–586.
32. Ding, Y., Shi, C-J., Li, N. (2018). Fracture properties of slag/fly ash-based geopolymer concrete cured in ambient temperature. *Construction and Building Materials* 190. 787–795.
33. Yang, T; Zhu, H; Zhang, Z. (2017). Influence of fly ash on the pore structure and shrinkage characteristics of metakaolin-based geopolymer pastes and mortars. *Construction and Building Materials*, 153. pp. 284–293.
34. Guades, E.J. (2016). Experimental investigation of the compressive and tensile strengths of geopolymer mortar: The effect of sand/fly ash (S/FA) ratio. *Construction and Building Materials* 127. 484–493.
35. Kamali, M., Khalifeh, M., Saasen, A., Godøy, R., Delabroy, L. (2021). Alternative setting materials for primary cementing and zonal isolation – Laboratory evaluation of rheological and mechanical Properties. *Journal of Petroleum Science and Engineering*, 201.
36. Brandvold, A.S., Trindade, A.C.C., Kriven, W.M. (2023). Rheological assessment of metakaolin-based geopolymer composites through squeeze flow. *Journal of the American Ceramic Society*. pp. 4038-4051.
37. Park, S.M., Khalid, H.R., Seo, J.H., Yoon, H.N., Son, H.M., Kim, S.H., Lee, N.K., Lee, H.K., Jang, J.G. (2018). Pressure-Induced Geopolymerization in Alkali-Activated Fly Ash. *Sustainability*, 10.
38. Gao, X; Yuan, B; Yu, Q. L; Brouwers, H. J. H. (2017). Characterization and application of municipal solid waste incineration (MSWI) bottom ash and waste granite powder in alkali activated slag. *Journal of Cleaner Production* 164. pp. 410-419.
39. Davoodabadi, M., Liebscher, M., Hampel, S., Sgarzi, M., Rezaie, A.B., Wolf, D., Cuniberti, G., Mechtcherine, V., Yang, J. (2021). Multi-walled carbon nanotube dispersion methodologies in alkaline media and their influence on mechanical reinforcement of alkali-activated nanocomposites. *Composites Part B* 209.

40. Alanazi, H., Zhang, D., Yang, M., Gao, Z. (2017). Early strength and durability of metakaolin-based geopolymer concrete. *Magazine of Concrete Research*, 69(1), 46–54
41. ASTM C618. Standard Specification for Coal Fly Ash and Raw or Calcined Natural Pozzolan for Use in Concrete. Version: 2022.
42. Olawalw, M. D. (2013). Syntheses, characterization and binding strength of geopolymers: A review. *International Journal of Materials Science and Applications*, 2(6), 185-193.
43. Kohout, J., Koutník, P., Hájková, P., Kohoutová, E., Soukup, A. (2022). Effect of Different Types of Aluminosilicates on the Thermo-Mechanical Properties of Metakaolinite-Based Geopolymer Composites. *Polymers* 2022, 14, 4838.
44. Djangang, C.N., Tchamba, A.B., Kamseu, E., Melo, U.C., Elimbi, A., Ferrari, A.M., Leonelli, C. (2014). Reaction sintering and microstructural evolution in metakaolinmetastable alumina composites. *J Therm Anal Calorim* (2014) 117:1035–1045.
45. Lahoti, M; Wong, K. K; Yang, E-H; Tan, K. H. (2018). Effects of Si/Al molar ratio on strength endurance and volume stability of metakaolin geopolymers subject to elevated temperature. *Ceramics International*, 44. pp. 5726–5734.
46. Kuenzel, C., Neville, T. P., Donatello, S., Vandeperre, L., Boccaccini, A. R., Cheeseman, C. R. (2013). Influence of metakaolin characteristics on the mechanical properties of geopolymers. *Applied Clay Science*, 83–84 (2013), 308–314.
47. Kuenzel, C., Li, L., Vandeperre, L., Boccaccini, A.R., Cheeseman, C.R. (2014). Influence of sand on the mechanical properties of metakaolin geopolymers. *Construction and Building Materials* 66. 442–446.
48. Chen, S; Wu, C; Yan, D. (2019). Binder-scale creep behavior of metakaolin-based geopolymer. *Cement and Concrete Research* 124.
49. Singh, G. V. P. B., Subramaniam, K. V. L. (2019). Influence of processing temperature on the reaction product and strength gain in alkali-activated fly ash. *Cement and Concrete Composites*, 95, 10–18.
50. Sun, Z., Lin, X., Vollpracht, A. (2018). Pervious concrete made of alkali activated slag and geopolymers. *Construction and Building Materials* 189. 797–803.
51. Ma, Y; Hu, J; Ye, G. (2013). The pore structure and permeability of alkali activated fly ash. *Fuel* 104. pp. 771–780.
52. Rovnanik, P., Safrankova, K. (2016). Thermal Behaviour of Metakaolin/Fly Ash Geopolymers with Chamotte Aggregate. *Materials* 2016, 9, 535.
53. Papa, E., Medri, V., Amari, S., Manaud, J., Benito, P., Vaccari, A., Landi, E. (2018). Zeolite-geopolymer composite materials: Production and characterization. *Journal of Cleaner Production*, 171, 76-84.
54. Hadi, M. N. S., Farhan, N. A., Sheikh, M. N. (2017). Design of geopolymer concrete with GGBFS at ambient curing condition using Taguchi method. *Construction and Building Materials*, 140, 424–431.

55. Assaedi, H., Shaikh, F.U.A., Low, I.M. (2016). Effect of nano-clay on mechanical and thermal Properties of geopolymer. *Journal of Asian Ceramic Societies* 4. 19–28.
56. Kuenzel, C; Vandeperre, L. J; Donatello, S; Boccaccini, A. R; Cheeseman, C. (2012). Ambient Temperature Drying Shrinkage and Cracking in Metakaolin-Based Geopolymers. *J. Am. Ceram. Soc.*, 95 [10] pp. 3270–3277.
57. Ling, Y., Wang, K., Wang, X., Hua, S. (2019). Effects of mix design parameters on heat of geopolymerization, set time, and compressive strength of high calcium fly ash geopolymer. *Construction and Building Materials*, 228.
58. Zhong, Q., Tian, X., Xie, G., Luo, X., Peng, H. (2022). Investigation of Setting Time and Microstructural and Mechanical Properties of MK/GGBFS-Blended Geopolymer Pastes. *Materials*, 15.
59. Liang, G., Yao, W., She, A. (2023). New insights into the early-age reaction kinetics of metakaolin geopolymer by ¹H low-field NMR and isothermal calorimetry. *Cement and Concrete Composites*, 137.
60. González-García, D. M., Téllez-Jurado, L., Jiménez-Álvarez, F. J., Zarazua-Villalobos, L., Balmori-Ramírez, H. (2022). Evolution of a natural pozzolan-based geopolymer alkalinized in the presence of sodium or potassium silicate/hydroxide solution. *Construction and Building Materials*, 321.
61. Zivica, V; Balkovic, S; Drabik, M. (2011). Properties of metakaolin geopolymer hardened paste prepared by high-pressure compaction. *Construction and Building Materials* 25. pp. 2206–2213.
62. Lizcano, M., Kim, H. S., Basu, S., Radovic, M. (2012). Mechanical properties of sodium and potassium activated metakaolin-based geopolymers. *J Mater Sci*, 47, 2607–2616.
63. Peng, H., Cui, C., Cai, C.S., Liu, Y., Liu, Z. (2019). Microstructure and microhardness property of the interface between a metakaolin/GGBFS-based geopolymer paste and granite aggregate. *Construction and Building Materials* 221. 263–273.
64. Rouyer, J; Benavent, V; Frizon, F; Poulesquen, A. (2017). Influence of geopolymer formulation parameters on the elastic and porous properties over a one-year monitoring. *Materials Letters*, 207. pp. 121–124.
65. Bouguermouh, K; Bouzidi, N; Mahtout, L; Pérez-Villarejo, L; Martínez-Cartas, M. L. (2017). Effect of acid attack on microstructure and composition of metakaolin-based geopolymers: The role of alkaline activator. *Journal of Non-Crystalline Solids*, 463. pp. 128–137.
66. Kolousek, D., Brus, J., Urbanova, M., Andertova, J., Hulinsky, V., Vorel, J. (2007). Preparation, structure and hydrothermal stability of alternative (sodium silicate-free) geopolymers. *J Mater Sci* 42. 9267–9275.
67. Muzek, M.N., Zelic, J., Jozic, D. (2012). Microstructural Characteristics of Geopolymers Based on Alkali-Activated Fly Ash. *Chem. Biochem. Eng. Q.* 26 (2). 89–95.

68. Malik, M.A., Sarkar, M., Xu, S., Li, Q. (2019). Effect of PVA/SiO₂ NPs Additive on the Structural, Durability, and Fire Resistance Properties of Geopolymers. *Appl. Sci.* 2019, 9, 1953.
69. Ferone, C., Colangelo, F., Roviello, G., Asprone, D., Menna, C., Balsamo, A., Prota, A., Cioffi, R., Manfredi, G. (2013). Application-Oriented Chemical Optimization of a Metakaolin Based Geopolymer. *Materials*, 6, 1920-1939.
70. Borges, P. H. R; Banthia, N; Alcamand, H. A; Vasconcelos, W. L; Nunes, E. H. M. (2016). Performance of blended metakaolin/blastfurnace slag alkali-activated mortars. *Cement and Concrete Composites*, 71. pp. 42-52.
71. Ahmad, M., Rashid, K., Hameed, R., Haq, E. U., Farooq, H., Ju, M. (2022). Physico-mechanical performance of fly ash based geopolymer brick: Influence of pressure - temperature – time. *Journal of Building Engineering*, 50.
72. Ranjbar, N., Kashefi, A., Ye, G., Mehrali, M. (2020). Effects of heat and pressure on hot-pressed geopolymer. *Construction and Building Materials*, 231.
73. Saludung, A., Azeyanagi, T., Ogawa, Y., Kawai, K. (2021). Alkali leaching and mechanical performance of epoxy resin-reinforced geopolymer composite. *Materials Letters*, 304.
74. Hoang, M.D., Do, Q.M., Le, V.Q. (2020). Effect of curing regime on properties of red mud-based alkali activated materials. *Construction and Building Materials*, 259.
75. Zhang, M., Zhao, M., Zhang, G., Mann, D., Lumsden, K., Tao, M. (2016). Durability of red mud-fly ash based geopolymer and leaching behavior of heavy metals in sulfuric acid solutions and deionized water. *Construction and Building Materials*, 124, 373–382.
76. Sun, Z., Vollpracht, A. (2020). Leaching of monolithic geopolymer mortars. *Cement and Concrete Research*, 136.
77. Ukrainczyk, N. (2021). Simple Model for Alkali Leaching from Geopolymers: Effects of Raw Materials and Acetic Acid Concentration on Apparent Diffusion Coefficient. *Materials*, 14, 1425
78. Łach, M., Korniejenko, K., Walter, J., Stefańska, A., Mikuła, J. (2020). Decreasing of Leaching and Improvement of Geopolymer Properties by Addition of Aluminum Calcium Cements and Titanium Oxide. *Materials*, 13, 495.
79. Giassudin, H. M; Sanjayan, J. G; Ranjith, P. G. (2013). Strength of geopolymer cured in saline water in ambient conditions. *Fuel* n. 107. pp. 34–39.
80. Kovarik, T., Kullova, L., Rieger, D. (2016). Production of refractory chamotte particle-reinforced geopolymer composite. *IOP Conf. Series: Materials Science and Engineering* 123.
81. Si, R; Dai, Q; Guo, S; Wang, J. (2020). Mechanical property, nanopore structure and drying shrinkage of metakaolin-based geopolymer with waste glass powder. *Journal of Cleaner Production*, 242. pp. 1-12.

82. Alvi, M. A. A; Khalifeh, M; Agonafir, M. B. (2020). Effect of nanoparticles on properties of geopolymers designed for well cementing applications. *Journal of Petroleum Science and Engineering* 191. pp. 107-128.
83. Ridha, S; Abd Hamid, A. I; Abdul Halim, A. H; Zamzuri, N. A. (2018). Elasticity and expansion test performance of geopolymer as oil well cement. *IConCEES 2017. IOP Conf. Series: Earth and Environmental Science* 140. pp. 1-6.
84. Zhao, J., Liebscher, M., Michel, A., Junger, D., Trindade, A.C.C., Silva, F.A., Mechtcherine, V. (2021). Development and testing of fast curing, mineral-impregnated carbon fiber (MCF) reinforcements based on metakaolin-made geopolymers. *Cement and Concrete Composites*, 116.
85. Muñoz-Villareal, M. S; Manzano-Ramírez, A; Sampieri-Bulbarela, S; Gasca-Tirado, J. R; Reyes-Araiza, J. L; Rubio-Ávalos, J. C; Pérez-Bueno, J. J; Apatiga, L. M; Zaldivar-Cadena, A; Amigó-Borrás, V. (2011). The effect of temperature on the geopolymerization process of a metakaolin-based geopolymer. *Materials Letters* 65. pp. 995–998.
86. Kajarathan, S., Karthikan, S., Nasvi, M.C.M. (2015). Geopolymer as Well Cement and its Mechanical Behaviour with Curing Temperature. In *Proceedings of the 6th International Conference on Structural Engineering and Construction Management 2015, Kandy, Sri Lanka, 11–13 December 2015*
87. Samantasinghar, S., Singh, S. (2020). Effects of curing environment on strength and microstructure of alkali-activated fly ash-slag binder. *Construction and Building Materials*, 235.
88. Salehi, S., Khattak, M.J., Rizvi, H., Karbalaei, S.F., Kiran, R. (2017). Sensitivity analysis of fly ash geopolymer cement slurries: Implications for oil and gas wells cementing applications. *Journal of Natural Gas Science and Engineering* 37. 116-125.
89. Paiva, M. D. M; Silva, E. C. C. M; Melo, D. M. A; Martinelli, A. E; Schneider, J. F. (2018). A geopolymer cementing system for oil wells subject to steam injection. *Journal of Petroleum Science and Engineering* 169. pp. 748–759.
90. Khalifeh, M; Saasen, A; Vralstad, T; Hodne, H. (2014). Potential utilization of class C fly ash-based geopolymer in oil well cementing operations. *Cement & Concrete Composites* n. 53. pp. 10–17.
91. John, S.K., Nadir, Y., Cascardi, A., Arif, M.M., Girija, K. (2023). Effect of addition of nanoclay and SBR latex on fly ash-slag geopolymer mortar. *Journal of Building Engineering* 66.
92. Nikolić, I; Karanović, L; Častvan, I. J; Radmilović, V; Slavko Mentus; S; Radmilović, V. (2014). Improved compressive strength of alkali activated slag upon heating. *Materials Letters* 133. pp. 251-254.
93. Ai, T., Zhong, D., Zhang, Y., Zong, J., Yan, X., Niu, Y. (2021). The Effect of Red Mud Content on the Compressive Strength of Geopolymers under Different Curing Systems. *Buildings*, 11, 298.
94. Bai, Y., Guo, W., Wang, J., Xu, Z., Wang, S., Zhao, Q., Zhou, J. (2022). Geopolymer bricks prepared by MSWI fly ash and other solid wastes: Moulding pressure and curing method optimisation. *Chemosphere*, 307.

95. Trindade, A.C.C., Silva, F.A., Alcamandb, H.A., Borges, P.H.R. (2017). On The Mechanical Behavior of Metakaolin Based Geopolymers Under Elevated Temperatures. *Materials Research*. 2017; 20(Suppl. 2): 265-272.
96. Xiang, J., Liu, L., Cui, X., He, Y., Zheng, G., Shi, C. (2019). Effect of Fuller-fine sand on rheological, drying shrinkage, and microstructural properties of metakaolin-based geopolymer grouting materials. *Cement and Concrete Composites* 104.
97. Keane, P.F., Kriven, W.M. (2019). Microstructure And Flexure Strengths Of Dolomite Particulate reinforced Geopolymer Composites. *Proceedings of the 42nd International Conference on Advanced Ceramics and Composites: Ceramic Engineering and Science Proceedings Volume 39, Issue 3*
98. Rabiaa, E., Mohamed, R. A. S., Sofi, W. H., Tawfik, T.A. (2020). Developing Geopolymer Concrete Properties by Using Nanomaterials and Steel Fibers. *Advances in Materials Science and Engineering*.
99. Zidi, Z; Ltifi, M; Ayadi, Z. B; El-Mir, L. (2019). Synthesis of nano-alumina and their effect on structure, mechanical and thermal properties of geopolymer. *Journal of Asian Ceramic Societies*, 7:4, pp. 524-535.
100. Sanchez, F., Sobolev, K. (2010). Nanotechnology in concrete – A review. *Construction and Building Materials* 24. 2060–2071.
101. Rocha, V.V., Ludvig, P. (2020). Influence of Carbon Nanotubes on the Mechanical Behavior and Porosity of Cement Pastes Prepared by A Dispersion on Cement Particles in Isopropanol Suspension. *Materials* 2020, 13, 3164.
102. Yan, S; He, P; Jia, D; Yang, Z; Duan, X; Wang, S; Zhou, Y. (2015). In situ fabrication and characterization of graphene/geopolymer composites. *Ceramics International* 41. pp. 11242–11250.
103. Sobolev, K; Gutierrez, M. F. (2014). How Nanotechnology Can Change the Concrete World. Chapter in *American Ceramic Society Bulletin*.
104. Vollath, D. *Nanoparticles – Nanocomposites – Nanomaterials: An Introduction for Beginners*. WILEY-VCH. 2013.
105. Brandão, D., Borges, P.H.R., Ludvig, P., Colão, M. (2023). Geopolymers based on Metakaolin reinforced with Carbon Nanotubes. *Research Square*.
106. Hassaan, M. M; Khater, H. M; H; El-Mahllawy, M. S; Nagar, A. M. (2015). Production of geopolymer composites enhanced by nano-kaolin material. *Journal of Advanced Ceramics* 4(4). pp. 245-252.
107. Lu, S-N., Xie, N., Feng, L-C., Zhong, J. (2015). Applications of Nanostructured Carbon Materials in Constructions: The State of the Art. *Journal of Nanomaterials*.
108. Khater, H. M. (2016). Effect of nano-silica on microstructure formation of low-cost geopolymer binder, *Nanocomposites*, 2:2, pp. 84-97.
109. Khater, H.M., Abd el Gawaad, H.A. (2016). Characterization of alkali activated geopolymer mortar doped with MWCNT. *Construction and Building Materials* 102. 329–337.
110. Davoodabadi, M., Vareli, I., Liebscher, M., Tzounis, L., Sgarzi, M., Paipetis, A.S., Yang, J., Cuniberti, G., Mechtcherine, V. (2021). Thermoelectric Energy Harvesting from Single-Walled Carbon Nanotube

- Alkali-Activated Nanocomposites Produced from Industrial Waste Materials. *Nanomaterials* 2021, 11, 1095.
111. Cao, V. D; Pilehvar, S; Salas-Bringas, C; Szczotok, A. M; Bui, T. Q; Carmona, M; Rodriguez, J. F; Kjøniksen, A-L. (2018). Thermal performance and numerical simulation of geopolymer concrete containing different types of thermoregulating materials for passive building applications. *Energy & Buildings*. n. 173. pp. 678–688.
 112. Foldari, G; Invernizzi, N. (2012). Implicações sociais e ambientais do desenvolvimento das nanotecnologias na América Latina e no Caribe. ReLANS.
 113. Chen, J., Akono, A-T. (2021). Influence of multi-walled carbon nanotubes on the fracture response and phase distribution of metakaolin-based potassium geopolymers. *J Mater Sci* 56. 19403–19424.
 114. Rocha, V.V., Ludvig, P., Trindade, A.C.C., Silva, F.A. (2019). The influence of carbon nanotubes on the fracture energy, flexural and tensile behavior of cement-based composites. *Construction and Building Materials* 209.
 115. Akono, A-T. (2020). Fracture Behavior of Metakaolin-based Geopolymer Reinforced with Carbon Nanofibers. *Journal of Ceramic Engineering and Science* June 26, 2020
 116. Abdalla, J.A., Thomas, B.S., Hawileh, R.A., Yang, J., Jindal, B.B., Ariyachandra, E. (2022). Influence of nano-TiO₂, nano-Fe₂O₃, nanoclay and nano-CaCO₃ on the properties of cement/geopolymer concrete. *Cleaner Materials* 4.
 117. Novais, R. M; Buruberri, L. H; Seabra, M. P; Labrincha, J. A. (2016). Novel porous fly-ash containing geopolymer monoliths for lead adsorption from wastewaters. *J. Hazard Mater.* 318, pp. 631-640.
 118. Shekhovtsova, J., Kearsley, E. P., Kovtun, M. (2015). Evaluation of short- and longterm properties of heat-cured alkali-activated fly ash concrete. *Magazine of Concrete Research*, 67(16), 897–905.
 119. Ravitheja, A., Kumar, N.L.N.K. (2019). A study on the effect of nano clay and GGBS on the strength Properties of fly ash based geopolymers. *Materials Today: Proceedings* 19. 273–276.
 120. Liu, X., Nair, S.D., Aughenbaugh, K.L., Juenger, M.C.G., Oort, E. (2020). Improving the rheological properties of alkali-activated geopolymers using non-aqueous fluids for well cementing and lost circulation control purposes. *Journal of Petroleum Science and Engineering*, 195.
 121. Tinoco, M.P., Silva, F.A. (2021). On the mechanical behavior of hybrid fiber reinforced strain hardening cementitious composites subjected to monotonic and cyclic loading. *Journal of Materials Research and Technology* 11. 754-768.
 122. Stolz, J; Boluk, Y; Bindiganavile, V. (2018). Mechanical, thermal and acoustic properties of cellular alkali activated fly ash concrete. *Cement and Concrete Composites*. n. 94. pp. 24–32. 2018.
 123. Cao, V. D; Pilehvar, S; Salas-Bringas, C; Szczotok, A. M; Rodriguez, J. F; Carmona, M; Al-Manasir, N; Kjøniksen, A-L. (2017). Microencapsulated phase change materials for enhancing the thermal performance of Portland

- cement concrete and geopolymer concrete for passive building applications. *Energy Conversion and Management*. n. 133. pp. 56–66.
124. Keane, P.F., Foltz, J.S., Chadha, V., Marsh, C.P., Kriven, W.M. (2021). Amorphous self-healed, chopped basalt fiber-reinforced, geopolymer composites. *J Am Ceram Soc*. 202; 104:3443–3451.
 125. Gülsan, M. E; Alzebaree, R; Rasheed, A. A; Nis, A; Kurtoglu, A.E. (2019). Development of fly ash/slag based self-compacting geopolymer concrete using nano-silica and steel fiber. *Construction and Building Materials*, 211, 271-283.
 126. Syamsidar, D; Nurfadilla; Subaer. (2017). The Properties of Nano TiO₂-Geopolymer Composite as a Material for Functional Surface Application. *MATEC Web of Conferences* 97.
 127. Wardani, N. K; Maulana, A. I; Nurfadilla; Subaer. (2017). Development of Nano TiO₂-Geopolymer Functional Composite as Antifouling Bricks. *MATEC Web of Conferences* 97.
 128. Joshi, A., Montes, C., Salehi, S., Allouche, E., Lvov, Y. (2015). Optimization of Geopolymer Properties by Coating of Fly-Ash Microparticles with Nanoclays. *J Inorg Organomet Polym* 25. 282–292.

3. Potassium-waterglass (K-WG) Influence on Geopolymer Strength Development & Leaching in Different Curing Environments

3.1. Introduction

A geopolymer material can be defined as an inorganic, amorphous, polymeric, 3D structure consisting of alumina, silica, and alkali metal oxides [1], synthesized from the mixture of a powdered aluminosilicate source with a solution based on amorphous silica dissolved in highly alkaline [1, 2, 3] or highly acidic [4] solution. The chemical composition of geopolymers is somewhat similar to that of zeolites and can be semi-crystalline depending on the geopolymerization conditions [5]. In principle, any material containing amorphous Si and Al can be used to produce alkaline materials. Pure Si and Al-based materials, such as kaolin, from mineral origin, and fly ash, an industrial waste, are effectively used to produce geopolymers. Highly Ca-based products, such as mining wastes, metallurgical slag and others industrial by-products [5, 6] are the baseline for manufacturing alkali-activated materials. From this variety of aluminosilicates sources, several products can be obtained, which consequently leads to a wide range of applications, mechanical capacities, and strength evolution over time [5, 7, 8].

Metakaolin, a commercial product, is one of the main sources of aluminosilicate used, which is obtained by calcining kaolinitic clay at around 750°C for 6 hours [9]. The meta stable state of collapsing clay is as reactive as pozzolan. However, unlike pozzolanic cements and alkali-activated materials, geopolymers do not form hydrated calcium silicates, but occurs the polycondensation of silica and alumina [5, 10]. One of the main advantages of geopolymers is that the maximum strength can be obtained in 1-3 days, depending on the curing regime, compared to 14-28 days for ordinary Portland cement and alkali activated materials [4]. The geopolymerization process does not follow mechanisms of pozzolanic activity and hydration [11], but instead a multi-step reaction process (which can

occur simultaneously): (1) Dissolution of aluminosilicates; (2) Polycondensation, due to reorganization of precursor ions; (3) Polymerization (precipitation at room temperature) [5, 7].

Geopolymers are intrinsically refractory, formed by tetrahedral units of $(\text{AlO}_4)^-$ and SiO_4 that share all of their vertices, forming Si-O-Si or Si-O-Al bonds that give rise to a rigid solid, containing group I cations for charge balance [4, 12]. The alkali solution, commonly known as “waterglass”, usually corresponds to 1 mol of NaOH or KOH (or even a combination of both) dissolved into 10 mol or more of H_2O , to which usually 2 or more mol of amorphous SiO_2 is added [1]. The mixture of the aluminosilicate source with a properly designed waterglass might control the rate of strength development of the geopolymer as it promotes the hydrolysis of siliceous and aluminum species and can also compensate for the lack of silicate in the precursor [5].

The chemical nature of the alkali influences the evolution of the geopolymer microstructure, affecting the mechanical behavior at different ages. Na^+ ions induce a higher reaction rate compared to K^+ ions due to the smaller atomic radius, which allows greater mobility and reactivity at low temperatures [2]. The faster geopolymerization capacity of sodium cations compared to potassium is also due to the higher charge density [13]. However, Na-based waterglasses are frequently more viscous than their K-based counterparts. Although Na-based waterglasses lead to a polymerization process at a faster pace, it is known that the work required to mix a more viscous paste may not ensure complete homogenization and greater degassing, leading to a less densified and workable paste [13, 14]. Thus, different natures and concentrations of waterglass will have different effects on the geopolymerization process, along with the composition (compound ratios and formulations) and granulometry of the precursor, added to varied synthesis conditions (temperature, pressure, and humidity) [7, 13, 14].

Due to this complexity, some researchers resorted to statistical models to evaluate the factors that lead to optimized mechanical properties, such as compressive strength and ductility [15-19]. It was found that the chemical composition of the waterglass is the most important parameter for obtaining geopolymers with maximum compressive strength [17]. The $\text{H}_2\text{O}/\text{K}_2\text{O}$ molar ratio commonly controls the fluidity of fresh geopolymer pastes [9]. In addition, excess of water can result in greater microstructural porosity [1, 20]. The $\text{K}_2\text{O}/\text{Al}_2\text{O}_3$ molar

ratio mainly determines the degree of polymerization, with the geopolymerization process being more governed by the molarity of the hydroxide solution than by the reaction time [9]. The $\text{SiO}_2/\text{Al}_2\text{O}_3$ ratio is directly related to the development of compressive strength [9, 14], which generally increases with the value of this ratio [13, 20]. However, geopolymers with higher Si:Al ratios may be more prone to drying shrinkage due to more intense capillary deformations related to water evaporation compared to those with low Si:Al ratios, characterized by larger pores [21]. Thus, although the compressive strength is expected to increase with the Si:Al ratio due to greater strengths of Si-O-Si bonds when compared to Si-O-Al bonds and higher sample densities, the size and distribution of defects, such as cracks and micro and macro voids, will also be influencing factors [14].

Previous works have quantified the degree of geopolymerization through the rate of heat release obtained by isothermal calorimetry [7, 9, 22]. The method was also proposed to characterize the reactivity of commercial metakaolins aimed at the synthesis of geopolymers by expressing the time needed to reach the exothermic peak and its temperature [11]. References that used this technique showed that Na-based waterglasses were about three times more reactive than K-based waterglasses over a period of 7 days. However, similar strength values were found at 28 days for both variations [2].

A major obstacle in implementing the geopolymer technology in similar applications to that of concrete is their tendency to leach alkalis when cured in water [23], resulting in efflorescence issues [24]. There are two known controlling mechanisms of leaching in geopolymers: (i) diffusion, in which there is a concentration gradient between the pore solution and the external surface; and (ii) solubility control, considering also the concentration gradient. However, in the last case, new phases must be formed on the surface (with lower solubility than the original products) or the concentration on the external surface must be in the same order of magnitude as the concentration of the pore solution [25].

Potassium-based geopolymers can be a more adequate substitute material for cementing applications due to their greater flowability, thermal stability and lower tendency to leach [26, 27] when compared to similar sodium variations. Still, so far, not many papers have addressed their use in similar conditions. Kamali *et al.* [28] developed geopolymer formulations using K-waterglass. However, the material did not present any significant strength within two days of saturated curing.

The same was reported by Singh and Subramaniam [20] for geopolymers based on low-calcium fly ash synthesized with Na-WG, which did not harden for up to 24 h at 25°C. Early strength is a crucial parameter when considering oil well cementing applications. The up-to-date standards require very short initial setting and wait-on cement (WOC) times to support the casing [29]. Therefore, improving the reaction kinetics of potassium-based geopolymers becomes fundamental when aimed at these types of applications. Still, evaluations restricted to heat release parameters are not sufficient to provide a general evaluation of the material's reaction degree since other phenomena may be involved in saturated curing conditions. The geopolymer strength, for example, must be evaluated in both dry and saturated curing regimes, as well as the alkali leaching effects during their fresh-to-hard transient stages.

For these reasons, the aim of this research was to evaluate the reaction mechanisms of metakaolin-based geopolymers in the initial curing stages by comparing the use of four potassium waterglass formulations by means of isothermal calorimetry analysis. An ultrasonic cement analyzer was used to correlate the calorimetric characterization with the evolution of compressive strength. Destructive compressive strength tests and pH measurements were carried out to measure the geopolymers strength evolution over time and leaching effects when subjected to different curing media (dry and saturated), providing some insight on their applicability in varied atmospheric conditions.

3.2. Experimental Program

3.2.1. Materials and geopolymer design

To investigate the relationship between the waterglass $\text{H}_2\text{O}/\text{K}_2\text{O}$ and $\text{SiO}_2/\text{K}_2\text{O}$ molar ratios and the reaction kinetics at early ages of a metakaolin-based geopolymer, four distinct K-waterglass compositions were considered: One to lead to the stoichiometric formulation of the geopolymer ($\text{K}_2\text{O}\cdot\text{Al}_2\text{O}_3\cdot 4 \text{SiO}_2\cdot 11 \text{H}_2\text{O}$) [1], thus being equal to $2 \text{KOH} + 2 \text{SiO}_2 + 10 \text{H}_2\text{O}$; two others reducing the amount of water in the alkaline solution to 9 and 8, to increase the alkalinity and; a fourth formulation with the same amount of water as the stoichiometric solution but with higher KOH content, corresponding to $2 \text{KOH} + 2 \text{SiO}_2 + 10 \text{H}_2\text{O}$ and used by

Zhao *et al.* [30]. This last formulation was also chosen to increase alkalinity, as it favors dissolution and polycondensation [5, 7], at the same time that it does not influence rheology since the amount of water is around 5 % lower compared to the stoichiometric condition. All compositions are specified in Table 3.1.

Table 3.1 - Composition for formulating 1000 g of waterglass and quantity of resulting products: detailed breakdown by weight of components.

	Reagents (g)			Waterglass (g)		
	KOH	H ₂ O	SiO ₂	K ₂ O	H ₂ O	SiO ₂
WG1	272.07	436.47	291.46	228.42	480.12	291.46
WG2	284.48	410.75	304.77	238.84	456.39	304.77
WG3	298.09	382.57	319.34	250.27	430.39	319.34
WG4	327.00	403.53	269.47	274.54	455.99	269.47

Initially, the waterglass was prepared as follows: (1) Dissolution of potassium hydroxide (PROQUÍMIOS, 88.9% purity, in the form of lentils) in deionized water; (2) Gradual addition of hydrophilic silica fume (AEROSIL – Evonik); (3) Mixing in a magnetic mixer for at least 24 h. After the mixing time, the waterglass was left to rest for at least 24 hours before use, ensuring thermal equilibrium within the environment.

The geopolymer formulations made in this study were prepared using a highly reactive metakaolin (MetaMax – BASF), as the only source of aluminosilicate. The composition of all geopolymers was fixed at a molar ratio of SiO₂/Al₂O₃=4, as this value leads to better mechanical properties [14, 30, 31]. The metakaolin powder was analyzed by X-ray fluorescence (XRF) and the results are shown in Table 3.2, presenting the material's chemical composition.

Table 3.2 - Composition (% wt.) of metakaolin MetaMax from BASF determined by XRF.

Al ₂ O ₃	SiO ₂	TiO ₂	Fe ₂ O ₃	K ₂ O	SO ₃	CaO	Others
50.02	48.28	1.11	0.355	0.109	0.055	0.026	0.045

Considering the chemical compositions of the different waterglasses proposed and the ones measured for the metakaolin (assuming that 100% of the Si and Al content in the metakaolin is reactive and contributes to the formation of the geopolymer), the design of each mixture was calculated, as shown in Table 3.3.

Table 3.3 - Geopolymer design: detailed breakdown by weight of components.

Nomenclature	Waterglass type	Composition (g)	
		Metakaolin	Waterglass
GP1	WG1	1000.00	1890.00
GP2	WG2	1000.00	1830.00
GP3	WG3	1000.00	1750.00
GP4	WG4	1000.00	1860.00

Metakaolin and waterglass were mixed in these proportions, and the mixing process consisted of the following steps: (1) Mixing the components in an IKA 60 control mixer at 1500 rpm for at least 10 minutes to ensure homogeneity and maximum reactivity; and (2) Submitting the formed paste to vibration at a frequency of 3 Hz and a minimum time of 10 minutes to remove air bubbles.

For uniaxial compressive strength tests, cubic samples (50.8 mm side) were molded in metallic boxes at room temperature (21°C) and cured under two conditions: completely immersed in water (water curing) and at dry conditions, the molds being wrapped with transparent acetate sheet, following the recommendations shown in previous studies [30, 32-36], to prevent early dehydration and cracking.

After 1 day, all specimens were demolded, and three specimens of each curing condition were tested. Other three specimens were stored in deionized water (water cured) to be tested after 3 days, and other 6 specimens, dry cured, were stored in a sealed box to be tested in 3 days and 28 days (reference values).

3.2.2. Testing Methods

3.2.2.1. Calorimetry

Isothermal calorimetry was used to estimate the setting time and the degree

of geopolymerization of each of the geopolymer formulations. The heat of geopolymerization and heating rate were monitored by a Calmetrix model I-Cal HPC calorimeter over a period of 7 days at intervals of 1 minute. In order for the samples to be comparable, it was necessary to use the same paste weight for each composition, choosing the value of 50 g.

The initial setting time considered was the time at half the amplitude of the polycondensation peak, with the final setting time corresponding to the peak value [36].

To evaluate the reaction kinetics at early ages, the JMAK model [9] was used with the following equation:

$$\ln(-\ln(1-\alpha)) = n \cdot \ln(t) + \ln(k) \quad (3.1)$$

Where: α = degree of reaction (equal to the ratio of heat released within a specified time scale to total accumulated heat release); n – Avrami exponent (related to the reaction mechanism during setting and hardening); t – reaction time scale (in minutes); k – Avrami growth rate (reflects nucleation and growth characteristics).

3.2.2.2. Non-destructive compressive strength evolution

The ultrasonic cement analyzer (UCA) technique was used to monitor the evolution of the compressive strength of different geopolymer compositions. Along with the calorimetry results, this dataset is expected to identify differences in reaction kinetics and estimate the final mechanical properties.

The freshly prepared geopolymer was transferred to the equipment (Chandler, model 4265) and the data were collected for 7 days every 30 seconds under room conditions (21°C). However, the equipment is calibrated for testing Portland cement pastes; therefore, for other materials, the equations for calculating compressive strength must be adjusted and a new algorithm must be provided and applied. This is because the density and ultrasonic pulse velocity of the geopolymer are lower than those of Portland cement paste of similar compressive strength. The pulse velocity mainly depends on the density and properties of the paste [37, 38]. For this reason, a fit relation developed by Kamali *et al.* [28] was used to fit the ultrasonic strength data obtained for K-geopolymers, according to Equation 3.2:

$$y = 28.662x^2 - 1310.9x + 12057 \quad (3.2)$$

Where: y – ultrasonic compressive strength; x – pulse transit time.

3.2.2.3 pH measurement

The leaching behavior of geopolymers was estimated from pH measurements. For this, particle-powder samples were prepared by grinding geopolymer samples cured in dry and saturated conditions. Two grams of powder were dissolved in 20 ml of deionized water (1:10 concentration). For 3 consecutive days, the solution was mixed to ensure homogeneity). For 3 consecutive days, the solution was mixed to ensure homogeneity.

Aliquots were also collected from 250 cm³ of water, initially deionized, in which cubic samples (side 50.8 mm) were immersed to evaluate the pH of the curing medium. At 1 and 3 days an aliquot of 20 ml of water were collected. The alkali concentration was measured by a pH meter. The reading was taken after 5 minutes. The validity of the reading value was confirmed if there was no pH variation larger than 0.25 within 3 minutes of measuring.

3.2.2.4 Uniaxial compressive strength

To evaluate the effect of leaching on the compressive strength, cubic samples (50.8 mm side) cured in dry and saturated conditions were tested at room temperature (21°C). The samples were tested after 1 and 3 days of curing. Also, samples kept in sealed compartments (21°C) for 28 days were also tested for a reference value. The geopolymers tested in the uniaxial compression tests are shown schematically in Table 3.4.

The tests were carried out on the MTS 810/500 (250 kN load cell), at a displacement rate of 0.5 mm/min. The samples were paper sanded prior to testing to obtain smooth surfaces, and thus ensure that they were subjected only to uniaxial loading.

Table 3.4 - Geopolymers tested in uniaxial compression tests as a function of time and curing medium.

	Curing days		
	1	3	28
GP1	-	-	
GP2	-	-	
GP3	-	-	
GP4			

■ Dry-cured ■ Saturated cured

3.3 Results and discussions

3.3.1 Chemical properties

The results obtained by calorimetry for all geopolymers formulations are shown in Figure 3.1.

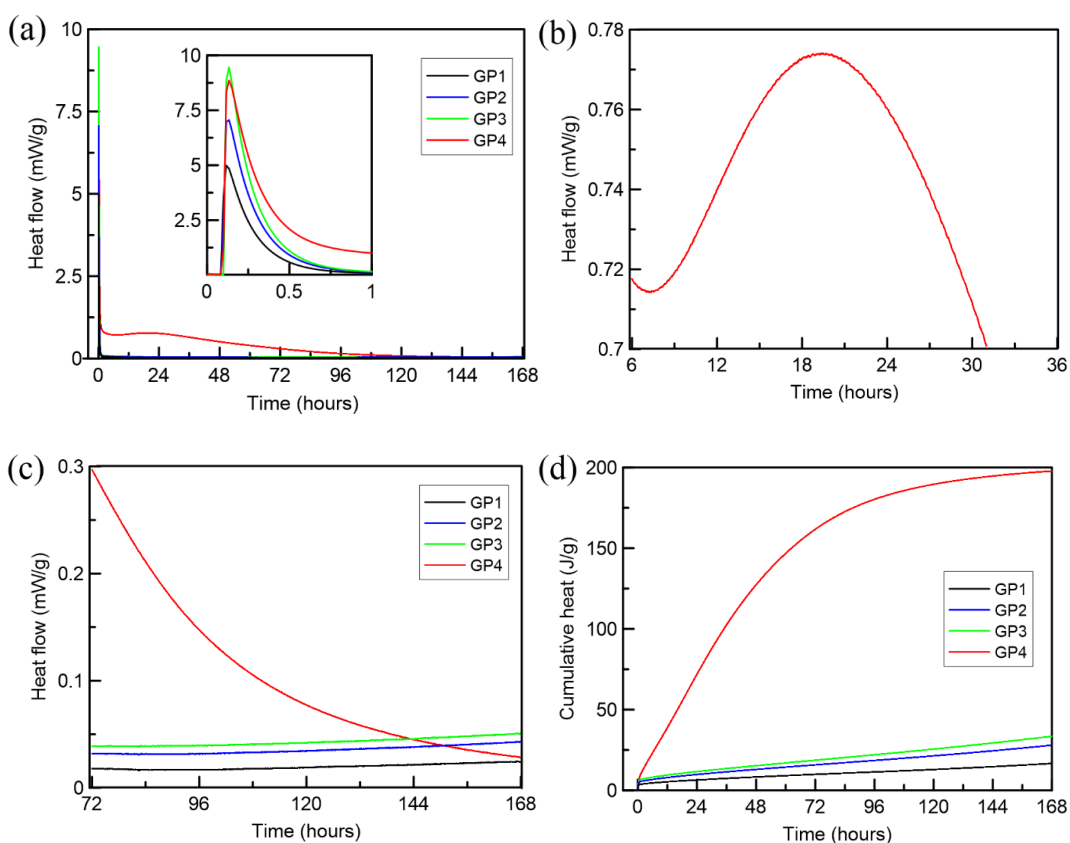


Figure 3.1 - (a) Heat flow of different geopolymer compositions as a function of curing time; (b) GP4 polycondensation peak; (c) Heat flux between 3 and 7 days of curing; (d) Cumulative heat for all geopolymers design.

As shown in Figure 3.1(a), all samples have a peak after mixing, which corresponds to the heat generated by wetting and dissolution of the aluminosilicate precursor [9, 11, 22, 36, 39]. The dissolution is generated by the immediate absorption of the alkali solution on the surface of the metakaolin and the rupture of the Si-O and Al-O bonds attacked by OH^- [22, 36, 40] forming poly-sialate oligomers (-Si-O-Al-O-) [39, 40].

The zoomed image in Figure 3.1(a) plotted for the first 1 hour of curing shows the dissolution peaks for all geopolymer formulation. As can be seen, higher concentrations of hydroxide promoted greater dissolution of aluminosilicates (due to the greater magnitude of the first peak). This explanation, however, fails when GP3 and GP4 are compared. Formulations containing high concentrations of KOH may hinder dissolution due to the faster formation of gel deposited on unreacted metakaolin particles, and therefore, less heat is released by the system [22].

Again, considering Figure 3.1(a), it is possible to see that there is a second exothermic peak, in this case only for GP4. The onset of the second exothermic peak is due to the formation and polymerization of gels [9, 11, 22, 36, 40]. During this period, the silicate and aluminate monomers formed in the dissolution period begin to polymerize into aluminosilicate oligomers and produce geopolymer seeds, which are critical for the strength development of geopolymers [22, 36, 41]. At this stage, the polymerization-condensation reactions rearrange the structure to form a three-dimensional network of poly-sialate-siloxo (-Si-O-Al-O-Si-O-) [11, 39, 40].

The development of this peak is expected in the early ages for geopolymers synthesized with K-WG with a higher hydroxide concentration, as it favors the conversion of precursors more strongly and, in this way, the desirable concentration of silicate and aluminate monomers for the polycondensation reaction is reached faster [22, 40]. The high concentration of K_2O in the GP4 system accelerated the geopolymerization, overcoming the effect of the liquid/binder ratio [36].

For clarity, the GP4 polycondensation peak was plotted over a shorter time interval, as shown in Figure 3.1(b). From this figure, the setting time, at 21°C , can be estimated at 12 h 30 min for the initial setting time and 19 h 30 min for the final setting time.

Nevertheless, with increasing alkali concentration, the dissolution and polycondensation stages can occur simultaneously, and thus the peaks are combined [22]. This could have happened with GP3, and for this reason, the graph in

Figure 3.1(c) showing the heat flux between 3 and 7 days of curing was plotted. As can be seen, the beginning of the polycondensation peak for GP1, GP2 and GP3 occurs at around 120 h. So, it can be concluded that these geopolymer formulations were still in their fresh state for up to 7 days at 21°C. It is also possible to observe in Figure 3.1(c) that GP4 is in the hardening process at the same time.

According to previous works [11, 22, 36, 39, 40], there may be a third peak in the geopolymer system related to crystallization and stabilization of the microstructure. In the case of K-geopolymer based on metakaolin, the polycondensation peak can be absorbed by this peak [11].

Another way to compare the reactivity of geopolymer systems is through the values of accumulated heat (Figure 3.1(d)). A low H₂O/K₂O ratio was beneficial for the dissolution of soluble species and formation of reaction products. However, the high concentration of K₂O in the GP4 formulation promoted faster dissolution and formed more products since the accumulated heat was 200 J/g at 7 days, when compared to values between 10 and 30 J/g for GP1-GP3.

To evaluate the geopolymerization kinetics, a linear adjustment of $\ln(-\ln(1-\alpha))$ vs $\ln(t)$ was performed, as predicted by the JMAK model [9]. The results for each geopolymer formulation are shown in Figure 3.2.

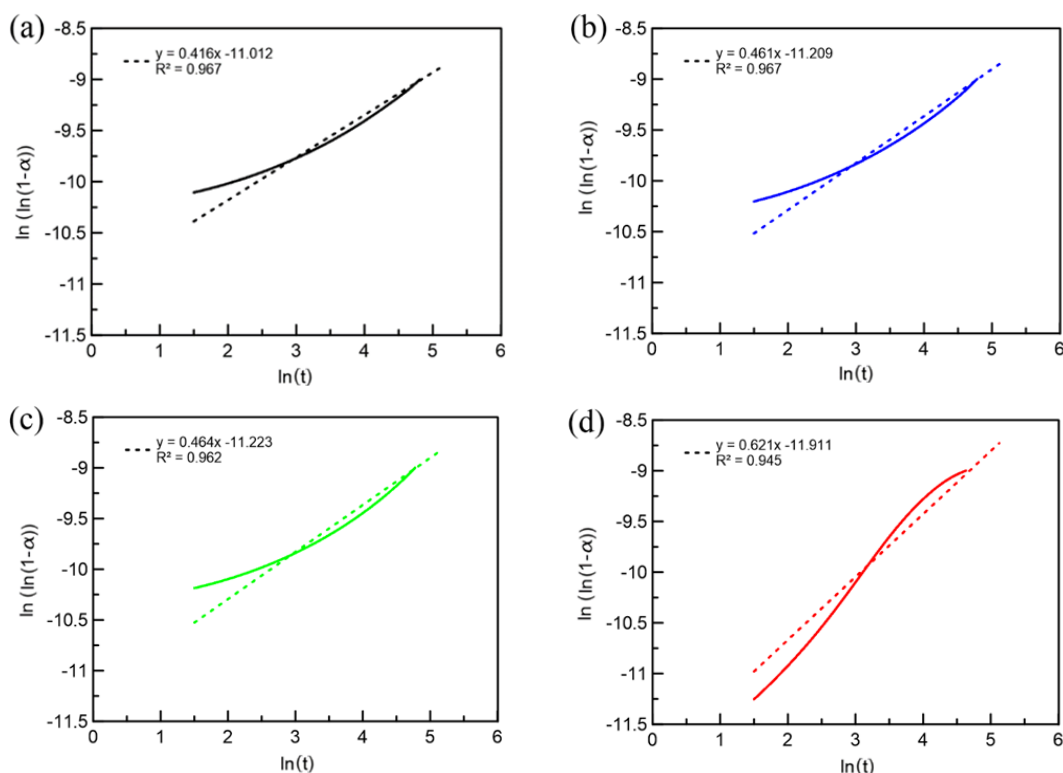


Figure 3.2 - Adjustment by JMAK model for (a) GP1; (b) GP2; (c) GP3; (d) GP4.

Fitting to the JMAK model showed an excellent correlation ($R^2 > 0.95$) for all geopolymer formulations. From the adjustment obtained, the Avrami parameters could be calculated (Table 3.5).

Table 3.5 - Avrami's parameters for all geopolymers design.

	GP1	GP2	GP3	GP4
n	0.417	0.461	0.464	0.621
k (h⁻¹)	1.650 x 10 ⁻⁵	1.355 x 10 ⁻⁵	1.336 x 10 ⁻⁵	6.716 x 10 ⁻⁶

The geopolymerization process for all variations analyzed supports the one-dimensional diffusion-controlled reaction because the Avrami exponents (n) were less than 1. The variation of n values indicates that the mobility of soluble species can be impeded by previously formed nuclei, affecting the radial growth rate of nuclei [9]. The Avrami exponent decreased with increasing H₂O/K₂O, which can be attributed to the difference in the number of soluble species dissolved in waterglass. The variation in the first exothermic peak supports this phenomenon well.

Avrami growth rate (k) is a parameter associated with nucleation and growth rates during reaction processes [9]. Geopolymers prepared with high values of H₂O/K₂O showed greater Avrami growth rates, which may have two explanations: either the sites available for nucleation are insufficient due to an excess amount of OH⁻ ions when compared to the abundant soluble species in the solution with high alkalinity, which is not conducive to rapid growth rates of reaction products; or the highly alkali solution promotes a high dissolution of the soluble species of the precursor, and this would increase the viscosity and reduce the mobility of the soluble species. The degree of full geopolymerization is obtained in a highly alkali solution, although this has an adverse effect on the individual growth rate [9].

Another chemical characteristic analyzed in the geopolymer variations was the feasibility of alkali leaching at saturated curing. The pH values of the geopolymers considering the curing medium (dry or saturated) are shown in Table 3.6:

Table 3.6 - pH values for different unary geopolymers considering the two curing conditions (dry and saturated).

	Curing medium	pH	Variation (%)
GP1	Dry (54 % RH)	10.24	13.57
	Saturated (100% RH)	8.85	
GP2	Dry (54 % RH)	9.80	-0.31
	Saturated (100% RH)	9.83	
GP3	Dry (54 % RH)	8.95	-0.11
	Saturated (100% RH)	8.96	
GP4	Dry (54 % RH)	9.30	-11.40
	Saturated (100% RH)	10.36	

The formulations that showed significant differences in pH value depending on the curing medium were GP1 and GP4. For GP1 the reason is clear: as there is more water in its formulation, the solid molecules are more separated, and thus the chance of alkalis escaping into the curing medium (in this case, into the water) is more likely, and a lower degree of geopolymerization results in more free alkalis in the pore solution [42]; for GP4, the pH after saturated curing was higher than dry curing, which at first glance may seem contradictory, but it is consistent with the fact that saturated curing delays the geopolymerization process (as can be seen in Figure 3.6(b)) and thus more free alkalis remain in the geopolymer. The pH values for the dry-cured geopolymers are consistent with the K_2O concentration in each formulation (Table 3.3), since the higher the K_2O concentration, the lower the pH value, which means that the stronger the bonding of the alkali in the geopolymer structure (further demonstrated by the compressive strength results, Figure 3.6(a)).

Furthermore, differences in stoichiometry may affect the stability of the resulting geopolymer and lead to different leaching characteristics [24, 25, 42]. Another factor is that pH measurements are not only related to the amount of alkali, but to other ions present. Therefore, such measurements are more qualitatively accurate to compare the effects of different curing mediums on the same geopolymer formulation. For GP2 and GP3, the small difference in pH values between the curing medium indicates that the controlling mechanism of leaching is diffusion [25]. Another important analysis was the measurement of the pH of the water in which the geopolymer was immersed during curing. This analysis was

performed for GP4, and the results are shown in Table 3.7.

Table 3.7 - pH values of the curing water at 1 and 3 days, after GP4 curing stages.

Solution	pH	Variation (%)
Deionized water (reference)	6.66	-
Water after 1 day of curing	7.78	16.82
Water after 3 days of curing	12.33	85.14

As shown, the pH value of the water increased during the geopolymer curing. Also considering the data presented in Table 3.6, it can be said that in addition to leaching, there is surface washing and solubilization [25, 42]. These pH values are therefore a result of the reaction degree of the geopolymer.

3.3.2. Transient state properties

Figure 3.3 shows the results of compressive strength development (obtained from ultrasonic pulse measurements) for all geopolymer formulations:

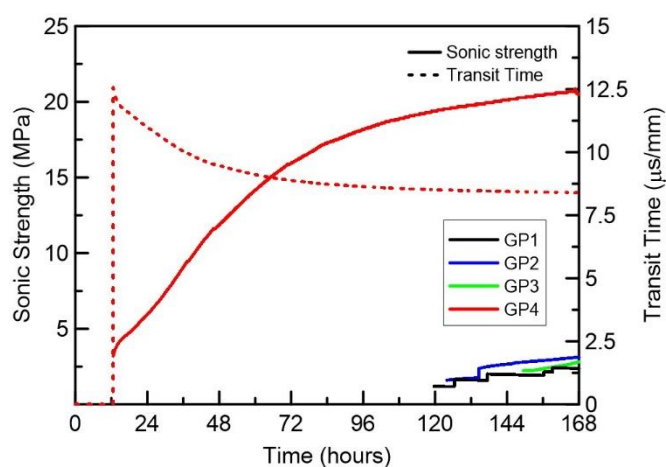


Figure 3.3 - Evolution of the compressive strength for all geopolymer formulations obtained from ultrasonic pulse measurements.

Evidently, the GP4 made it possible to achieve the shortest initial setting time, approximately 13 hours, which is compatible with the value calculated from the previous calorimetry data. The other formulations presented an initial setting time only after 120 h. With the increase in H_2O/K_2O , these formulations (GP1 to GP3) had their setting times increased, consistent with previous reports in the

literature [36]. Reduced water/solid ratios can make it difficult to mix homogeneously, which may reduce the rate of geopolymerization [22] and thus slow the setting [39]. The greatest initial strength gain for the GP4 is directly related to the increase in the alkalinity of the waterglass. As compared to the other mixes, the concentration of potassium hydroxide was 30% higher, thus increasing the degree of geopolymerization and, consequently, leading to higher compressive strength values for the same curing age.

As the geopolymerization process produces heat [1] and leads to increased strength, it is reasonable to assume a certain correlation between heat, degree of geopolymerization, and strength [7]. Figure 3.4 shows the relationship between sonic strength and accumulated heat release (obtained by calorimetry) for GP4.

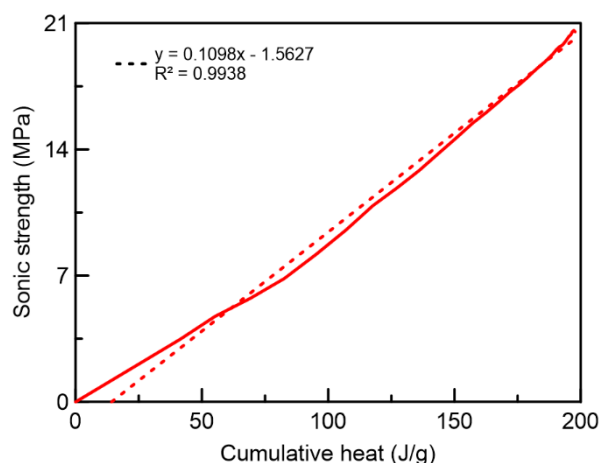


Figure 3.4 - Relationship between sonic strength and accumulated heat released for GP4.

A linear correlation between heat and sonic strength was found, consistent with results reported in the literature [7, 40]. Figure 3.4 shows that the more total heat generated, the greater the compressive strength obtained [36] and the excellent fit found ($R^2=0.99$) may be related to the high purity of metakaolin used in the present work. One of the main difficulties in using the ultrasonic cement analyzer is that this equipment is calibrated for cement pastes. Thus, the results generated for the geopolymer are only qualitative, used to suggest the setting and strength gain over time, and should not be used quantitatively to assign compressive strength values. However, a published work provided an adjustment for geopolymer pastes [28], based on transit time values. Therefore, a similar adjustment is proposed here

and shown in Figure 3.5, presenting the new sonic strength curve for GP4.

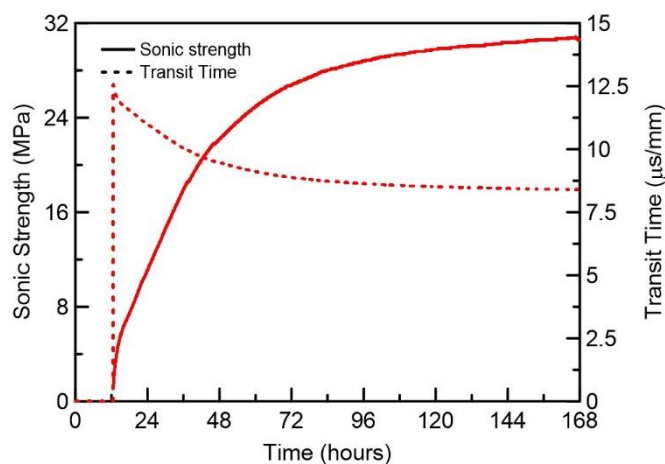


Figure 3.5 - Sonic strength data for GP4 adjusted, based on Kamali *et al.* [28].

As demonstrated in Figure 3.5, the pulse velocity increases with curing time as the transit time is reduced [37], and this is associated with the transition from the gel state to the hardened state. Over time, the transit time reduces due to the geopolymer strength gain. Corrected sonic strength values are shown in Figure 3.5. However, these values must be compared with measurements of compressive strength obtained by destructive tests to verify the adequacy of the adjustment made in Kamali *et al.* [28] with the geopolymer formulation of the present work. Furthermore, the development of geopolymer strength is complex, as it is not only a function of the degree of reaction but also how many aluminosilicate units are deposited and interconnected [7].

3.3.3. Hardened properties

The compressive strength values obtained from the destructive tests conducted for all formulations are shown in Figure 3.6. Compressive strength at 28 days (Figure 3.6(a)) increased with increasing K_2O concentration, as dissolution was favored and, consequently, enabled a greater degree of geopolymerization [19]. Furthermore, the SiO_2/K_2O molar ratio of 1.53 (corresponding to the GP4 formulation) led to maximum compressive strength, because silica and alumina were intensively dissolved, which enhanced polycondensation [45].

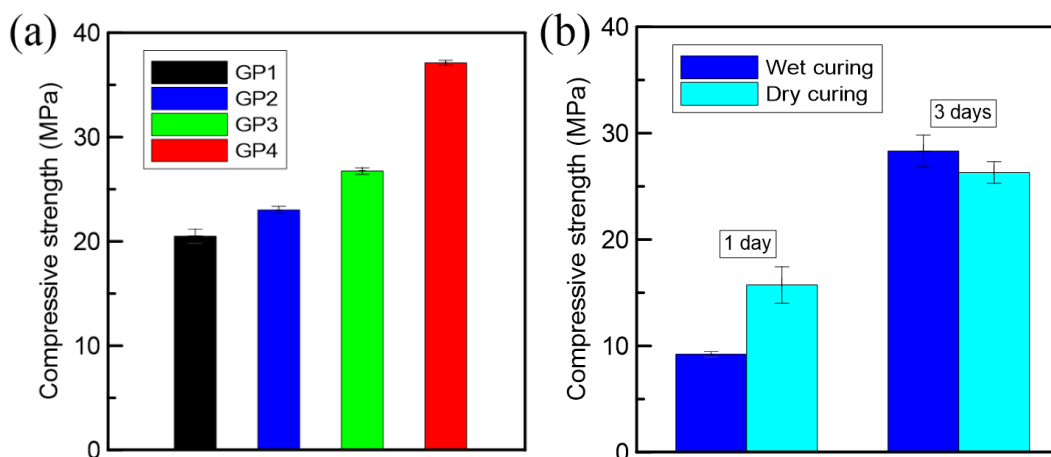


Figure 3.6 - (a) Compressive strength for all unary GP at 28 days; (b) Compressive strength of GP4 subjected to different curing mediums and time.

It is noted in Figure 3.6(a) that the compressive strength decreased significantly when the $\text{SiO}_2/\text{K}_2\text{O}$ molar ratio was increased from 1.53 to 2 (formulations GP1 to GP3); likewise, the compressive strength reduces with an increase in the $\text{H}_2\text{O}/\text{K}_2\text{O}$ ratio, given the same $\text{SiO}_2/\text{K}_2\text{O}$ ratio (GP1 to GP3), which can be related to the reduction in alkalinity.

As can be seen in Figure 3.6(b), the compressive strength of GP4 at saturated curing was about 70% lower when compared to dry curing at 1 day. In this case, a possible explanation is that the degree of geopolymerization for the dry-cured sample was higher compared to the saturated curing due to the faster removal of free water from the waterglass, increasing the alkalinity of the paste and accelerating the gelation of the aluminosilicate particles [32, 43, 44], well supported by the pH values for GP4 presented in Table 3.6. However, at 3 days of curing, no significant difference was noted in compressive strength after subjecting the GP4 samples to the two-curing mediums and it may be related to the slower evaporation of water in the saturated condition, reducing the probability for drying cracking.

Comparing the results from Figure 3.6(b) and Figure 3.5, a difference of 8.3% for the compressive strength values at 1 day and of 5.8% at 3 days can be verified. So, it can be said that the adjustment performed in the sonic strength values can be used to predict up to a small variation in the compressive strength of the GP4. Although GP3 showed a higher dissolution peak than GP4 (Figure 3.1(a)), its lower water/solids ratio may have resulted in higher amounts of unreacted MK particles, and thus the geopolymerization had a low degree [14], as revealed by

Figure 3.1(c). This is one of the key factors that supports the lower GP3 compressive strength when compared to that of GP4.

3.4. Conclusions

This investigation on the use of different K-waterglasses indicated the major influence of $\text{SiO}_2/\text{K}_2\text{O}$ and $\text{H}_2\text{O}/\text{K}_2\text{O}$ molar ratios on the geopolymerization process and strength gain at early ages. Still, for the same $\text{SiO}_2/\text{K}_2\text{O}$ molar ratio the compressive strength reduces when increasing in the $\text{H}_2\text{O}/\text{K}_2\text{O}$ molar ratio, which may be related to the reduction in alkalinity and, thus, lower polycondensation capacity.

Isothermal calorimetry effectively showed the progress of geopolymerization, with the magnitude and elapsed time of the polycondensation peak being an indicator of the setting time. The measurement of pH values showed that the formulated geopolymers, with the exception of the stoichiometric composition, have good water resistance and that the leaching process is limited by a diffusion mechanism.

At room temperature (21°C), waterglass formulations WG1 to WG3 led to the lowest dissolution of metakaolin, which resulted in a slowdown of the polycondensation reaction, which occurred in the matter of 120 h after mixing. This may be the result of insufficient alkali content available to promote faster polycondensation.

The adjustment performed in the sonic strength values led to a difference of 8.3% for the compressive strength values at 1 day and of 5.8% at 3 days, so the ultrasonic cement analyzer can be used to predict the compressive strength of the GP4. Moreover, the evolution of the total heat released was consistent with the strength monitored through an ultrasonic cement analyzer, presenting an excellent linear fit ($R^2=0.99$). Thus, polycondensation is directly related to strength gain in geopolymers based on metakaolin.

After saturated curing, the compressive strength of the geopolymer was lower than after dry curing for 1 day due to the delay in the geopolymerization reactions. However, at 3 days, the strength in both medium (water and dry) showed similar values and it may be related to the slower evaporation of water in the saturated condition, reducing the probability for drying cracking.

The study demonstrated a viable method to optimize the geopolymer design and predict strength by adjusting the molar ratios of $\text{SiO}_2/\text{K}_2\text{O}$ and $\text{H}_2\text{O}/\text{K}_2\text{O}$ in waterglass. A greater amount of alkali ions plays an important role in the formation of a geopolymer since they act in the charge balance. The K-waterglass composition with $\text{SiO}_2/\text{K}_2\text{O}=1.53$ and $\text{H}_2\text{O}/\text{K}_2\text{O}=8.69$ presented a rapid strength gain with low leachability and is therefore presented as an optimistic solution to be used in saturated conditions that may require a faster strength evolution.

3.5. References

1. W.M. Kriven, Geopolymer-Based Composites, *Comprehensive Composite Materials II*. 5 (2018) 269-280. <https://doi.org/10.1016/B978-0-12-803581-8.09995-1>.
2. J.L. Provis, Alkali-activated materials, *Cement and Concrete Research*. 114 (2018) 40-48. <https://doi.org/10.1016/j.cemconres.2017.02.009>.
3. J. Provis, S.A. Bernal, Geopolymers and related alkali-activated materials, *Annual Review of Materials Research*. 44 (2014) 299–327. <https://doi.org/10.1146/annurev-matsci-070813-113515>.
4. T. Ling, K. Wang, X. Wang, S. Hua, Effects of mix design parameters on heat of geopolymerization, set time, and compressive strength of high calcium fly ash geopolymer, *Construction and Building Materials*. 228 (2019). <https://doi.org/10.1016/j.conbuildmat.2019.116763>
5. M.D. Olawale, Syntheses, characterization and binding strength of geopolymers: A review, *International Journal of Materials Science and Applications*. 2(6) (2013) 185- 193..
6. I.M. Kamal, K. Allaf, Geopolymers: Prospects For Polymer Industry, Conference: Proceedings of the third International conference on advances and trends in engineering materials and their applications, 6-10 July (2009), Montreal-Canada. ISBN 0-9780479.
7. W. Hu, Y. Ma, M. Koehler, H. Gong, B. Huang, Mix design optimization and early strength prediction of unary and binary geopolymer from multiple waste streams. *Journal of Hazardous Materials*. 403 (2021). <https://doi.org/10.1016/j.jhazmat.2020.123632>.
8. B. Walkley, X. Ke, J.L. Provis, S.A. Bernal, Activator Anion Influences the Nanostructure of Alkali-Activated Slag Cements, *The Journal of Physical Chemistry C*. 125(37) (2021) 20727- 20739.
9. G. Liang, W. Yao, A. She, New insights into the early-age reaction kinetics of metakaolin geopolymer by ^1H low-field NMR and isothermal calorimetry. *Cement and Concrete Composites*. 137 (2023). ISSN:0958-9465.
10. B. Singh, G. Ishwarya, M. Gupta, S.K. Bhattacharyya, Geopolymer concrete: a review of some recent developments, *Construction and Building Materials*. 85 (2015) 78–90.
11. R. Davidovits, C. Pelegris, J. Davidovits, Standardized Method in Testing Commercial Metakaolins for Geopolymer Formulations, Geopolymer Institute Library. (2019). <https://doi.org/10.13140/RG.2.2.18109.10727/1>.

12. K.A. Komnitsas, Potential of geopolymer technology towards green buildings and sustainable cities, *Procedia Engineering*. 21 (2011) 1023–1032. <https://doi.org/10.1016/j.proeng.2011.11.2108>.
13. E. Papa, V. Medri, S. Amari, J. Manaud, P. Benito, A. Vaccari, E. Landi, Zeolite-geopolymer composite materials: Production and characterization, *Journal of Cleaner Production*. 171 (2018) 76–84. <https://doi.org/10.1016/j.jclepro.2017.09.270>.
14. M. Lizcano, H.S. Kim, S. Basu, M. Radovic, Mechanical properties of sodium and potassium activated metakaolin-based geopolymers, *Journal of Materials Science*. 47 (2012) 2607–2616.
15. L. Xin, X. Jinyu, B. Erlei, L. Weimin, Systematic study on the basic characteristics of alkali-activated slag-fly ash cementitious material system, *Construction and Building Materials*. 29 (2012) 482–486. <https://doi.org/10.1016/j.conbuildmat.2011.09.021>.
16. M. Zahid, N. Shafiq, M.H. Isa, L. Gil, Statistical modeling and mix design optimization of fly ash based engineered geopolymer composite using response surface methodology, *Journal of Cleaner Production*. 194 (2018) 483–498. <https://doi.org/10.1016/j.jclepro.2018.05.158>.
17. H. Mehdizadeh, E.N. Kani, Modeling the influence of chemical composition on compressive strength behavior of alkali activated phosphorus slag cement using statistical design, *Canadian Journal of Civil Engineering*. 45(3) (2018) 1073–1083. <http://dx.doi.org/10.1139/cjce-2018-0132>.
18. M.E. Gülsan, R. Alzebaree, A.A. Rasheed, A. Nis, A.E. Kurtoglu, Development of fly ash/slag based self-compacting geopolymer concrete using nano-silica and steel fiber, *Construction and Building Materials*. 211 (2019) 271–283. <https://doi.org/10.1016/j.conbuildmat.2019.03.228>.
19. M.N.S. Hadi, N.A. Farhan, M.N. Sheikh, Design of geopolymer concrete with GGBFS at ambient curing condition using Taguchi method, *Construction and Building Materials*. 140 (2017) 424–431.
20. G.V.P.B. Singh, K.V.L. Subramaniam, Influence of processing temperature on the reaction product and strength gain in alkali-activated fly ash, *Cement and Concrete Composites*. 95 (2019) 10–18.
21. C. Ferone, F. Colangelo, G. Roviello, D. Asprone, C. Menna, A. Balsamo, A. Prota, R. Cioffi, G. Manfredi, Application-Oriented Chemical Optimization of a Metakaolin Based Geopolymer, *Materials*. 6(5) (2013) 1920–1939. <https://doi.org/http://dx.doi.org/10.3390/ma6051920>.
22. Q. Zhong, X. Tian, G. Xie, X. Luo, H. Peng, Investigation of Setting Time and Microstructural and Mechanical Properties of MK/GGBFS-Blended Geopolymer Pastes, *Materials*. 15(23) (2022).
23. A. Saludung, T. Azeyanagi, Y. Ogawa, K. Kawai, Alkali leaching and mechanical performance of epoxy resin-reinforced geopolymer composite, *Materials Letters*. 304 (2021).
24. M. Łach, K. Korniejenko, J. Walter, A. Stefańska, J. Mikuła, Decreasing of Leaching and Improvement of Geopolymer Properties by Addition of Aluminum Calcium Cements and Titanium Oxide, *Materials*, 13(3):495 (2020). <https://doi.org/10.3390/ma13030495>.
25. Z. Sun, A. Vollpracht, Leaching of monolithic geopolymer mortars, *Cement and Concrete Research*. 136 (2020).
26. E.N. Kani, A. Allahverdi, J.L. Provis, Efflorescence control in geopolymer

- binders based on natural pozzolan. *Cement and Concrete Composites*. 34(1) (2012) 25-33. <https://doi.org/10.1016/j.cemconcomp.2011.07.007>.
27. H. Szklorzová, V. Bílek, Influence of alkali ions in the activator on the performance of alkali-activated mortars. In: *Proceedings of the 3rd International Symposium on Non-traditional Cement and Concrete*, Brno, Czech Republic 2008 Jun (pp. 10-12).
 28. M. Kamali, M. Khalifeh, A. Saasen, R. Godøy, L. Delabroy. Alternative setting materials for primary cementing and zonal isolation –Laboratory evaluation of rheological and mechanical Properties, *Journal of Petroleum Science and Engineering*. 201 (2021).
 29. S. Adjei, S. Elkatatny, P. Sarmah, A.M. Abdelfattah, Evaluation of calcined Saudi calcium bentonite as cement replacement in low-density oil-well cement system, *Journal of Petroleum Science and Engineering*. 205 (2021). <https://doi.org/10.1016/j.petrol.2021.108901>.
 30. J. Zhao, M. Liebscher, A. Michel, D. Junger, A.C.C. Trindade, F.A. Silva, V. Mechtcherine, Development and testing of fast curing, mineral-impregnated carbon fiber (MCF) reinforcements based on metakaolin-made geopolymers, *Cement and Concrete Composites*. 116 (2021).
 31. M. Zhang, M. Zhao, G. Zhang, D. Mann, K. Lumsden, M. Tao, Durability of red mud-fly ash based geopolymer and leaching behavior of heavy metals in sulfuric acid solutions and deionized water, *Construction and Building Materials*. 124 (2016) 373–382.
 32. M. Ahmad, K. Rashid, R. Hameed, E.U. Haq, H. Farooq, M. Ju. Physico-mechanical performance of fly ash based geopolymer brick: Influence of pressure - temperature – time, *Journal of Building Engineering*. 50 (2022). <https://doi.org/10.1016/j.jobeb.2022.104161>.
 33. S. Kajarathan, S. Karthikan, M.C.M. Nasvi, Geopolymer as Well Cement and its Mechanical Behavior with Curing Temperature. In: *Proceedings of the 6th International Conference on Structural Engineering and Construction Management 2015*, Kandy, Sri Lanka, 11–13 December.
 34. A.C.C. Trindade, F.A. Silva, H.A. Alcamandb, P.H.R. Borges, On The Mechanical Behavior of Metakaolin Based Geopolymers Under Elevated Temperatures, *Materials Research*. 20(Suppl. 2) (2017) 265-272. <https://doi.org/10.1590/1980-5373-MR-2017-0101>.
 35. T. Ai, D. Zhong, Y. Zhang, J. Zong, X. Yan, Y. Niu, The Effect of Red Mud Content on the Compressive Strength of Geopolymers under Different Curing Systems, *Buildings*. 11(7) 298 (2021).
 36. Y. Ling, K. Wang, X. Wang, S. Hua, Effects of mix design parameters on heat of geopolymerization, set time, and compressive strength of high calcium fly ash geopolymer, *Construction and Building Materials*. 228 (2019). <https://doi.org/10.1016/j.conbuildmat.2019.116763>.
 37. N.A. Farhan, M.N. Sheikh, M.N.S. Hadi, Investigation of engineering properties of normal and high strength fly ash based geopolymer and alkali-activated slag concrete compared to ordinary Portland cement concrete, *Construction and Building Materials*. 196 (2019) 26–42. <https://doi.org/10.1016/j.conbuildmat.2018.11.083>.
 38. Y. Bu, W. Song, M. Wang, Y. He, The improvement of cementation quality rating method based on compressive strength for low density cement system, *Procedia Engineering* 18 (2011) 289–294.
 39. C. Kuenzel, T.P. Neville, S. Donatello, L. Vandeperre, A.R. Boccaccini,

- C.R. Cheeseman, Influence of metakaolin characteristics on the mechanical properties of geopolymers, *Applied Clay Science*. 83–84 (2013) 308–314. <https://doi.org/10.1016/j.clay.2013.08.023>.
40. D.M. González-García, L. Téllez-Jurado, F.J. Jiménez-Álvarez, L. Zarazua-Villalobos, H. Balmori-Ramírez, Evolution of a natural pozzolan-based geopolymer alkalized in the presence of sodium or potassium silicate/hydroxide solution, *Construction and Building Materials*. 321 (2022). <https://doi.org/10.1016/j.conbuildmat.2021.126305>.
 41. N.K. Lee, H.K. Lee, Reactivity and reaction products of alkali-activated, fly ash/slag paste, *Construction and Building Materials*. 81 (2015) 303–312. <https://doi.org/10.1016/j.conbuildmat.2015.02.022>.
 42. N. Ukrainczyk, Simple Model for Alkali Leaching from Geopolymers: Effects of Raw Materials and Acetic Acid Concentration on Apparent Diffusion Coefficient, *Materials*. 14(6) (2021) 1425.
 43. J. Shekhovtsova, E.P. Kearsley, M. Kovtun, Evaluation of short- and long-term properties of heat-cured alkali-activated fly ash concrete, *Magazine of Concrete Research*. 67(16) (2015) 897–905.
 44. N. Ranjbar, A. Kashefi, G. Ye, M. Mehrali, Effects of heat and pressure on hot-pressed geopolymer, *Construction and Building Materials*. 231 (2020). <https://doi.org/10.1016/j.conbuildmat.2019.117106>.
 45. H. Alanazi, D. Zhang, M. Yang, Z. Gao, Early strength and durability of metakaolin-based geopolymer concrete, *Magazine of Concrete Research*. 69(1) (2017) 46–54. <http://dx.doi.org/10.1680/jmacr.16.00118>.

4. Influence of Curing Temperature and Pressure on the mechanical and microstructural development of metakaolin-based geopolymers

4.1. Introduction

Geopolymers (GP) are inorganic polymers synthesized at temperatures below 100°C, forming cross-linked networks by covalent bonds [1]. They are produced by combining amorphous aluminosilicates with an alkaline or acid activator [2]. Natural minerals, e.g., reactive clays, and industrial waste or by-products, e.g., fly ash, can be used as aluminosilicate precursors, resulting in a three-dimensional network of SiO₄ and AlO₄ tetrahedra linked by oxygen atoms [3].

The chemical, physical, and mechanical properties of GPs are governed by the covalent bonds, as well as the Si:Al atomic ratios [4]. The geopolymerization process is facilitated by increasing curing temperatures [5] as it promotes a dissolution of the precursor and an increased kinetics of the chemical reaction [6], which allows for greater incorporation of Si into the GP structure [7]. However, elevated temperatures may affect early dehydration and therewith volumetric shrinkage [8], potentially contributing to the formation of voids and cracks [9-11]. A tailored design of the solidification regime is essential for achieving a fast setting and strength gain of the resulting GP, while maintaining a homogenous and densely compacted microstructure [12]. A number of existing literature reported optimal geopolymerization achieved by curing temperatures ranging from 40°C to 85°C within short time intervals of 2-48 h at atmospheric pressure [6]. In dependence on material-related factors, e.g., the aluminosilicate source, activators and the ratios between components, the ideal post treatment varies accordingly [3, 7, 8, 11-13].

Another viable post-treatment parameter that warrants further investigation is curing pressure, an aspect that has been relatively understudied. For geopolymers, curing pressure has the potential to either facilitate or impede material reorganization, thereby enhancing microstructure compaction, a factor that might contribute for both mechanical strength and long-term durability [8]. Previous research [9], for instance, showed that when red mud is subjected to atmospheric

pressure, its silicon dioxide components remain insoluble, rendering it unsuitable as an aluminosilicate source. Still, high-pressure and high-temperature curing environments were able to promote the dissolution of the silicon dioxide [14], expanding the range variety of available aluminosilicate sources for alkali-activated products. Under temperature and pressure curing conditions, alkali-activated materials based on volcanic ash exhibited exceptional initial strength and nearly poreless structures [15]. Greater amount of dissolved SiO_2 facilitates the formation of more reaction products, resulting in increased compressive strength [7, 14-16]. Ahmad *et al.* [10] revealed a strong correlation between short-term pressure of 20 MPa and temperature curing of 110°C with heightening the compressive strength from 4 to 12 MPa.

Curing under pressure plays a fundamental role in oil well cementing. However, the prevalent use of Portland cement (PC) in such applications presents challenges. Although OPC can be stabilized with the addition of silicate at temperatures of up to 370°C , it is still challenging with thermal wells [17], due to cracking, chemical attacks, and shrinkage [19]. Compared to class G cement, GPs exhibit a uniform strength development rate, and superior mechanical performance at high temperatures, reaching their ultimate performance within the first 7 days [13, 18].

In terms of durability, Giassudin *et al.* [21] researched curing GP in a saline medium and found an approximately 25% improvement in compressive strength compared to samples cured in water. This improvement was attributed to the greater availability of Na^+ ions, leading to greater structural stability. Nasvi *et al.* (2012) [22] investigated the compressive strength of GPs based on fly ash as compared to cement. GP exhibited elevated strength measurements both at 36°C and 80°C conditions, after 48 h of curing, the latter of impressive 82 MPa, as opposed to the 28 MPa found for PC. Below 40°C , GP exhibits a slower strength progression compared to cement [13]. With the extended curing time, their strength increases gradually due to the continued geopolymerization reaction [23], resulting in greater final strength [13].

When cured under temperature and pressure conditions of 130°C and 20 MPa, Ridha *et al.* [24] reported that the compressive strength of an alkali-activated material based on a high-calcium content fly ash was 141% higher than that of class G cement. Likewise, Salehi *et al.* [19] highlighted that within a mere

24-h timeframe, under curing conditions of 93°C and 20 MPa, the material strength had already surged to 63% of its 14-day value.

At the moment, the formulations tested in order to understand the rheological behavior under temperature and pressure are those containing high calcium content [20, 23], e.g. alkali-activated materials. However, formulations with a low calcium content (which actually correspond to GPs), despite having already defined rheology and its control being attributed to its restructuring capacity, have not yet been evaluated under coupled temperature and pressure conditions.

The determination of the rheology of GP pastes with metakaolin has already been established in several studies carried out by Brandvold *et al.* [27, 28]. These investigations have demonstrated the feasibility of reducing GP viscosity by elevating the liquid-to-solid ratios. Notably, this approach achieved reduced viscosity levels, despite the substantial difference in particle size between ordinary Portland cement (OPC) and metakaolin (MK), with OPC particles being approximately $4 \cdot 10^4$ times larger than those of metakaolin. In addition, the fact that cement hydration kinetics is much faster than geopolymerization explains the lower viscosity of the GP paste due to a greater fluid content between the metakaolin particles, which also slows down the chemical reaction and setting [27]. Physical restructuring of the GP slurry has also been proven after being subjected to extremely high shear, favoring a preferential orientation of the $\text{Al}(\text{OH})_4^-$ and $\text{Si}(\text{OH})_4$ tetrahedra. Thus, the viscosity of the geopolymer paste can be effectively recovered after periods of high shear prior to the onset of setting (~16h) [28].

Therefore, geopolymer materials exhibit significant potential for applications that demand exceptional flowability and restructuring in their fresh state, while also showcasing a controlled progression of strength [20]. To the best of the authors' knowledge, this study represents the inaugural exploration into the feasibility of free-calcium geopolymer mixtures, based on metakaolin, with reference to autoclave curing. Much of the existing research [11, 12, 15] predominantly centers around slag, characterized by its elevated calcium oxide (CaO) content, significantly exceeds the 10% threshold established by ASTM C618 [29] for categorization as a pozzolanic material. This research prioritizes the use of exclusively aluminosilicate-based materials to avoid any potential hybridization within the microstructure. Consequently, due to these specific characteristics, slag

is deemed unsuitable for the production of geopolymer (GP), aligning our material selection closely with the study's core objectives and ensuring the purity of the resulting microstructure.

The current investigation introduces a comprehensive parameter study, encompassing the effects of elevated curing temperatures of up to 200 °C and pressures up to 70 MPa within a saturated regime (100% relative humidity). This temperature range was selected to encompass conditions commonly encountered in both oil wells and various industrial settings, such as cemented pipe lines. In contrast, the pressure values chosen extend beyond typical oil well conditions, allowing for a thorough assessment of the stability of the GP. The study concentrates on the early stages development, specifically 1 and 3 days after mixing. The resultant geopolymer material is strategically engineered to exhibit robust early strength characteristics and resilience in the face of extreme environmental conditions.

4.2. Experimental Program

4.2.1. Materials and geopolymer design

The K-based alkali solution composition used in this study had molar ratios of $\text{SiO}_2/\text{K}_2\text{O}=1.53$ and $\text{H}_2\text{O}/\text{K}_2\text{O}=8.69$. The metakaolin-based geopolymer was designed with $\text{SiO}_2/\text{Al}_2\text{O}_3=4$, as described by [6] and [30]. Metakaolin (MK) was chosen due to its purity and superior participation in the geopolymerization reaction compared to fly ash (FA) at the same temperature. Furthermore, in terms of water curing, FA-based geopolymers exhibited lower compressive strength values (approximately 53.3%) compared to dry curing [21], whereas MK-based geopolymers demonstrated increased compressive strength when cured in water [31]. The potassium silicate solution was prepared as follows: (1) dissolution of potassium hydroxide (PROQUÍMIOS, 88.9% purity, in the form of lentils) in deionized water; (2) gradual addition of hydrophilic silica fume (AEROSIL – Evonik); (3) further mixing the components in a magnetic stirrer for 24 h. After mixing, the liquid was left to rest for additional 24 hours before use. Additionally, an alkali solution based on potassium was chosen due to its ability to produce geopolymers with denser structures and better thermal stability compared to sodium-based systems, as supported by previous studies [32-34]. These decisions

were made to enhance the effectiveness and performance of the produced geopolymer, ensuring optimal results.

The geopolymer formulations were made using a highly reactive metakaolin (MK) powder (tradename MetaMax – BASF, Germany) as the primary source of aluminosilicates. The MK and silica fume composition, physical properties and X-ray diffraction pattern are shown in Table 4.1, Table 4.2 and Figure 4.1, respectively.

Table 4.1 – Composition of metakaolin determined by X-ray fluorescence (XRF), expressed in weight percentages (%wt.).

Material	Al ₂ O ₃	SiO ₂	TiO ₂	Fe ₂ O ₃	K ₂ O	SO ₃	CaO	Others
Metakaolin	50.02	48.28	1.11	0.355	0.109	0.055	0.026	0.045
Silica	-	99.992	-	0.005	-	-	-	0.003

Table 4.2 – Physical properties of metakaolin and silica: BET, density, and average particle size.

Material	BET surface area (m ² /g)	Density (g/cm ³)	Average particle size (µm)
Metakaolin	13.90	2.52	4.60
Silica	200.00	0.03	0.012

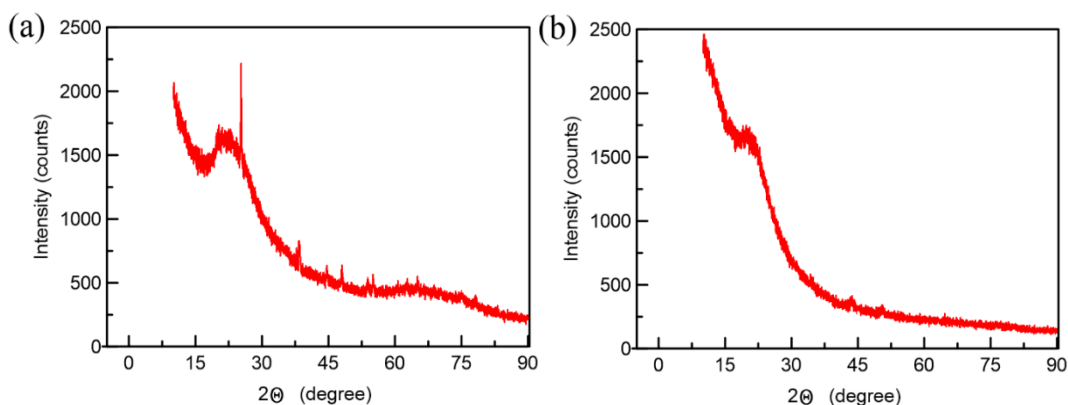


Figure 4.1 – X-ray diffraction (XRD) pattern for (a) metakaolin and (b) silica fume, showing a high degree of amorphicity.

Considering the chemical constituents of the alkali solution and the ones quantified for metakaolin (based on the XRD pattern, Figure 4.1(a), which is predominantly amorphous can be assumed that 100% of the Si and Al content in

the metakaolin is reactive and contributes to the formation of the geopolymer), the mixture design was based on evaluation of previous study [30] so that it had the fastest setting time at room temperature (21°C) and the amount of each component by weight is given in Table 4.3:

Table 4.3 – Composition of geopolymer formulation: detailed breakdown by weight of components.

Composition (g)			
Metakaolin	Alkali solution		
$\text{Al}_2\text{O}_3 \cdot 2\text{SiO}_2$	KOH	H_2O	SiO_2
1000.00	608.03	751.07	500.90

Metakaolin and alkali solution were blended in accordance with the proportions outlined in Table 4.3: specifically, 1860 g of alkali solution was utilized to dissolve 1000 g of metakaolin. The mixing process involved combining the components in an IKA 60 control mixer, operating at 1500 rpm for a minimum duration of 10 minutes to ensure thorough homogenization and maximum reactivity. To achieve this, an IKA dissolver R1300 model paddle was employed, generating radial flow that facilitated movement from top to bottom, thus ensuring high turbulence and intense shear forces within the mixture. Subsequently, the resulting paste underwent vibration at a frequency of 3 Hz for at least 10 minutes to eliminate any trapped air bubbles.

For the uniaxial compressive strength tests, cubic samples with a side length of 50.8 mm were formed by molding the mixture in metallic molds coated with non-stick adhesive tape (Figure 4.2) at room temperature (21°C). The samples were subjected to various curing conditions involving combinations of pressure and temperature. As reference, a group of specimens was stored at room temperature (21°C) and relative humidity (RH = 55%) for 28 days. To prevent early dehydration and cracking, these specimens were wrapped with transparent acetate sheets, following the methodology suggested in previous studies [2, 6, 9-11, 13].

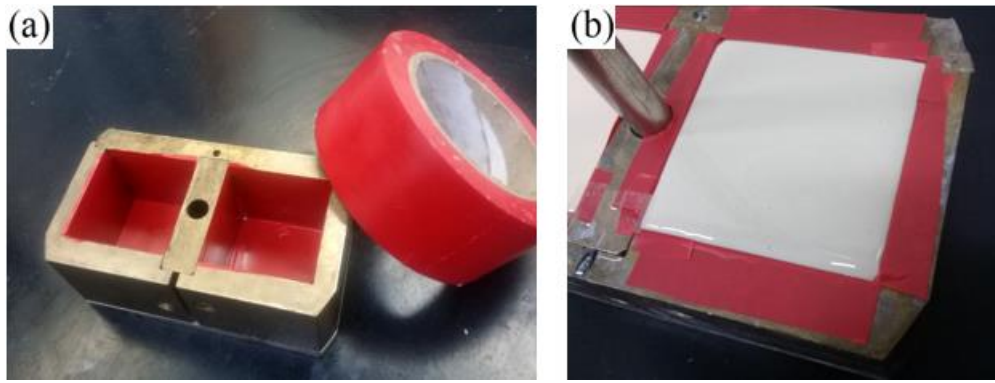


Figure 4.2 – (a) Metallic molds coated with non-stick adhesive tape and (b) Mold filled with fresh geopolymer.

4.2.2. Testing Methods

4.2.2.1. Non-destructive compressive strength evolution

An ultrasonic cement analyzer (UCA) technique was used to investigate the evolution of the GP compressive strength at different temperatures (21°C, 50°C, 90°C, 150°C, 200°C) and pressures (0.1 MPa, 20 MPa, 40 MPa, 70 MPa).

The freshly prepared geopolymer was transferred to the test cell at room temperature (21°C) and the data was collected for 7 days consecutively, every 30 seconds, at the applied temperature or pressure conditions. The equipment (Chandler, model 4265) was calibrated to reach the target temperature in 4 h and the pressure is considered to hit instantly. The equipment, however, is designed to estimate the sonic strength of Portland cement (PC) mixes, from the transit time of the sonic pulse. For the materials with lower density than PC, the acoustic impedance value is lower [35], so consequently the transit time of the sonic pulse will be higher. This prolonged transit time can lead to an underestimation of the material's strength. Thus, due to the unique properties of GP, an alternative algorithm must be employed for their accurate evaluation [5, 20]. Due to Kamali *et al.* [20] used the same equipment to estimate the geopolymer strength synthesized by potassium silicate solution, the fit relation developed by the authors was used to calculate the ultrasonic strength data obtained, according to Equation 4.1:

$$y = 28.662x^2 - 1310.9x + 12057 \quad (4.1)$$

where y corresponds to the ultrasonic compressive strength and x is the pulse transit time.

4.2.2.2. Autoclave curing

A pressurized curing chamber (Chandler, model 1910) was used in this study. The curing parameters involved combinations of temperature and pressure settings. Temperatures of 21°C, 50°C, 90°C, 150°C, 200°C were employed with pressures of 0.1 MPa, 20 MPa, 40 MPa, 70 MPa, at 1 and 3 days, resulting in a total of 40 different temperature-pressure-time conditions. To carry out the curing process, the freshly prepared GP pastes were cast into the 50.8 mm cubic molds, then placed inside a metallic compartment containing deionized water (Figure 4.3), which was subsequently inserted into the pressurizing oil-containing chamber. The equipment was calibrated to reach the target temperature in 4 h and the pressure was considered to hit instantly. The autoclave is regulated through two control mechanisms: (i) Temperature, which is programmed and maintained by an automatic controller system, and (ii) Pressure, which is upheld by the pressure bleed valve. Throughout the specified curing duration, the autoclave maintains the maximum pressure and temperature until just before the end of the process. At this point, the pressure is released through the pressure bleed valve, while the temperature gradually decreases as the heater is deactivated by the automatic controller.

After curing, the samples were allowed to cool down to room temperature before being removed from the chamber, to avoid thermal shock issues. After demolding, all specimens were kept in dry plastic bags afterwards to prevent the risk of premature spalling until compressive tests.



Figure 4.3 - Set used for autoclave curing: stacked metal molds (on the right) and metal compartment for inserting the molds (on the left).

4.2.2.3. Uniaxial compressive strength

The evaluation of uniaxial compressive strength involved testing both the cubic samples (50.8 mm side) that were cured in the pressurized chamber and the reference samples that were cured at room temperature for 28 days, at 21°C, and 55% RH. The tests were carried out on a servo-hydraulic MTS 810/500 (max. capacity of load cell: 250 kN) testing machine, at a displacement rate of 0.5 mm/min. The compressive strength was calculated from the average value of 3 specimens.

4.2.2.4. Thermal stability

Thermogravimetric analysis was performed using a STA 409 cell device from Netzsch, Germany, under an oxygen atmosphere, operated with a heating rate of 10 K/min from 20 °C to 1000 °C and 60 mL/min of gaseous flow. Prior to analysis, all specimens were exposed to iso-propanol to remove free pore water and were subsequently dried out by solvent evaporation. Approximately 15 mg of ground geopolymer powder was used for each evaluation.

4.2.2.5. Porosity

The pore size distribution analysis was conducted using the Mercury Intrusion Porosimetry (MIP) technique within the range of 0.003-100 µm. Measurements were performed on monolithic samples carried out on a Porotec Porosimeter PASCAL 140/440 with a Mercury surface tension of 0.48 N/m, contact angle of 140° and test pressure between 0 to 400.71 MPa. Prior to chemical analysis, all specimens were exposed to iso-propanol for 7 days to fully remove free pore water and were subsequently dried out by solvent evaporation.

4.2.2.6. Morphological analysis

The microstructure of the samples was observed using an Environmental Scanning Electron Microscope (ESEM) model Quanta 250 FEG from FEI, Eindhoven, the Netherlands. The ESEM allowed for fracture surface observation to observe the presence of pores, unreacted phases, and reacted microstructure variations. The analysis was carried out with a secondary electron detector. For the investigation, fractured pieces of geopolymer cubes from compressive strength tests were collected. Pressurized air was used to meticulously remove any dust and

extraneous debris from the surfaces of the cracks. This careful cleaning process was essential to ensure that the samples were as clean as possible, enabling accurate imaging for the analysis.

4.3. Results and discussions

4.3.1. Transient state properties

In Figure 4.4, the strength gain is plotted as a function of curing time, considering different target temperatures. It can be observed that at room temperature (21°C), the GP exhibits a significantly slower strength gain due to the slower rate of geopolymerization [7, 13]. However, as the curing temperature is increased, the strength gain accelerates. This is attributed to the thermally facilitated dissolution of Si and Al atoms, particularly noticeable from 50°C onwards. It is worth noting, however, that beyond 150°C, the strength of the GP begins to diminish. This decrease can be attributed to the possible suppression of ion transport, thereby reducing the geopolymer reactivity.

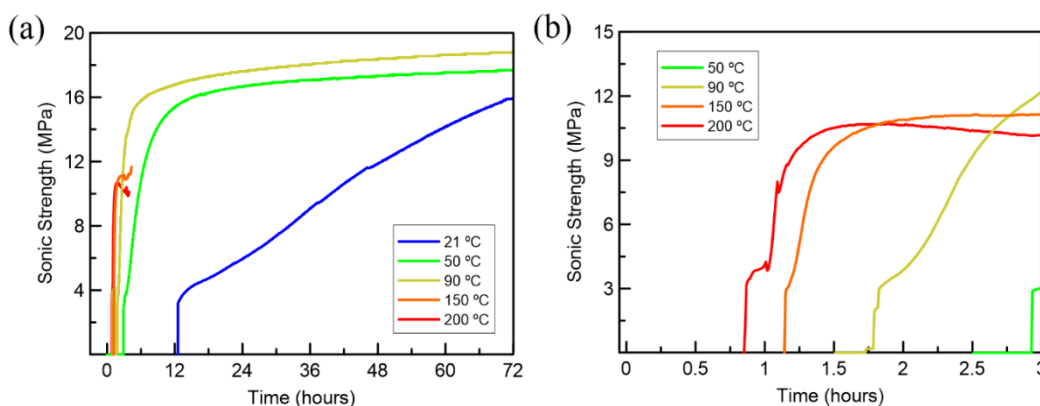


Figure 4.4 – (a) Compressive strength gain as a function of curing time at various curing temperatures (21°C, 50°C, 90°C, 150°C, and 200°C) at 1 atm and (b) zoomed portion to demonstrate the difference in initial setting from 50°C to 200°C.

Elevated temperatures have a positive effect on the geopolymerization process, leading to faster strength development [5, 6, 20]. Curing at elevated temperatures up to 90°C enhances the rate of initial strength gain [6, 7, 20]. The majority of the geopolymerization process is completed within 16 h of curing from 50°C [13]. However, at a lower curing temperature (below 50 °C), a longer time is required to reach maximum compressive strength [5, 8].

It is worth noticing, however, that cracks were formed in the geopolymer after 260 min and 235 min of curing at 150°C and 200°C, respectively, as shown in Figure 4.5. These cracks result from the thermal shrinkage experienced during high-temperature curing [5, 12, 23] and occurs in transverse direction due to the formation of laminated structures, as seen in ESEM images (Figure 4.19). Furthermore, although it is generally understood that maintaining controlled humidity can prevent dehydration at elevated temperatures [12], it should be noted that the water evaporation within the GP at these temperature ranges introduces additional stress concentrators under high thermal pressures. This is accompanied by changes in volume due to thermal dehydration [5, 36], leading to the formation of cracks and defects, and therewith reducing the overall strength of the GP.

It is important to point out that the contraction of the geopolymer continued until reaching the maximum strength value at both temperatures. This is evident from the consistent increase in equipment pressure until that point. Thus, despite the increase in temperature favors the increase of the Si:Al reaction ratio in shorter time spans [8], this is not only parameter influencing the compressive strength of the geopolymer.

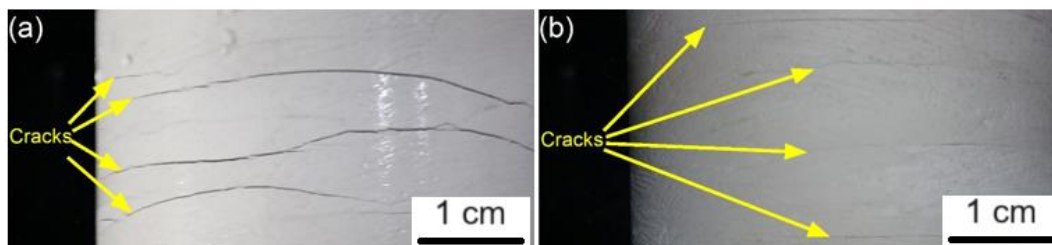


Figure 4.5 – Formation of microcracks in the geopolymer after testing in the UCA at (a) 150°C and (b) 200°C.

Figure 4.6 illustrates the strength gain at room temperature (21°C) as a function of curing time, considering different curing pressures. Notably, the plot reveals that there is no significant difference in strength between 24 h and 40 h of curing at 0.1 MPa, 20 MPa and 40 MPa. However, for all pressures other than 0.1 MPa, the sonic strength shows an immediate increase following data acquisition. This increase can be attributed to different factors. Firstly, the pressure applied during curing enhances the solubility of the oxides involved in the geopolymerization [14], accelerating its setting. Secondly, the higher pressure reduces the presence of voids [10-12, 26], resulting in a dense and homogenous

microstructure.

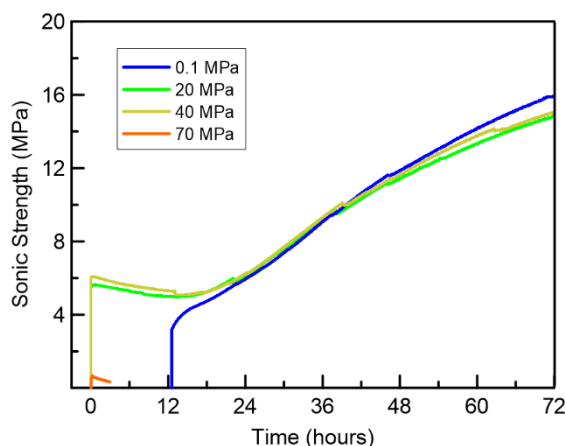


Figure 4.6 – Compressive strength gain at room temperature (21°C) as a function of curing time at various curing pressures (0.1 MPa, 20 MPa, 40 MPa, 70 MPa).

Regarding the curing at 70 MPa, an initial strength gain was observed until approximately 175 min. However, after this time, no measurements could be recorded by the equipment for the following 24 h. Upon demolding, radial cracks were recognized in the geopolymer, confirming the formation of microcracks induced by the combination of wet curing and paste contraction at 70 MPa [36]. The restricted exit of water from within the geopolymer material likely created internal stresses, contributing to the crack formation [5], which prevented sonic strength measurements.

Research on the curing of calcium-based alkali-activated materials solely through temperature or pressure is limited. Khalifeh *et al.* [37] demonstrated that at 125°C, the compressive strength of such materials peaks within a day before declining. Similarly, Alvi *et al.* [38] observed that a pressure of 14 MPa did not influence the setting time.

4.3.2. Hardened properties

4.3.2.1. Temperature effect

Figure 4.7 displays the destructive compressive strength values recorded for

the GP as a function of curing temperature at both 1 and 3 days.

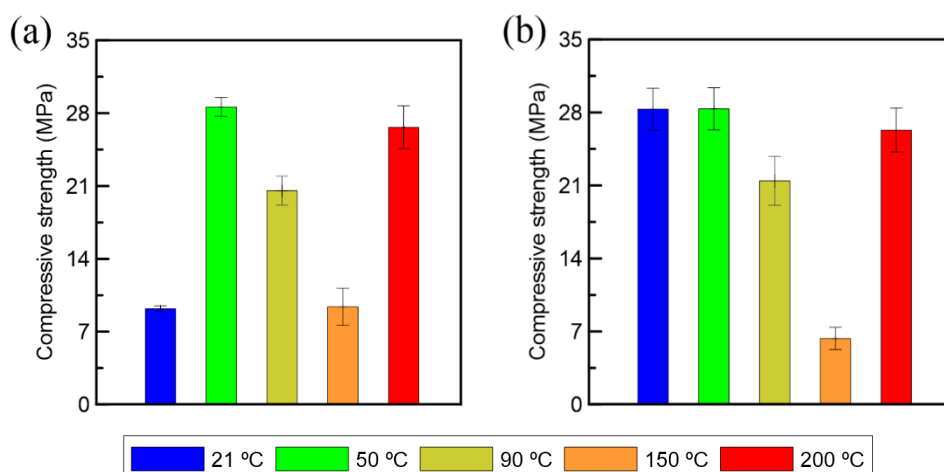


Figure 4.7 – Compressive strength at different curing temperatures (21°C, 50°C, 90°C, 150°C, 200°C) at ambient pressure (0.1 MPa) for (a) 1-day curing and (b) 3-day curing.

At ambient temperature (21°C), the geopolymer samples showed a rapid initial dissolution, indicating a fast reaction, but the rate of formation of reaction products and strength gain was slower compared to elevated curing temperatures, which is consistent with the results shown in Figure 4.4. Within 1 day at 21°C, there may not be sufficient time and temperature to remove free water and strengthen the inorganic polymer bonds, keeping the geopolymer fresh at early stages. In contrast, at temperatures above 50°C, the initial geopolymerization reaction occurred more rapidly, leading to rapid strength development [11, 39]. The rate of product formation became the controlling factor for strength gain, as observed in previous studies [8].

The increase in early strength with elevated temperatures is attributed to a faster chemical reaction [6, 7, 10-12, 15, 20]. Elevated temperature favors the reaction kinetics and the incorporation of Si into the product, contributing to the densification of the microstructure [6-8]. The strength of the geopolymer increased with curing temperature up to 90°C and then declined beyond that threshold, attributed to the fast evaporation of free water within the pores. It has also been noted that curing at such high temperatures leads to increased geopolymer contraction, which causes cracks and reduces strength. The solubility of Al_2O_3 increases with temperature [14], increasing its amount in the geopolymer and thus

contributing to the decrease in strength. Interestingly, at 200°C, the strength was higher than at 150°C, due to increased geopolymerization and stiffening between 200°C and 400°C ranges [39].

The compressive strengths of the samples were significantly lower than the reference sample (37.11 ± 0.24 MPa), as the total reaction product content was only nominally identical when ultimate strength was achieved at all curing temperatures. Notably, the 28-day cured specimens exhibited substantial strength improvement compared to the 3-day samples, indicating a greater degree of geopolymerization [40].

4.3.2.2. Pressure effect

Figure 4.8 shows the relationship between compressive strength and curing pressure at 21°C for aging of 1 and 3 days. The compressive strength of geopolymer displays an ascending trend up to a curing pressure of 20 MPa. This is attributed to a reduction in the number of voids [10, 12, 15, 26] causing the particles to be strongly bound and promoting the geopolymerization reaction [10, 12]. Similar to temperature, early-age strength development in geopolymer can be obtained through pressure curing, leading to a continuous formation of reaction products and enhanced silica enrichment in solids-based processes [7, 8, 10, 16]. Higher curing pressure significantly improves the solubility of oxides and Si-O-Si bonding in the pressure-treated samples, indicating greater reactivity [9, 16].

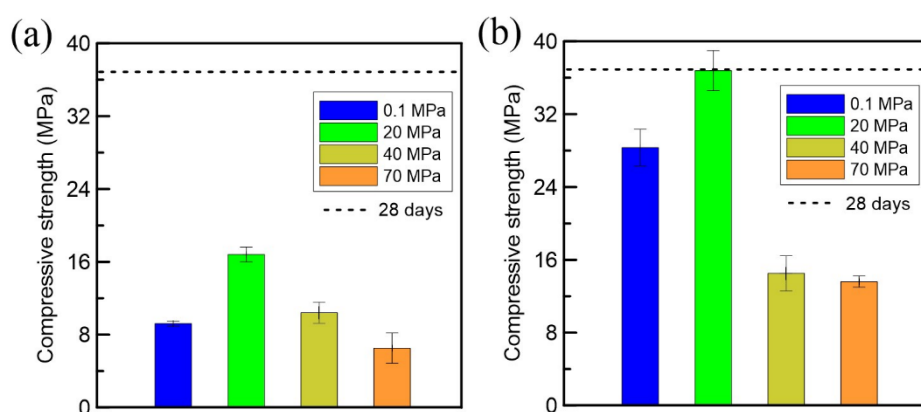


Figure 4.8 – Compressive strength at different curing pressures (0.1 MPa, 20 MPa, 40 MPa, 70 MPa) at 21°C for (a) 1-day curing and (b) 3-day curing.

During the aging process of the geopolymer, microstructural changes occur, affecting its mechanical properties. A molding pressure of 20 MPa is beneficial in improving early compressive strength [12], as shown in Figure 4.8, at room temperature (21°C). However, further increments above 20 MPa yield no additional improvement, associated with the fact that the precursor particles are solid and incompressible, rendering the extra pressure ineffective. Furthermore, excessive pressure can lead to crack nucleation [10]. In contrast, when heat alone is employed, marginal improvements in strength from 1 to 3 days are observed [10], as shown in Figure 4.7. Combining pressure and extended time, however, can result in a remarkable 118% increase in strength.

4.3.2.3. Combination of temperature and pressure effects

In light of the observed effects of pressure and temperature, it is convenient to discuss their combined effects. Figure 4.9 illustrates the outcomes of compressive strength for all combinations of curing pressure and temperature analyzed, carried out at 1 and 3 days.

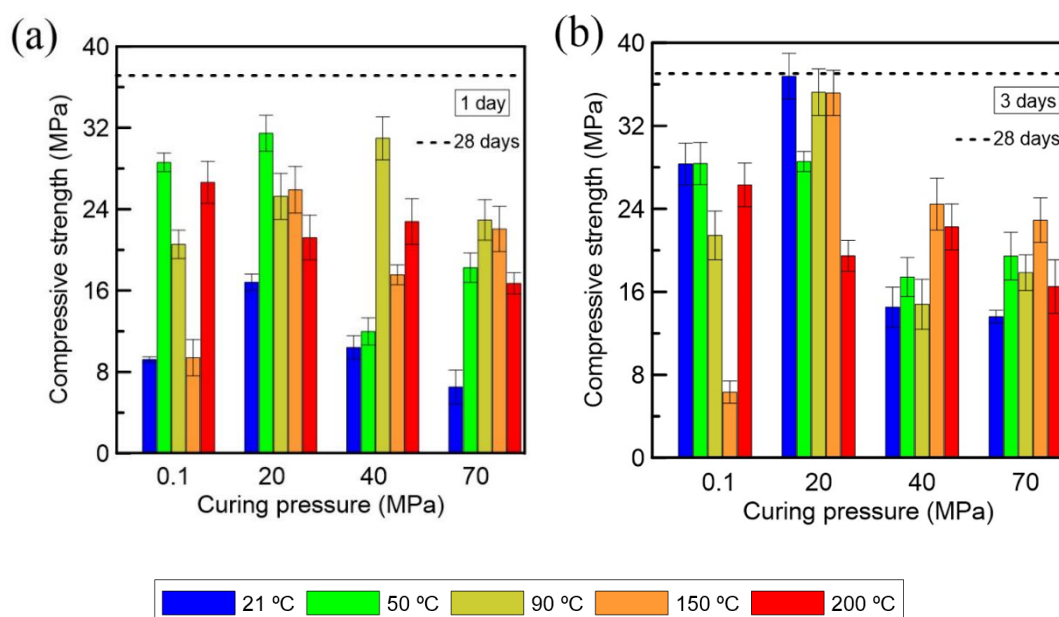


Figure 4.9 – Compressive strength for different combinations of temperature and curing pressures at (a) 1-day curing and (b) 3-day curing.

High-temperature and high-pressure curing have been acknowledged for their ability to facilitate incremental dissolution, coupled with increased curing time

[7, 14, 15]. The greater the amount of dissolved SiO_2 , the more reaction products are generated, favoring an increase in compressive strength [7, 14-16]. Furthermore, the rate of solid-based reactions (which are affected by pressure) is also favored by increasing temperature [8]. This is attributed to the reduction of pores (curing pressure), thereby increasing the dissolution of metakaolin particles in the geopolymerization process [10, 15]. This observation substantiates the contrast in compressive strength under thermal curing conditions at 20 and 40 MPa [10].

Given a consistent content of solid precursors across all temperature and pressure conditions tested, the compressive strength at 1 day is predominantly influenced by the extent of dissolution due to a relatively highly alkaline environment. This environment is characterized by a high $\text{K}_2\text{O}/\text{Al}_2\text{O}_3$ ratio and low $\text{H}_2\text{O}/\text{K}_2\text{O}$ ratio. On the other hand, the compressive strength at 3 days is more significantly affected by the degree of geopolymerization and thermal stress applied during curing [41].

Exposing the material to very high pressures can lead to liquid loss, as exposed in [10], increasing the alkalinity of the GP. This enhanced alkalinity in conjunction with temperature, can expedite the geopolymerization process due to the synergistic effects of heat and pressure, facilitating the expulsion of air bubbles (via enhanced diffusion) and promoting efficient heat transfer [15]. Consequently, a denser microstructure and an increased prevalence of closed pores, in contrast to a continuous pore network, can be achieved [7, 15]. Alterations in curing pressure and temperature optimize the polymerization degree for (SiO_4) and (AlO_4) monomers [9]. This phenomenon could potentially account for the contrasting behavior between samples cured at 200°C and those cured at 150°C .

Comparing the effects of pressure and temperature curing alone to those of combined pressure, temperature and aging, showed a marginal difference. Notably, the most substantial strength increase occurs in the case of a pressure of 20 MPa. However, specimens subjected to 70 MPa exhibited consistent compressive strength between 1 to 3 days of curing. This phenomenon may be attributed to structural non-uniformity stemming [42].

For a better understanding of the compression behavior of GP after being subjected to different curing conditions (temperature and pressure), Figure 4.10 is presented.

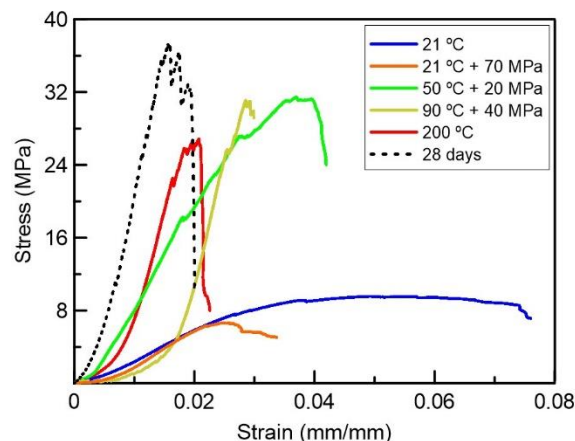


Figure 4.10 - Stress-strain curves illustrating the behavior of select specimens subjected to uniaxial compression testing.

After one day of curing at room temperature (21°C), the geopolymer (GP) is still undergoing the hardening process, as evidenced by its higher deformation and relatively low strength compared to other curing conditions. This observation is further supported by the noticeable differences in microstructures between specimens cured for 1 and 28 days (see Figure 4.18). Interestingly, curing at 21°C with a pressure of 70 MPa shows minimal change in strength compared to atmospheric pressure. However, the specimen experiences less deformation due to increased particle proximity, as indicated by both mercury intrusion porosimetry (MIP) results (see Figure 4.16) and microstructural analysis (see Figure 4.21). As the curing temperature rises from 50°C to 200°C, the geopolymer's strain capacity decreases due to increased porosity (see Figure 4.15). The optimal balance between strength and deformation is achieved at a curing temperature of 50°C and a pressure of 20 MPa.

4.3.2.4. Correlation with sonic strength

The change in sonic strength development, as determined by the standard algorithm for class G cement, shown in Figure 4.4 and Figure 4.6, does not align with the values obtained with the destructive tests presented in Figure 4.7 and Figure 4.9. To address this discrepancy, the adjustment developed by Kamali *et al.* [20] was implemented and the results are depicted in Figure 4.11:

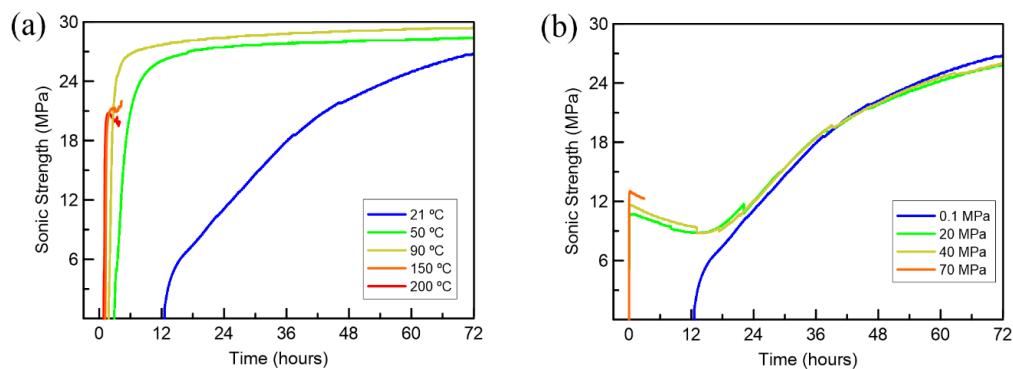


Figure 4.11 – Compressive strength gain at different curing temperatures and pressures, corrected by an adjustment made by Kamali *et al.* [20].

The uniaxial compressive strength data (Figure 4.4 and Figure 4.8) compared with the values in the fitted curves (Figure 4.11) shows a low correspondence. Therefore, the results of the ultrasonic cement analyzer (UCA) cannot be used in quantitative terms, but only for qualitative purposes.

4.3.4. Thermal Analysis

Figure 4.12 shows the weight loss experienced by post-cured samples under different temperature and pressure conditions when subjected to controlled heating.

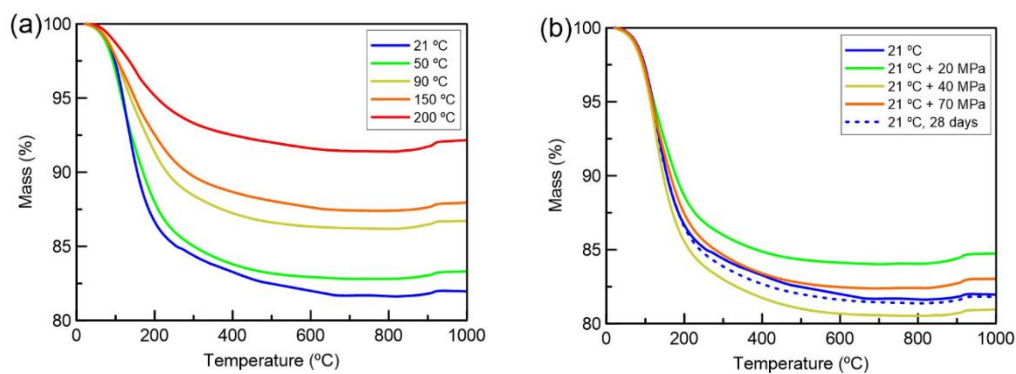


Figure 4.12 – Thermogravimetric curves of specimens cured for 1 day at (a) different temperatures and (b) under different pressures.

A decrease in sample weight was observed between the temperature range of 150 °C and 250 °C. This could be attributed to the evaporation of both physically adsorbed and chemically bound water [3]. Illustrated in Figure 4.12(a), there is a noticeable trend: at elevated temperatures (from 150 °C), the weight loss becomes less pronounced, since most of the physically bound water has been removed in the previous steps, indicating less reactivity. However, an interesting observation

emerges concerning the effect of curing pressure, as shown in Figure 4.12(b).

Notably, when subjected to a curing pressure of 20 MPa, the geopolymer exhibited less significant water loss, compared to all other pressures. The variance in these outcomes could be attributed to different pore diameter range, supported by the measurements obtained with MIP analysis, as further investigated in Figure 4.16.

This weight loss is also evident when examining the DTG curves, as shown in Figure 4.13. As temperature rises, all geopolymers exhibited weight loss peaks, with once again the most significant mass reduction occurring between 80°C and 250°C. It is conceivable that the reductions in strength observed in this temperature range are detrimental effects of rapid water evaporation, leading to microstructural damage [39].

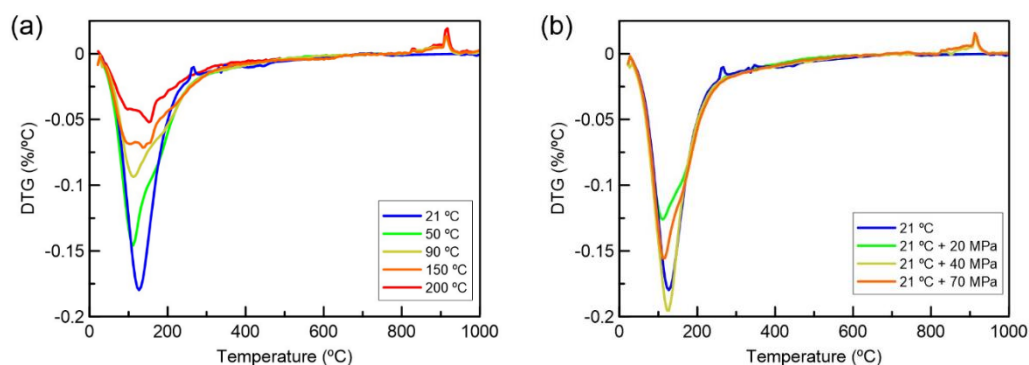


Figure 4.13 – DTG curves of specimens cured for 1 day at (a) different temperatures and (b) under different pressures.

Figure 4.13(b) demonstrates the highest mass loss rate within this temperature range under a curing pressure of 40 MPa. This is likely due to the fact that higher pressure retains a larger volume of free water within the micropores. The thermal stability of geopolymer increases with a curing pressure of 20 MPa and can be associated to a reduction in the number of voids [10, 12, 15, 26] and as discussed earlier, pressure curing leading to an increase in the formation of reaction products. However, for pressure above 20 MPa there was no additional improvement, because excessive pressure can lead to crack nucleation [10].

The synergistic interplay between temperature and pressure effects during curing is presented in Figure 4.14, displaying the TGA and DTG curves for the geopolymer cured at 50°C for 1 day.

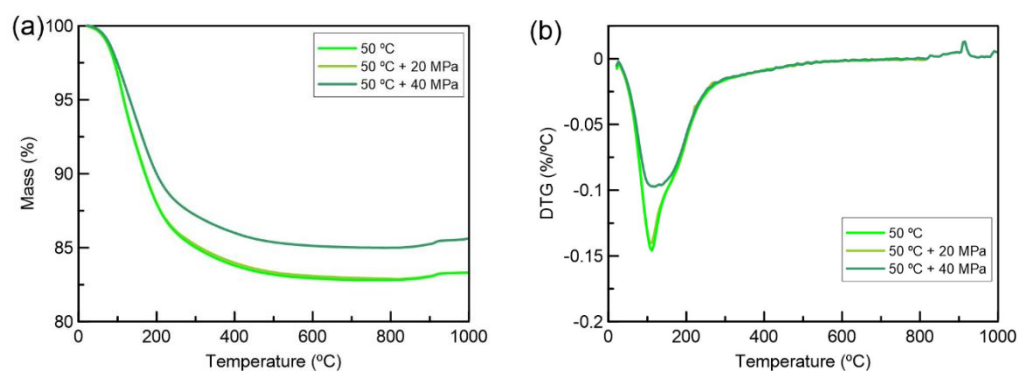


Figure 4.14 – (a) TGA and (b) DTG curves for geopolymer cured for 1 day at 50°C under different pressures.

Strikingly, even post autoclave, residual and chemically bound water persists [42], with the degree of geopolymer condensation dependent on pressure and heat effects. Significant mass loss occurs between approximately 110°C and 200°C related to the evaporation of physical and chemically bound water [15].

Regardless of temperature, heightened external pressure expels a notable portion of trapped air. Temperature then accentuates water evaporation, thereby depleting the voids occupied by water and promoting further compaction. Curing under 40 MPa and 50°C can result in loss of liquid in addition to increase the alkalinity of the GP, as demonstrated by [10]. Under higher alkalinity along with temperature it can accelerate the geopolymerization process [15].

It is important to mention the peak that appears in the DTG curves around 900°C, where the shrinkage tends to accelerate, a phenomenon called viscous sintering [43], the main characteristic is the increase in crystallinity [44] driven by free alkalis [45].

4.3.5. Porosimetry

The classification of pore types is based on a previous study [6], establishing four categories: nanopores (3-10 nm), mesopores (10-50 nm), macropores (50-200 nm), and pores exceeding 200 nm. It's noted that micropores and mesopores exhibit favorable characteristics, while macropores have detrimental effects [12], as they are closely associated with reductions in strength and durability. Figure 4.15 displays the porosimetry results, illustrating cumulative and differential pore volumes for samples subjected to different curing temperatures and atmospheric pressure conditions (0.1 MPa).

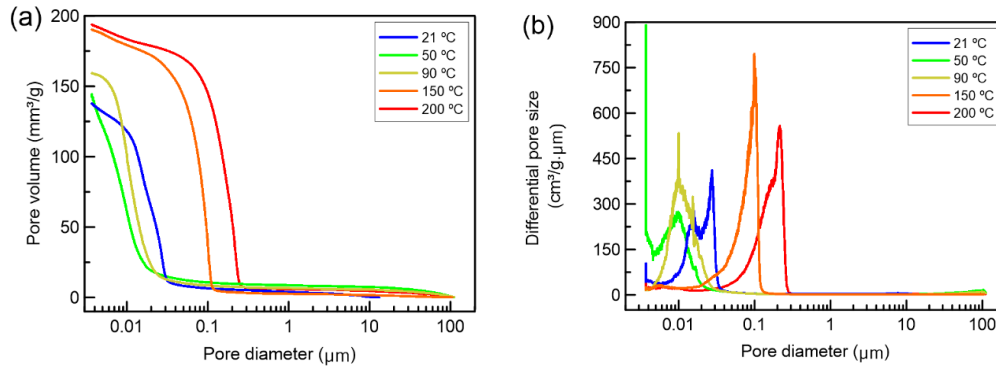


Figure 4.15 – (a) Cumulative pore volume and (b) pore size distribution for geopolymer cured for 1 day at different temperatures (21°C, 50°C, 90°C, 150°C, 200°C) at 1 atm.

Samples cured up to 90°C reveal a prominent peak in the pore size distribution spanning 5 to 30 nm, indicating consistent nanoporosity [6]. The decrease in porosity observed in heat-cured specimens is attributed to enhanced dissolution of aluminosilicate particles, expediting geopolymerization [10]. These findings are consistent with trends observed in compressive strength values (Figure 4.7(a)).

For samples subjected to curing temperatures of 150°C and 200°C, there is a simultaneous increase in porosity alongside an expansion in the range of pore sizes. This is attributed to excessive water evaporation [6, 10] and the process of dehydroxylation [10], involving the addition of hydrogen to a hydroxyl group. Figure 4.16 illustrates the outcomes of porosimetry evaluations conducted on samples cured for one day, encompassing a variety of pressure conditions at room temperature (21°C).

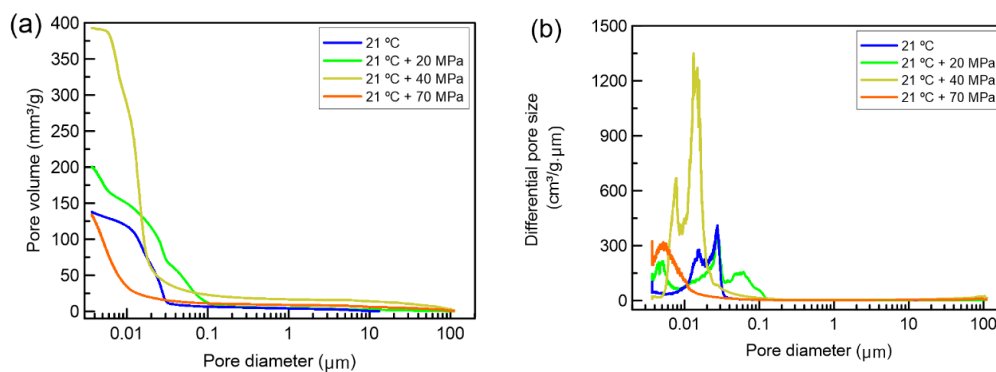


Figure 4.16 – (a) Cumulative pore volume and (b) pore size distribution for geopolymer cured for 1 day at different pressures (0.1 MPa, 20 MPa, 40 MPa, 70 MPa).

Elevated curing pressures manifest a dual impact: a notable reduction in nanopore volume, coupled with a significant expansion in trapped air space volume, as evidenced by the bimodal pore size distribution in pressure-cured specimens, with the exception of the 70 MPa condition, which exhibited the opposite effect. At this juncture, it is pertinent to note that the observed increase in strength associated with the 20 MPa curing pressure could potentially be attributed to the heterogeneous distribution of pore sizes present. This diverse array has the potential to mitigate internal stresses induced by the geopolymer's expansion during curing, as elucidated in a prior study [38].

However, it is intriguing to observe that specimens subjected to a curing pressure of 70 MPa, despite showcasing the least porosity and the most limited pore size range, paradoxically demonstrate lower compressive strength in comparison (Figure 4.7(a)). This trend could plausibly be attributed to the accumulation of internal stresses resulting from the geopolymer's contraction within the constraints of a more restricted assortment of smaller pores. This heightened concentration of stresses renders the material more susceptible to crack initiation and propagation. For a comprehensive examination of the influence of temperature and pressure on porosity, please refer to Figure 4.17, which delineates the porosimetry findings for geopolymers cured at 50°C and 150°C for one day.

These findings underscore the intricate interplay between curing pressure and temperature in enhancing favorable pore characteristics while concurrently promoting compaction of the porous structure, thereby bolstering mechanical properties [12]. Possible mechanisms contributing to the decrease in porosity include the expulsion of entrapped air through pressure application, followed by further removal via exposure to elevated temperatures [10].

When samples are subjected to curing conditions at 50°C and 20 MPa, the presence of a distinctive bimodal pore size distribution, characterized by well-defined and separated peaks, serves as a mechanism to mitigate internal stress arising from the geopolymer's expansion during the curing phase, as previously explained. In contrast, for specimens cured at 150°C and 20 MPa, the intentional reduction in porosity assumes a central role in accelerating the rapid establishment of early-age compressive strength, as illustrated in Figure 4.9. Table 4.4 provides a summary of the porosity values for the results presented in Figures 4.15-17.

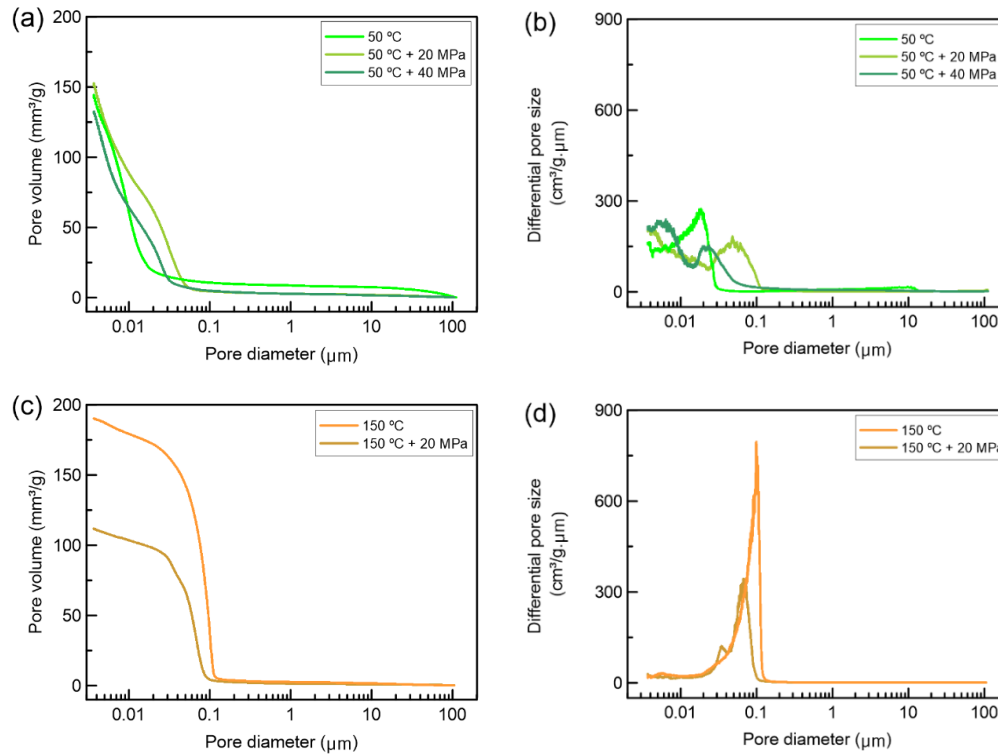


Figure 4.17 – (a) Cumulative pore volume and (b) pore size distribution for geopolymer cured for 1 day at 50°C different pressures (0.1 MPa, 20 MPa, 40 MPa); (c) Cumulative pore volume and (d) pore size distribution for geopolymer cured for 1 day at 150°C different pressures (0.1 MPa, 20 MPa).

Table 4.4 – Porosity (%) measurements for geopolymers submitted to different curing regimes (temperature and pressure) after 1 day of curing.

Curing parameters		Porosity (%)				
		Temperature (°C)				
		21	50	90	150	200
Pressure (MPa)	0.1	22.97	14.68	25.24	58.84	28.81
	20	29.38	24.86	-	18.82	-
	40	46.84	21.24	-	-	-
	70	21.59	-	-	-	-

4.3.6. Microstructure

After just one day of curing, the formation of a gel phase is evident, as illustrated in Figure 4.18(a). This early-stage gel phase is accompanied by white-colored unreacted metakaolin (MK) particles and microstructural porosity. Over the course of 28 days, this porosity undergoes slight densification.

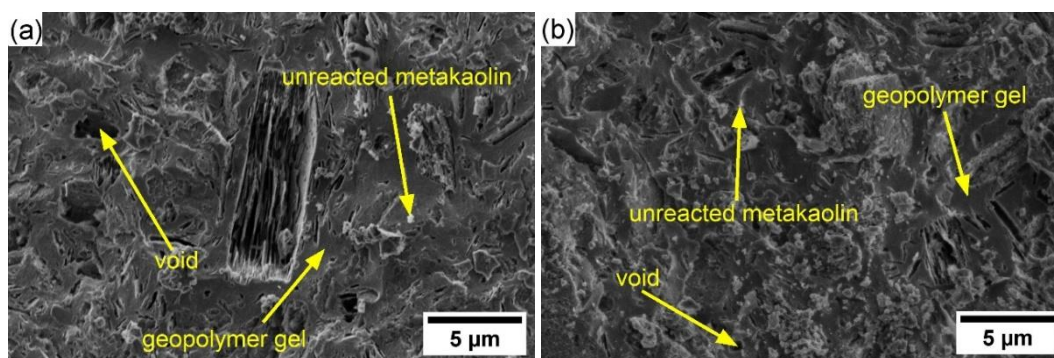


Figure 4.18 – Microstructure of samples cured at 21°C in (a) 1-day curing and (b) 28-days curing.

As illustrated in Figure 4.18(b), the microstructure exhibits a subtle increase in densification at the 28-day mark. This enhanced level of geopolymerization carries implications for enhanced mechanical properties and refined microstructure, making them particularly well-suited for demanding high-performance applications [41]. The remarkable 402 % upswing in compressive strength after a 28-day finds its interpretation in the achieved denser microstructure, as elucidated in an earlier investigation [12]. Evidently, this intricate interplay between microstructural attributes and macroscopic features, including strength, echoes through various research studies [10, 46, 47]. Evidenced by the findings from the ultrasonic cement analyzer, an unequivocal correlation emerges between heightened temperature and the acceleration of the geopolymerization process, as visually demonstrated in Figure 4.4. Figure 4.19 shows the microstructure of samples cured under different temperatures for 1 day. A porous microstructure becomes apparent through thermal curing, where a marked contrast is observed in comparison to samples cured at 21°C, wherein unreacted particles remain visible. This observation stands as evidence of the heightened geopolymerization facilitated by temperatures [13], which is evidenced by the apparent reduction in unreacted metakaolin particles compared with curing at 21°C (Figure 4.18(a)).

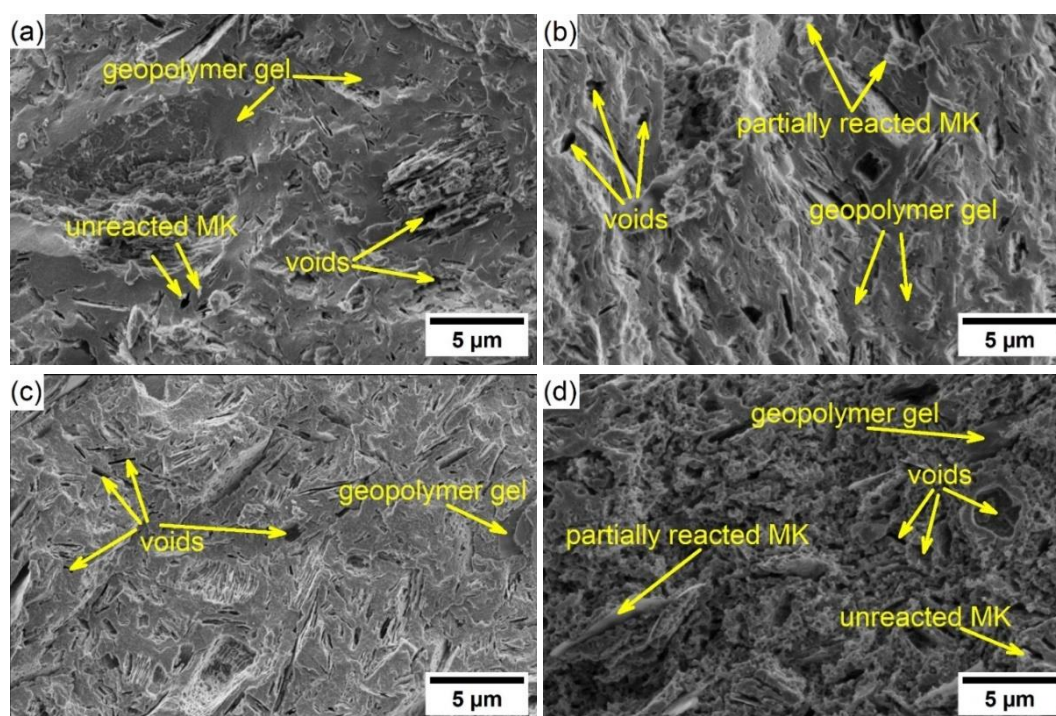


Figure 4.19 – Microstructure of samples cured for 1 day at (a) 50°C, (b) 90°C, (c) 150°C, (d) 200°C.

Notably, a reduction in microstructural porosity can be observed for specimens cured at 50°C (Figure 4.19(a)), aligning well with the observations from compressive tests. While the microstructure cured at 200°C displays a comparatively higher degree of porosity in contrast to those cured at 150°C (Figure 4.19(d) and Figure 19(c), respectively), a congruent outcome is corroborated by MIP analysis (Figure 4.15). The compressive strength of the former registered a remarkable was about 300% superiority over the latter (Figure 4.7(a)).

Microscopic examination of the sample cured at 200°C (Figure 4.17) reveals the presence of debris of a similar shape distributed all over the entire surface. These particles could originate from one of two possible causes. The first possibly arises from damage related to microcracking within the pore structure when exposed high-temperature curing. This is suggested because the morphology of the pores associated with water loss primarily exhibits a spherical nature. This characteristic aligns with the smooth central region of the identified debris. Alternatively, the second assumption is that two metakaolin particles have merged due to the rapid loss of water resulting from the elevated curing temperature.

Microscopic examination of the sample cured at 200°C, as shown in Figure 4.20, reveals the widespread distribution of similarly shaped debris across

the entire surface. Initially, based solely on visual analysis, the origin of these debris could only be speculated. One potential cause might be damage due to microcracking within the pore structure, a consequence of high-temperature curing and associated water loss, given that the debris primarily exhibits a spherical shape in between their contact. An alternative hypothesis could be the fusion of two metakaolin particles, driven by the rapid dehydration at elevated curing temperatures. Nonetheless, a detailed analytical assessment using Energy Dispersive Spectroscopy (EDS) revealed that the debris predominantly consists of carbon (C) and sulfur (S). This composition strongly indicates a chemical reaction stemming from the interaction between the demolding tape and the geopolymer (GP) under conditions of high pressure and temperature, challenging initial assumptions and directing focus towards material interactions not previously considered. This finding underscores the necessity for more meticulous preparation methods when considering further increases in curing temperature in future studies, to mitigate unforeseen reactions and ensure the integrity of the sample.

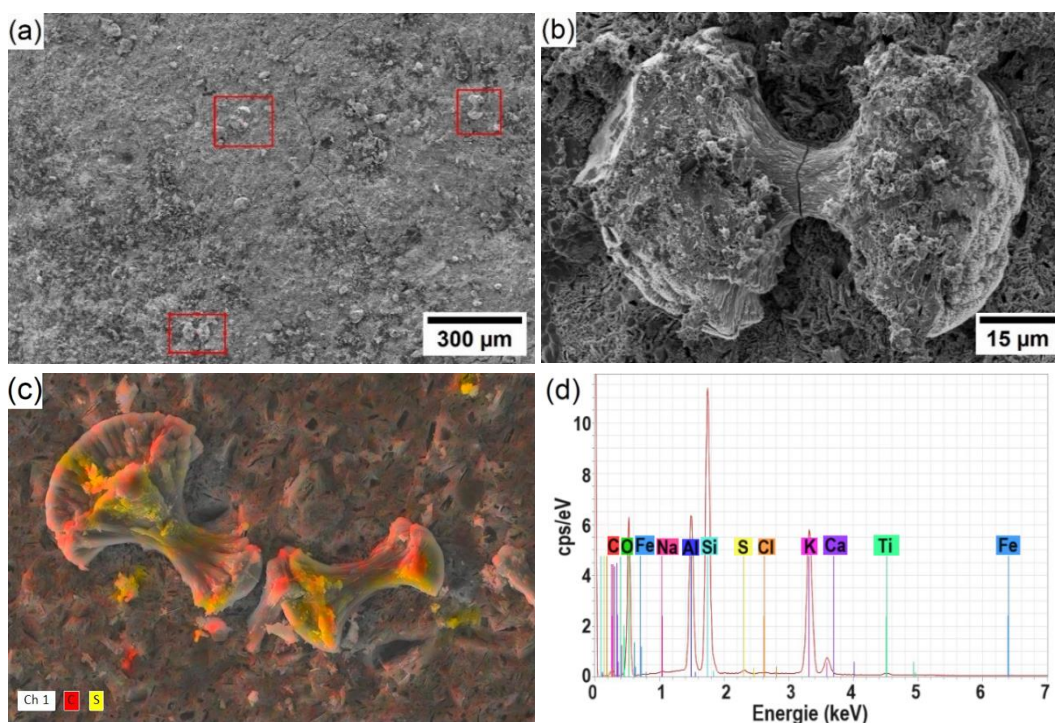


Figure 4.20 – Microstructure of the geopolymer cured at 200°C showing the presence of (a) debris (marked by red rectangles); (b) a debris in detail; (c) EDS map and (d) EDS spectrum.

The presence of these similarly-shaped debris is not a result of the preparation

method and may be the result of geopolymer's microstructure evolution. More specific techniques would be needed to identify the presence of zeolites, which is outside the scope of this paper. But, according to the literature [48] at a temperature of 200°C, no zeolite was formed despite this structure formed could be dumbbell shaped zeolite [49], but scientific proof would be necessary. It may even be interesting to evaluate in future studies whether pressure combined with temperature can trigger the formation of zeolites at temperatures lower than those reported in the literature.

Figure 4.21 shows the microstructure of samples cured for 1 day at 21°C under different pressures.

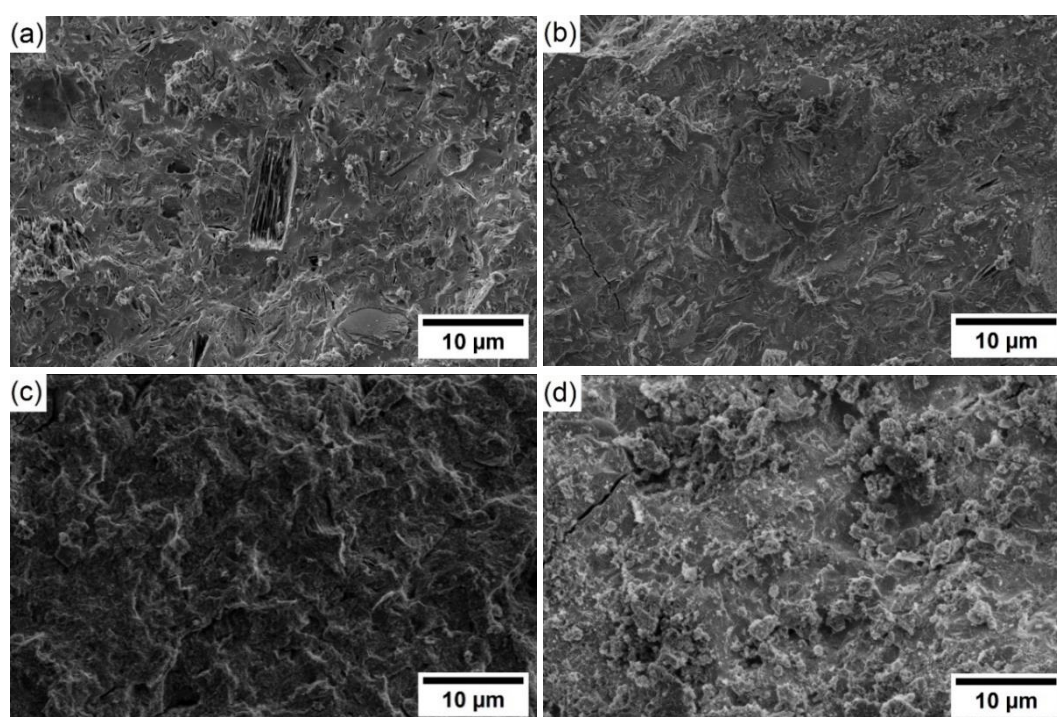


Figure 4.21 – Microstructure of the geopolymer 1-day cured at 21°C under the pressure of (a) 0.1 MPa (atmospheric pressure); (b) 20 MPa; (c) 40 MPa; (d) 70 MPa.

The microstructures obtained through different curing pressures exhibit significant variations. Specimens subjected to elevated pressures demonstrate a notably enhanced and stable structure [15], corroborating the findings from TGA analysis (cf. Figure 4.13(b)). This phenomenon can be attributed to the pressure role in diminishing inter-particle voids, thereby facilitating heightened particle contact and augmenting reactivity [12]. Particularly, the microstructure of the

specimen cured at 20 MPa (as depicted in Figure 4.21(b)) showcases uniformity and denseness.

Pressure emerges as a pivotal factor influencing specimen porosity, illustrated prominently at the 40 MPa pressure level where the microstructure displays increased porosity (Figure 4.21(c)), consistent with MIP outcomes (compare with Figure 4.16). Furthermore, specimens cured at 70 MPa exhibit a homogeneous microstructure (Figure 4.21(d)).

In order to assess the combined effect of temperature and pressure on morphology, Figure 4.22 and Figure 4.23 present the microstructure of samples cured at 50°C and 150°C for 1 day, respectively.

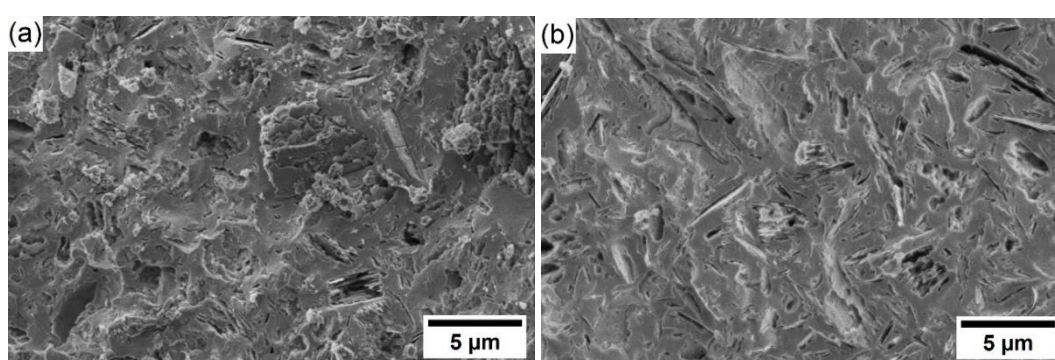


Figure 4.22 – Microstructure of the geopolymer 1-day cured at 50°C under the pressure of (a) 20 MPa; (b) 40 MPa.

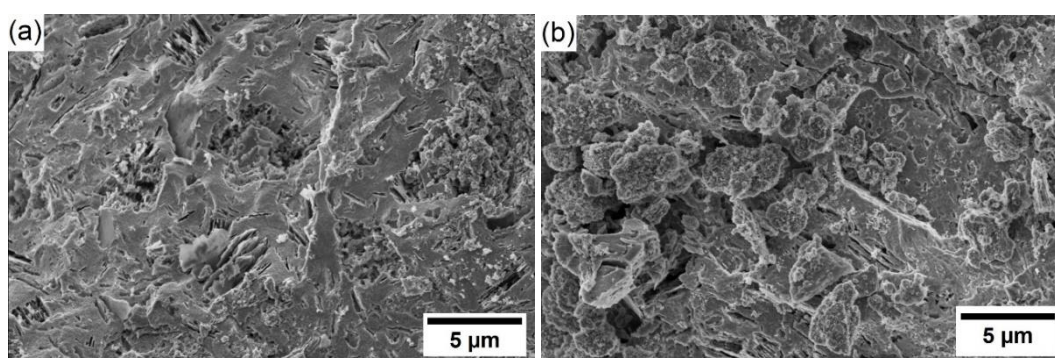


Figure 4.23 – Microstructure of the geopolymer 1-day cured at 150°C under the pressure of (a) 20 MPa; (b) 40 MPa.

Thermal curing conducted at 50°C yields a more porous microstructure as the pressure increases, also supported by MIP analysis results (Figure 4.17). Interestingly, although the microstructure achieved through curing at 50°C and 40 MPa exhibits lower porosity compared to that obtained at 50°C and 20 MPa

(Table 4.4), the resultant strength is compromised (depicted Figure 4.9(a)). This outcome might be attributed to the comparatively less compact nature of the former when contrasted with the latter, discerned from the pore size distribution analysis of the geopolymer (as illustrated in Figure 4.17(b)).

However, curing at 150°C introduces a notable shift in the scenario: the increased pressure contributes to compaction, primarily attributed to the diminished evaporation of free water [15]. Under these conditions, the synergistic effect of elevated pressure and temperature fosters pore volume reduction while promoting the formation of a more robust geopolymeric gel structure [9, 15], transitioning it into a denser, consolidated configuration [12]. Additionally, it's noteworthy that at 150°C, a curing pressure of 20 MPa proves particularly beneficial for the microstructure, as evidenced in Figure 4.23(a), and for porosity reduction (refer to Table 4.4). The observed decrease in porosity is further supported by the findings from mercury intrusion porosimetry (MIP), as depicted in Figure 4.17 and Table 4.4.

The investigation of curing under simultaneous pressure and temperature revealed a balance influence of these parameters on the resulting microstructure and compressive strength. The interplay between both factors hinges on their combined values, with pressure refining the microstructure for temperatures exceeding 100°C. Conversely, at temperatures below 100°C, pressure tends to elevate porosity while leaving compressive strength unaffected due to enhanced reactivity. This comprehensive analysis of combined temperature and pressure holds significance across various applications, oil-well cementing, brick production, high-tech ceramic sintering and industrial commercialization.

4.4. Conclusions

Curing geopolymers at room temperature (21°C) poses challenges, resulting in lower geopolymerization degrees and delayed setting, primarily due to difficulties in achieving gel homogenization. However, targeted thermal curing post-production effectively enhances geopolymerization.

Validation using the ultrasonic cement analyzer (UCA) confirms that thermal curing significantly reduces setting time and accelerates early-age strength development. This is attributed to intensified geopolymerization at higher curing

temperatures, facilitated by increased metakaolin dissolution and reaction kinetics. Nonetheless, temperatures exceeding 100°C lead to early dehydration and volumetric contraction-induced crack formation.

Curing pressure plays a crucial role in material reorganization; pressures equal to or exceeding 40 MPa hinder compaction, while 20 MPa promotes microstructural compaction, contributing to improved mechanical properties.

Elevated temperatures coupled with pressure enhance geopolymerization kinetics, resulting in microstructural densification. However, caution is warranted at temperatures above 100°C, as rapid water evaporation induces crack formation within hours.

Mercury intrusion porosimetry (MIP) reveals a narrower pore size distribution at temperatures up to 90°C, with increased pore size values at higher temperatures due to intensified water evaporation. High-pressure curing refines macropores to micropores below 20 nm, optimizing porosity and compressive strength.

The combined effect of pressure and temperature accelerates reaction product formation and microstructural compaction. Optimal conditions, observed at 50°C and 20 MPa for at least one day, enhance mechanical and morphological features, improving compressive strength by 177% compared to room temperature at atmospheric pressure.

Overall, this study significantly advances knowledge on pressurized thermal curing for rapidly setting geopolymers, offering diverse mechanical properties for various applications. Future research should explore reinforcements to enhance mechanical properties under extreme temperature and pressure conditions.

4.5. References

1. Davidovits, R., Pelegris, C., Davidovits, J. (2019), Standardized Method in Testing Commercial Metakaolins for Geopolymer Formulations, Technical Paper#26-MK-testing, Geopolymer Institute Library, www.geopolymer.org.
2. Trindade, A. C. C., Silva, F. A., Alcamandb, H. A., Borges, P. H. R. (2017). On The Mechanical Behavior of Metakaolin Based Geopolymers Under Elevated Temperatures. *Materials Research*, 20(Suppl. 2): 265-272.
3. Lee, N. K., Lee, H. K. (2015). Reactivity and reaction products of alkali-activated, fly ash/slag paste. *Construction and Building Materials*, 81, 303–312.

4. Davidovits, J. (2018), Why Alkali-Activated Materials (AAM) are Not Geopolymers, Technical Paper #25, Geopolymer Institute Library, www.geopolymer.org.
5. Shekhovtsova, J., Kearsley, E. P., Kovtun, M. (2015). Evaluation of short- and longterm properties of heat-cured alkali-activated fly ash concrete. *Magazine of Concrete Research*, 67(16), 897–905.
6. Zhao, J., Liebscher, M., Michel, A., Junger, D., Trindade, A.C.C., Silva, F.A., Mechtcherine, V. (2021)._Development and testing of fast curing, mineral-impregnated carbon fiber (MCF) reinforcements based on metakaolin-made geopolymers._*Cement and Concrete Composites*, 116.
7. Samantasinghar, S., Singh, S. (2020). Effects of curing environment on strength and microstructure of alkali-activated fly ash-slag binder. *Construction and Building Materials*, 235.
8. Singh, G. V. P. B., Subramaniam, K. V. L. (2019). Influence of processing temperature on the reaction product and strength gain in alkali-activated fly ash. *Cement and Concrete Composites*, 95, 10–18.
9. Ai, T., Zhong, D., Zhang, Y., Zong, J., Yan, X., Niu, Y. (2021). The Effect of Red Mud Content on the Compressive Strength of Geopolymers under Different Curing Systems. *Buildings*, 11, 298.
10. Ahmad, M., Rashid, K., Hameed, R., Haq, E. U., Farooq, H., Ju, M. (2022). Physico-mechanical performance of fly ash based geopolymer brick: Influence of pressure – temperature – time. *Journal of Building Engineering*, 50.
11. Ling, Y., Wang, K., Wang, X., Hua, S. (2019). Effects of mix design parameters on heat of geopolymerization, set time, and compressive strength of high calcium fly ash geopolymer. *Construction and Building Materials*, 228.
12. Bai, Y., Guo, W., Wang, J., Xu, Z., Wang, S., Zhao, Q., Zhou, J. (2022). Geopolymer bricks prepared by MSWI fly ash and other solid wastes: Moulding pressure and curing method optimization. *Chemosphere*, 307.
13. Kajarathan, S., Karthikan, S., Nasvi, M.C.M. (2015). Geopolymer as Well Cement and its Mechanical Behaviour with Curing Temperature. In *Proceedings of the 6th International Conference on Structural Engineering and Construction Management 2015*, Kandy, Sri Lanka, 11–13 December 2015
14. Hoang, M.D., Do, Q.M., Le, V.Q. (2020). Effect of curing regime on properties of red mud-based alkali activated materials. *Construction and Building Materials*, 259.
15. Ranjbar, N., Kashefi, A., Ye, G., Mehrali, M. (2020). Effects of heat and pressure on hot-pressed geopolymer. *Construction and Building Materials*, 231.
16. Park, S.M., Khalid, H.R., Seo, J.H., Yoon, H.N., Son, H.M., Kim, S.H., Lee, N.K., Lee, H.K., Jang, J.G. (2018). Pressure-Induced Geopolymerization in Alkali-Activated Fly Ash. *Sustainability*, 10.

17. Debruijn, G., Skeates, C., Greenaway, R., Harrison, D., Parris, M., James, S., Mueller, F., Ray, S., Riding, M., Temple, L., Wutherich, K. (2008). High-Pressure, High-Temperature Technologies. *Oilfield Review*. pp. 46-60.
18. Liu, X., Nair, S.D., Aughenbaugh, K.L., Juenger, M.C.G., Oort, E. (2020). Improving the rheological properties of alkali-activated geopolymers using non-aqueous fluids for well cementing and lost circulation control purposes. *Journal of Petroleum Science and Engineering*, 195.
19. Salehi, S., Khattak, M. J., Rizvi, H., Karbalaeei, S. F., Kiran, R. (2017). Sensitivity analysis of fly ash geopolymer cement slurries: Implications for oil and gas wells cementing applications. *Journal of Natural Gas Science and Engineering* 37. Pp. 16-125.
20. Kamali, M., Khalifeh, M., Saasen, A., Godøy, R., Delabroy, L. (2021). Alternative setting materials for primary cementing and zonal isolation – Laboratory evaluation of rheological and mechanical Properties. *Journal of Petroleum Science and Engineering*, 201.
21. Giasuddin, H. M., Sanjayan, J. G., Ranjith, P. G. (2013). Strength of geopolymer cured in saline water in ambient conditions. *Fuel* n. 107. pp. 34–39.
22. Nasvi, M., Gamage, R. P., Jay, S. (2012). Geopolymer as well cement and the variation of its mechanical behavior with curing temperature. *Greenhouse gases: science and technology*. 2(1): 46-58.
23. Khalifeh, M., Saasen, A., Hodne, H., Godøy, R., Vra°lstad, T. (2018). Geopolymers as an Alternative for Oil Well Cementing Applications: A Review of Advantages and Concerns. *Journal of Energy Resources Technology*. Vol. 140.
24. Ridha, S., Abd Hamid, A. I., Abdul Halim, A. H., Zamzuri, N. A. (2018) Elasticity and expansion test performance of geopolymer as oil well cement. *ICOnCEES 2017. IOP Conf. Series: Earth and Environmental Science* 140. pp. 1-6.
25. Feng, Q., Jia, F., Peng, Z., Zheng, Y. (2022). Preparation, characterization, and evaluation of suspension stabilizer for low-density cement slurry for cementing. *J Appl Polym Sci*. 139.
26. Yue, J., Liu, Z., Wang, J., Sun, T., Wu, Z., Geng, Y. (2020). A Low-Cost and Low-Density Cement Slurry System Suitable for a Shallow Unconsolidated Stratum. *Advances in Materials Science and Engineering*, Vol. 2020.
27. Brandvold, A.S., Trindade, A.C.C., Kriven, W.M. (2023). Rheological assessment of metakaolin-based geopolymer composites through squeeze flow. *Journal of the American Ceramic Society*. pp. 4038-4051.
28. Brandvold, A.S., Al-Chaar, G.K., Kriven, W.M. (2023). Isolating the effects of thixotropy in geopolymer pastes. *Journal of the American Ceramic Society*. pp. 2797-2807.
29. ASTM C618-22, *Standard Specification for Coal Fly Ash and Raw or Calcined Natural Pozzolan for Use in Concrete*.
30. Siciliano, U.C.C.S., Trindade, A.C.C., Silva, F.A. Potassium-waterglass (K-WG) Influence on Geopolymer Strength Development & Leaching in

- Different Curing Environments. Submitted to **Journal of Building Engineering** on August 08, 2023.
31. Saludung, A., Azeyanagi, T., Ogawa, Y., Kawai, K. (2021). Alkali leaching and mechanical performance of epoxy resin-reinforced geopolymer composite. *Materials Letters*, 304.
 32. Ameri, F., Shoaiei, P., Zareei, S.A., Behforouz, B. (2019). Geopolymers vs. alkali-activated materials (AAMs): A comparative study on durability, microstructure, and resistance to elevated temperatures of lightweight mortars. *Construction and Building Materials* 222. 49–63.
 33. Kolousek, D., Brus, J., Urbanova, M., Andertova, J., Hulinsky, V., Vorel, J. (2007). Preparation, structure and hydrothermal stability of alternative (sodium silicate-free) geopolymers. *J Mater Sci* 42. 9267–9275.
 34. John, S.K., Nadir, Y., Cascardi, A., Arif, M.M., Girija, K. (2023). Effect of addition of nanoclay and SBR latex on fly ash-slag geopolymer mortar. *Journal of Building Engineering* 66.
 35. Bu, Y., Song, W., Wang, M., He, Y. (2011). The improvement of cementation quality rating method based on compressive strength for low density cement system. *Procedia Engineering* 18 (2011) 289 – 294.
 36. Wang, R., Qin, L., Gao, X. (2020). Mechanical strength and water resistance of magnesium oxysulfate cement based lightweight materials. *Cement and Concrete Composites*, 109.
 37. Khalifeh, M; Saasen, A; Vralstad, T; Hodne, H. (2014). Potential utilization of class C fly ash-based geopolymer in oil well cementing operations. *Cement & Concrete Composites* n. 53. pp. 10–17.
 38. Alvi, M. A. A; Khalifeh, M; Agonafir, M. B. (2020). Effect of nanoparticles on properties of geopolymers designed for well cementing applications. *Journal of Petroleum Science and Engineering* 191. pp. 107-128.
 39. Junaid, M.T., Kayalli, O. (2017). Response of alkali activated low calcium fly-ash based geopolymer concrete under compressive load at elevated temperatures. *Materials and Structures*. 50:50.
 40. Lizcano, M., Kim, H. S., Basu, S., Radovic, M. (2012). Mechanical properties of sodium and potassium activated metakaolin-based geopolymers. *J Mater Sci*, 47, 2607–2616.
 41. Liang, G., Yao, W., She, A. (2023). New insights into the early-age reaction kinetics of metakaolin geopolymer by ¹H low-field NMR and isothermal calorimetry. *Cement and Concrete Composites*, 137.
 42. Nishikawa, K., Yamaguchi, K., Suzuki, T., Hashimoto, S., Rossignol, S. (2022). Effect of amorphous silica fume as active filler for rapid densification of the geopolymer products formed by warm pressing. *Ceramics International*, 48.
 43. Kohout, J., Koutník, P., Hájková, P., Kohoutová, E., Soukup, A. (2022). Effect of Different Types of Aluminosilicates on the Thermo-Mechanical Properties of Metakaolinite-Based Geopolymer Composites. *Polymers* 2022, 14, 4838.

44. Kamseu, E., Rizzuti, A., Leonelli, C., Perera, D. (2010). Enhanced thermal stability in K₂O-metakaolin-based geopolymer concretes by Al₂O₃ and SiO₂ fillers addition. *J Mater Sci* 45. 1715–1724.
45. Rovnanik, P., Safrankova, K. (2016). Thermal Behaviour of Metakaolin/Fly Ash Geopolymers with Chamotte Aggregate. *Materials* 2016, 9, 535.
46. Ukrainczyk, N. (2021). Simple Model for Alkali Leaching from Geopolymers: Effects of Raw Materials and Acetic Acid Concentration on Apparent Diffusion Coefficient. *Materials*, 14, 1425
47. Adjei, S., Elkatatny, S., Sarmah, P., Abdelfattah, A. M. (2021). Evaluation of calcined Saudi calcium bentonite as cement replacement in low-density oil-well cement system. *Journal of Petroleum Science and Engineering*, 205.
48. Kani, E.N., Allahverdi, A. (2009). Effects of curing time and temperature on strength development of inorganic polymeric binder based on natural pozzolan. *J Mater Sci*, 44:3088–3097.
49. Smeets, S., Xie, D., Baerlocher, C., McCusker, L.B., Wan, W., Zou, X., Zones, S.I. (2014). High-Silica Zeolite SSZ-61 with Dumbbell-Shaped Extra-Large-Pore Channels. *Angew. Chem. Int. Ed.*, 53, 10398 –10402

5. Optimizing high-temperature and pressure performance of metakaolin-based geopolymers through the inclusion of hybrid particulate reinforcements

5.1. Introduction

Geopolymer (GP) is an inorganic polymeric material composed of alumina, silica and alkali metal oxides [1]. Geopolymerization is a chemical process involving dissolved silicates and aluminates in a highly alkali medium. Dehydration, dehydroxylation, densification and plastic deformation are induced by alkali ions [2]. Metakaolin-based geopolymers (MK-GP) often require an alkali solution made with high water content to achieve suitable rheology, leading to excessive cracking and drying shrinkage [3]. Water serves as a transport medium, without participating in the reaction, as opposed to the hydration mechanisms of Portland cement [4-6]. The alkali solution governs both the dissolution and polycondensation stages, affecting crosslinking and strength development [2]. Resulting products typically possess predominantly amorphous 3D structures with partially ordered fractions [7]. The degree of crystallization depends on achieving thermodynamic balance [5] and precursor reactivity.

Optimal geopolymer designs include strong Si-O-Si bonds [8], suitable composition related to $\text{SiO}_2:\text{Al}_2\text{O}_3$ ratios [9,10], adequate particle size distribution and correct alkali choice [9]. Systems with finer particles commonly lead to higher compressive strength [5]. Fracture energy and peak load capacities are enhanced with increasing alkali concentration [11]. Potassium-based alkali solutions offer improved thermal stability [7, 12], compared to sodium-based systems, lower shrinkage (approx. around 20%), [13] and more uniform nanosized pore distribution due to their extended dissolution [14].

Geopolymers, considered substitutes for Portland cement (PC), offer advantages like rapid strength gain, low shrinkage, long-term, thermal and high freeze-thaw durability [15]. They excel in thermal scenarios up to 1100°C [2, 16],

making them well-suited for applications as refractory coatings and thermal barriers. However, at intermediate temperatures, particularly between 90°C and 200°C [17, 18], a significant strength decline is observed due to rapid dehydration [17], resulting in an expansion of macropores [19]. Furthermore, higher temperatures can widen pre-existing cracks [20].

Prior research indicates that consistent strength development is achievable by employing curing temperatures coupled with pressures, promoting polycondensation and microstructure enhancement [21]. Additionally, a more extensive array of reaction products is obtained after a 4 h autoclave curing period [22].

Plain geopolymers persist as brittle materials when cured at high temperatures, being susceptible to dehydration cracking. Therefore, it is essential to add a reinforcing phase to improve strength, toughness and maintain structural integrity under elevated temperatures [1]. A newly developed geopolymer paste, incorporating alpha-quartz sand and fine alumina powder, demonstrated superior performance, with Al-rich GP outperforming sand-rich variants [2]. Notably the addition of sand alone supported temperatures up to 110°C without encountering cracking issues [3]. Mullite-based particulates, such as chamotte [1], have proven effective due to excellent stability in alkali environments at high temperatures [16], resulting in minimal shrinkage and excellent mechanical properties [18]. In MK-GP, the inclusion of sand with particle size less than 76 μm increased compactness, reducing drying shrinkage and reaching greater compressive strength [8]. Thus, smaller particles contribute to a more compact structure and improve the interfacial transition zone (ITZ) [6]. For highly alkali geopolymers, there is a potential chemical effect, forming more Si-O-Si bonds through the superficial adhesion with mullite-based aggregates [8].

The use of raw materials with varying reactivities also offers a promising alternative for optimizing the properties of GP [9]. Nanosized aluminosilicate sources owing to their elevated surface area to volume ratio, ensured high chemical reactivity [23-25]. This contributed to the microstructure densification, resulting in increased compressive strength at early ages [23, 25-27] as a consequence of a faster setting [25]. The implications extend to the control of rheological properties [24], with potential gains in terms of toughness and elastic modulus [23, 24].

Nevertheless, there is an optimal concentration of nanoparticles (nanoclay,

nano-metakaolin and carbon nanotubes) that yields the maximum improvement in mechanical properties [8, 10, 12, 15, 21, 23-25, 28-35]. The inclusion of nanoparticles also reduces the permeability of the GP [12, 23, 25, 30, 31]. However, it is crucial to note that concentrations above the optimum value can lead to a decline in the aforementioned properties. The increase in tensile and flexural strengths may be attributed to the enhanced bonding in the ITZ between the GP paste and particles, facilitated by the addition of nanoclay [12, 34].

Nanoclay plays a dual role as both filler and binder, facilitating the geopolymerization reactions [23, 31]. Its inclusion enhances durability, thermal properties [12, 23, 25], ensuring superior strength at elevated temperatures [23, 31] as a result of the increased degree of geopolymerization and the formation of more dimensionally stable products [12]. At optimal levels, nanoclay acts as a catalyst, accelerating geopolymerization even under ambient curing conditions (22°C) [36]. Coated nanoclay strategically extends setting times, counteracting viscosity increases with thixotropic behavior [37]. However, excessive nanoclay disrupts the material properties, causing agglomeration, self-desiccation and cracking [28]. This hinders chemical reactions and weakens the bonds between reinforcement particles and matrix, affecting workability [23]. Balancing nanoclay addition is crucial to maximize benefits without compromising overall material performance.

The incorporation of multi-walled carbon nanotubes (MWCNTs) into GPs enhances structural properties [15] by exploiting the intrinsic strength and fibrous morphology of MWCNTs [10, 32, 34, 35]. This leads to a notable crack-bridging effect, particularly evident with 1.5 %wt. CNTs [38], improving load transfer, strength and stiffness. Despite inducing stress concentrations [15, 25, 33, 35, 38], CNTs also serve as fillers, linking GP pores and altering the microstructure [30, 34, 38, 39], reducing drying shrinkage and water absorption [30]. Beyond mechanical benefits, CNTs enable structural functionalization [39], increasing electrical conductivity [15, 23, 25, 32, 35]. The hydroxylation of Si atoms in K-GP contributes to microstructural densification, with 0.6 and 1.5 %wt. CNTs affecting chemical bonds [38]. CNTs delay setting time, since they influence rheological properties [38, 39], with up to 0.2 %wt. showing no discernible impact [38], 0.3 %wt. reducing plastic viscosity [33, 38], and concentrations above 0.6 %wt. increasing plastic viscosity [38]. However, achieving uniform dispersion of CNTs poses a major challenge [10, 25, 34] due to their high hydrophobicity and self-

attraction [25], exacerbated at high concentrations [10, 25, 33, 38]. The methodology chosen by Rocha and Ludvig [35], including the use of absolute ethanol or surfactants, affects dispersion quality [10, 25], introducing challenges such as persistent clusters and air bubbles formation. Surface treatment of CNTs with negatively charged groups proves promising for improved dispersion and matrix compatibility [25, 39]. Functionalization enhances dispersion, especially for additions up to 0.15 %wt. CNTs [25]. Achieving an effective dispersion method remains a challenge for optimizing the benefits of CNTs additions to GP.

To meet the demand for high-tech concrete applications without increasing binder content, the incorporation of nanomaterials, particularly CNTs, has emerged as a viable alternative [23]. The enhanced conductivity allows concrete to absorb electromagnetic waves, presenting possibilities for electromagnetic shielding infrastructures [25, 39]. The heightened piezoresistive response enables effective monitoring of crack propagation [15, 24]. Moreover, CNT-based nanocomposites exhibit promising thermoelectric properties, capable of storing energy when exposed to temperature gradients [32]. In addition to elevating structural performance, CNT-based concretes exhibit excellent durability, withstanding harsh environments and various types of stresses [24]. Expanding applications, the addition of CNTs to K-GP holds potential for innovative uses in 3D printing, due to plastic viscosity changes [38]. Simultaneously, the incorporation of nanoclay in GP shows promise for repair materials, fiber-reinforced composites [12], and gas barriers [23]. GP filled with chamotte lead to low shrinkage [40] (less than 1 % up to 1200°C [41]), high heat resistance [40, 41] and excellent mechanics properties [40, 42]. They also find potential application in oil well plugging, maintaining workability for up to 2 h at temperatures reaching 150°C, crucial for their use in challenging conditions. Overall, these advanced materials demonstrate versatility and innovation in addressing diverse construction challenges.

This study aims to improve the performance of K-GP at elevated temperatures and pressures by adding micrometric and nanometric reinforcements, thereby mitigating extreme conditions induced cracks. Enhanced microstructural stability is pivotal for broadening the material's application. The exploration of nanoparticle-modified GPs and the novel application of hybrid reinforcements in K-GP for superior quality represent uncharted territories in the current literature. Prioritizing mechanical properties is foundational, considering that this is the

primary factor dictating field application feasibility. Innovatively, early-age curing under pressure and temperature serves as predictive measure for long-term properties, allowing for the induction and acceleration of structural changes. Notably, the dispersion of MWCNTs adopts an efficient approach, utilizing functionalization and dispersion in an alkali solution. This method ensures dispersion without relying on surfactants or sonication, reducing binder consumption and simplifying in-situ production processes. This research pioneers a holistic approach to enhancing microstructural stability of K-GP under extreme environmental conditions by adding hybrid reinforcements that act simultaneously to prevent damages.

5.2. Experimental Program

5.2.1. Materials and Alkaline Solution Preparation

Even with the incorporation of reinforcements, achieving an optimal GP paste/filler ratio is crucial to keep control over the final mechanical properties. For this reason, the GP plain formulation was selected based on the findings of a previous study [43]. The K-based alkali solution was composed with molar ratios of $\text{SiO}_2:\text{K}_2\text{O}=1.53$ and $\text{H}_2\text{O}:\text{K}_2\text{O}=8.69$. Plain geopolymers were designed with $\text{SiO}_2:\text{Al}_2\text{O}_3=4$. The potassium silicate solution was prepared by (1) dissolving potassium hydroxide (PROQUIMIOS, 88.9% purity, in the form of lentils) in deionized water; (2) gradually adding hydrophilic silica fume (AEROSIL – Evonik); (3) further mixing the components on a magnetic stirrer for 24 h. Following mixing, the solution rested for an additional 24 hours before use.

For micrometric particulate reinforcement, a non-reactive material compatible with the GP constituents was chosen to avoid compromising the degree of geopolymerization and to withstand the high alkalinity of the paste. To this end, Chamotte70 (TOGNI S/A) was selected, possessing an extremely low coefficient of thermal expansion, making it suitable for high-temperature applications [1]. The addition of 20 %wt. was chosen based on Trindade *et al.* [44], indicating that this percentage facilitates does not affect so significantly the rheology of the paste. However, incorporating a material with appropriate particle size distribution is essential for optimizing the final properties of the GP.

According to the Chamotte70 supplier, the particles are less than 0.59 mm. Nevertheless, an analysis of the granulometry of this material obtained by Laser Diffraction Particle Size Analyzer - LDPSA (Figure 5.1(b)) revealed that the mean diameter of the particles (d_{50}) significantly differed from that of metakaolin (Figure 5.1(a)). Consequently, Chamotte70 underwent a grinding process in a bar mill for 5 minutes. The resulting change in the particle size distribution curve is evident (Figure 5.1(b)), as accompanied by a lighter color of the material (Figure 5.2). The surface area of Chamotte70 increased from $0.0798 \text{ m}^2/\text{g}$ to $0.798 \text{ m}^2/\text{g}$ (obtained by LDPSA), and the d_{50} varied from 248.8 to $36.6 \mu\text{m}$, with the size now falling within the range of 0.3 to $158.5 \mu\text{m}$.

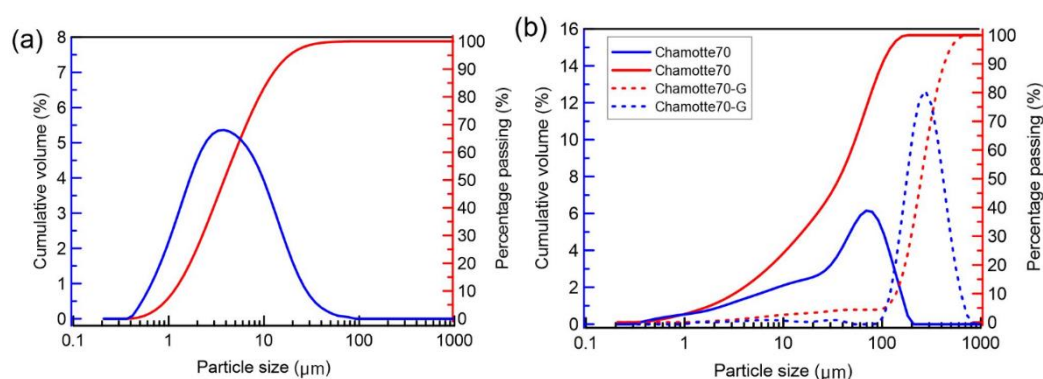


Figure 5.1 – Particle size distribution for (a) Metakaolin and (b) Chamotte70 (before and after grinding).

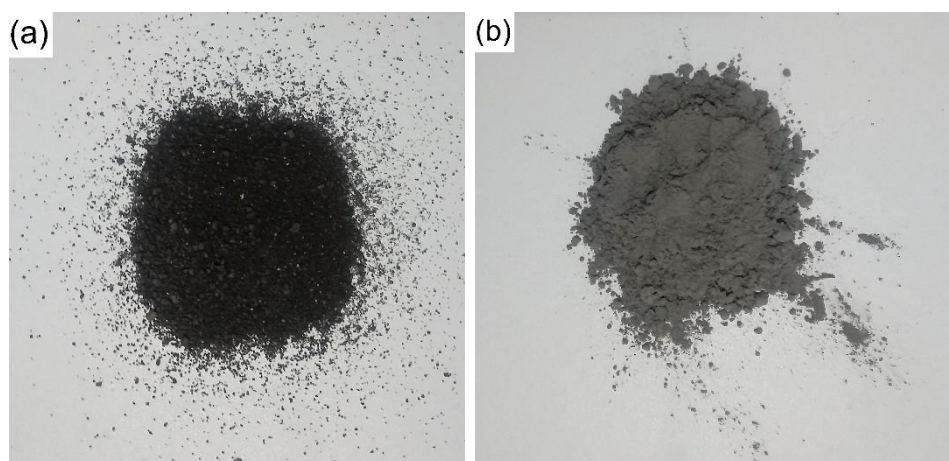


Figure 5.2 – Visual comparison: (a) Chamotte70 in its original state as supplied, and (b) after the grinding process.

In light of the color change following the grinding process, X-ray Diffraction (XRD) analysis was performed on both the Chamotte70 sample and the resulting ground material (referred to as Chamotte70-G). This analysis aimed to

discern any potential shifts in the crystalline structure (Figure 5.3). Additionally, the chemical composition was assessed by X-ray Fluorescence (XRF), with the results presented in Table 5.1.

Table 5.1 – Composition of raw materials determined by X-ray fluorescence (XRF), expressed in weight percentages (%wt.).

Material	Al ₂ O ₃	SiO ₂	TiO ₂	Fe ₂ O ₃	K ₂ O	SO ₃	CaO	Others
Metakaolin	50.02	48.28	1.11	0.355	0.109	0.055	0.026	0.045
Silica fume	-	99.992	-	0.005	-	-	-	0.003
Chamotte70	76.598	17.131	4.694	1.262	-	-	-	0.315
Chamotte70-G	77.373	16.853	4.192	1.266	-	-	0.038	0.28
Nanoclay	48.356	50.666	0.031	0.463	-	0.068	0.171	0.245
Nanoclay-C	49.483	49.659	0.035	0.442	-	0.048	0.164	0.17

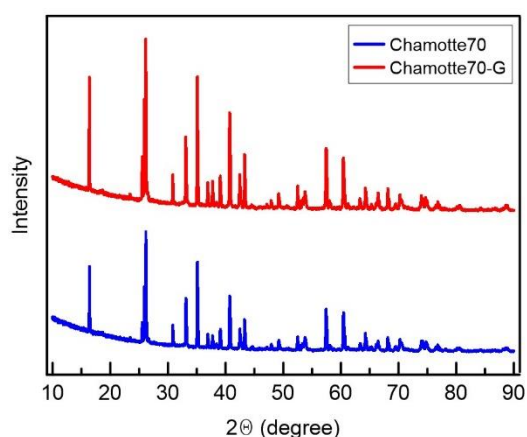


Figure 5.3 – XRD pattern for Chamotte70 as supplied and after grinding (Chamotte70-G).

As depicted in Figure 5.3, the crystalline structure of Chamotte-70 remained unaltered, and there were only slightly changes in the chemical composition (Table 5.1). Table 5.2 provides an overview of the phases present in the both types of Chamotte70.

Table 5.2 – Mass distribution and lattice parameters of crystalline phases obtained by XRD analysis for Chamotte70 and Chamotte70-G.

Sample	% Mass			Crystallite Size (LVol IB) /nm				
	C	M	F	C	M	F		
Chamotte70	18.6	77.1	4.3	714	383	16		
Chamotte70-G	21.3	73.9	4.8	482	304	16		
Sample	Lattice Parameters / Å							
	C		M			F		
Sample	a	c	a	b	c	a	b	c
Chamotte70	4.76	13.00	7.58	7.70	2.89	3.58	9.59	9.81
Chamotte70-G	4.76	13.00	7.58	7.70	2.89	3.59	9.54	9.79

C- corundum (Al_2O_3 , ICSD 9770), M – mullite ($\text{Al}_{5.33}\text{Si}_{0.67}\text{O}_{9.33}$, ICSD 66448), F (FeAlTiO_5 , ICSD 35243.)

The identified crystalline phases include corundum, mullite and FeAlTiO_5 . Additionally, there is a potential presence of approximately 1 to 2 %wt. of hematite (Fe_2O_3), which XRD could not confirm as its peaks are superposed with peaks of the other phases. The grinding procedure changed the lattice parameters of the three constitutive phases beyond the experimental errors. The grinding procedure may have changed the composition (Table 5.1) and lattice distortions. Replacing part of the metakaolin with nano-metakaolin (NMK) was also considered. For this, nanoclay (halloysite nanoclay, from Sigma-Aldrich) was used and a temperature of 750°C was deemed optimal to obtain maximum reactivity of the nano-halloysite, as proposed by Abdalla *et al.* [23]. The material underwent calcination in a muffle furnace with a heating rate of $18^\circ\text{C}/\text{min}$. Upon reaching the target temperature, the material was held for 2 hours and allowed to cool inside the oven until thermal equilibrium with the environment (25°C). This process resulted in a subtle change in the material's color, as shown in Figure 5.4.



Figure 5.4 – Visual contrast: (a) nanoclay in its original state as supplied, and (b) nanoclay after heating at 750°C for 2 hours.

XRD analysis was used (Figure 5.5) to assess whether the nanoclay became reactive in the alkaline solution, that is, whether there was amorphization.

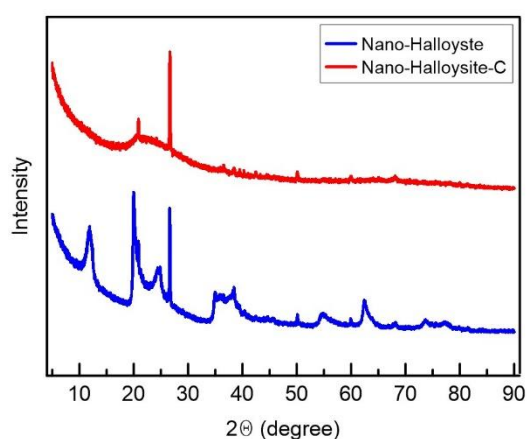


Figure 5.5 – XRD pattern for nanoclay in its original state as supplied and nanoclay after heating at 750°C for 2 hours.

As shown in Figure 5.5, the calcination of the nanoclay (now referred to as nanoclay-C) promotes amorphization, as evidenced by the broad hump in the X-ray diffraction pattern [24]. The amount of amorphous phase was 64.4 %, obtained by Rietveld analysis with alumina powder standard, indicating the destruction of part of the crystalline structure and the formation of an amorphous phase, giving rise to Nano-Metakaolin (NMK) [23]. These amorphous and crystalline content values, along with the composition of the nanoclay-C assessed by XRF (Table 5.1), was

used in the geopolymer design. Notably, the $\text{SiO}_2:\text{Al}_2\text{O}_3$ ratio in nanoclay-C is equal to 1.05, similar to the value for MK and therefore ideal for replacement. Table 5.3 presents the crystalline phases present in both the nanoclay and nanoclay-C.

Table 5.3 – Mass distribution of crystalline phases obtained by XRD analysis for nanoclay and nanoclay-C.

Sample	% Mass				Rwp
	H7A1	H7A2	Q	K	
Nanoclay	4.7	83.8	0.8	10.7	6.45
Nanoclay-C	-	-	24.0	76.0	4.68
Sample	Crystallite Size (LVol IB) /nm				GOF
	H7A1	H7A2	Q	K	
Nanoclay	26	6	99	25	1.91
Nanoclay-C	-	-	91	19	1.36

H7A1- Halloysite7A ($\text{Si}_2\text{Al}_2\text{O}_5(\text{OH})_4$, ICSD 26717), H7A2 - Halloysite7A ($\text{Si}_2\text{Al}_2\text{O}_5(\text{OH})_4$, ICSD 186723), Q – Quartz (SiO_2 , ICSD 16331), and K – Kaolinite ($\text{Al}_2\text{SiO}_5(\text{OH})_4$, ICSD 80082).

The physical properties of nanoclay, provided by the supplier, are given in Table 5.4.

Table 5.4 – Physical properties of the nanoclay provided by the manufacturer.

Relative density (g/cm^3)	Pore volume (ml/gm)	Diameter (nm)	Length (μm)	pH
2.53	1.26-1.34	30-70	1-3	4.5-7.0

It is worth noting that, as shown in Table 5.1, both particles (Chamotte70-G and nanoclay-C) exhibit elevated levels of SiO_2 and Al_2O_3 , suggesting their suitability in geopolymer mortars [27].

Multi-walled carbon nanotubes (MWCNT), supplied by NanoView, were also employed as reinforcements. Figure 5.6 displays microscopic images illustrating the tubular structures, a distinctive characteristic of MWCNT morphology.

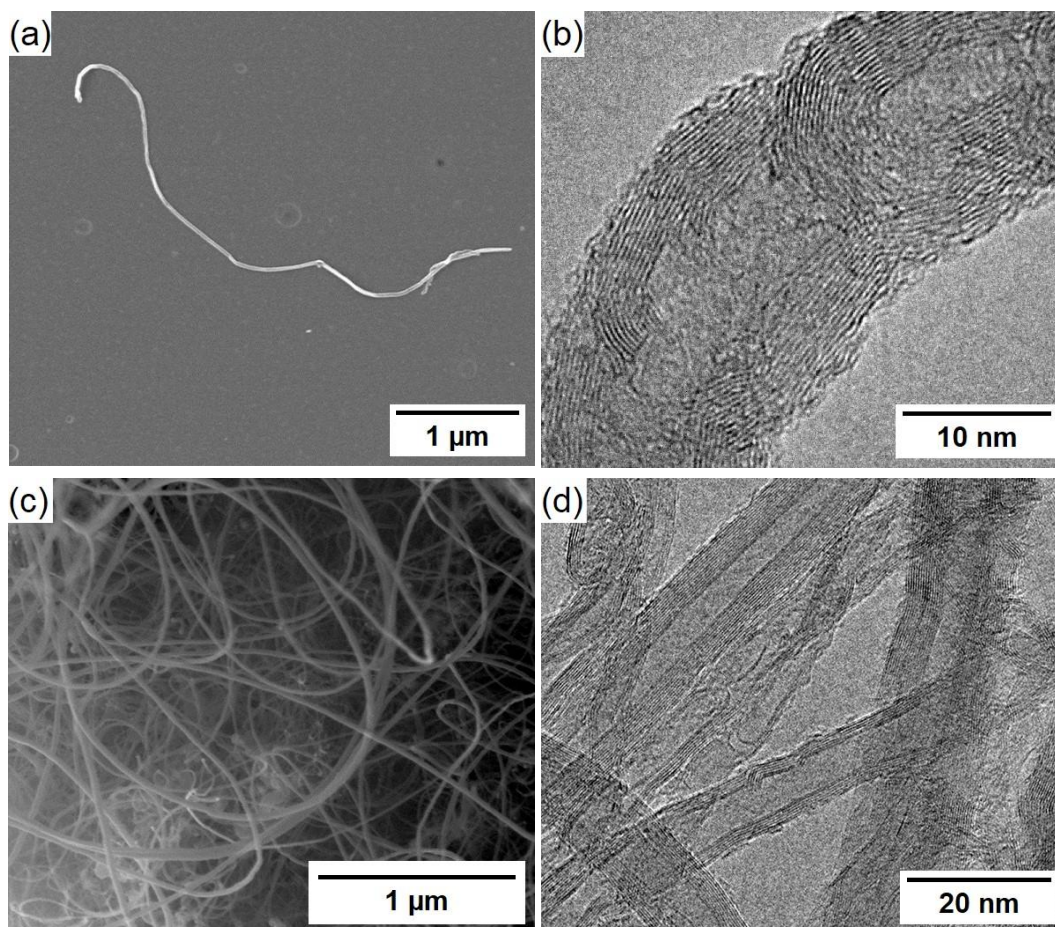


Figure 5.6 – Microscopic images provided by the manufacturer (NanoView), showing: (a) a singular functionalized MWCNT; (b) the multiple walls of MWCNTs within a single particle; (c) an ensemble of MWCNTs; and (d) the varied multiple walls of different MWCNTs.

MWCNTs underwent characterization through XRD (Figure 5.7). Notably, X-ray peaks are evident at diffraction angles (2θ) of 26° and 44.1° , corresponding to C(002) and C(100), the highly ordered graphitic structure of carbon atoms [38].

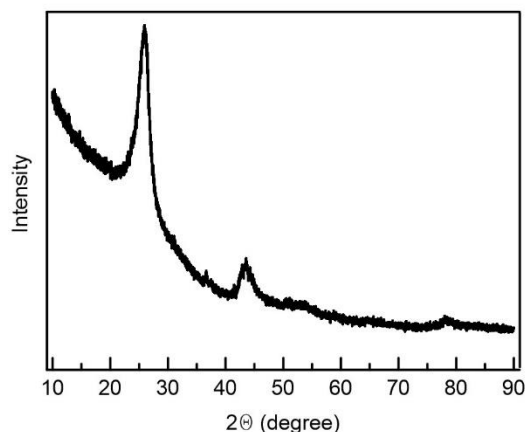


Figure 5.7 – X-ray diffraction (XRD) pattern of MWCNT.

The Physical, chemical and electrical characteristics of the MWCNT are presented in Tables 5.5 and 5.6.

Table 5.5 – Physical and chemical properties of the MWCNTs provided by the manufacturer.

Relative density (g/cm³)	1.4	Outer diameter (nm)	10-30	Purity (%)	> 95
Melting temperature (°C)	3652 - 3697	Length (um)	1-10	Degree of functionalization (%)	9-11
Electric conductivity (S/m)	> 100				

Table 5.6 – Chemical composition of MWCNT expressed in weight percentages (%wt.) provided by the manufacturer.

C	H	N	O	S	Co, Fe, Al₂O₃
81	0.8	0.3	11.6	0.7	5.6

5.2.2. Mix design and fresh properties

To achieve good MWCNT dispersion, the alkali solution was employed as the dispersing medium, as also proposed by Saafi *et al.* [15]. Once the MWCNTs in this work are functionalized type, no surfactant was added and a magnetic stirrer was utilized for process simplification. A quantity of 0.15 g of MWCNT was

dispersed in 1 kg of alkali solution and subjected to high-speed mixing for 72 hours. For comparison, non-functionalized MWCNTs (from Nanosyl) were placed in the alkali solution and sonicated (UP50H, Hielscher) for 5 minutes at 70% of the maximum power amplitude.

The dispersion of the MWCNTs was evaluated following two methods:

1. Optical Microscopy: a drop of the solution was placed between two glass plates for imaging. Image J software was used to binarize the image and evaluate cluster regions;
2. Multiple Light Scattering (MLS) technique: a dispersion analyzer (Turbiscan LAB) was used to quantify the stability of the MWCNT dispersion in the alkaline medium. Approximately 20 ml of the solution was placed in a cuvette and illuminated at 25°C for 60 min with near-infrared light ($\lambda=880$ nm), and the transmission and backscattering of light throughout the cell height were monitored.

The geopolymer formulations were manufactured using a highly reactive metakaolin (MK) powder (tradename MetaMax – BASF, Germany, specific density equal to 2.50 g/cm³, $d_{50}=1.3$ μm and pH=6) as the primary source of aluminosilicates. Various formulations were prepared, including plain samples (GP-0) and those with additional components: Chamotte70-G (GP-Cha), nanoclay-C (GP-NMK), MWCNTs (GP-CNT), and a hybrid formulation incorporating all three additions (GP-H).

Considering the chemical constituents of the alkali solution and those quantified for all source materials, along with the proportion of amorphous phase in nanoclay-C, the mixture design for the plain GP (GP-0) is outlined in Table 5.7.

Table 5.7 – Geopolymer design guided by the alkali solution/metakaolin mass ratio and the mass fraction of components, expressed in weight percentages (%wt.).

Alkali solution/Metakaolin mass ratio	Composition (%wt.)			
	KOH	SiO ₂	H ₂ O	Metakaolin (Al ₂ O ₃ . 2SiO ₂)
1.86	21.3	17.5	26.3	34.9

For GP-Cha, 20 %wt. of Chamotte70-G was added to the GP mass; for GP-NMK, 3 wt.% of nanoclay-C was incorporated into the GP mass, accounting for the reactive fraction (64.4% of nanoclay-C) as a substitute in the MK value; for GP-NTC, 0.015 %wt. of MWCNT was integrated into the GP mass; for GP-H, the three additions were considered in the same proportions as those used individually.

The mixing procedure consisted of mixing the components in an IKA 60 control mixer. Initially, the dry components were mixed at 1000 rpm for 1 minute, with the exception of nanoclay-C, which, due to its hydrophilic nature was first mixed in the alkali solution at 800 rpm for 3 minutes to ensure high dispersion. Subsequently, the dry components were added to the alkali solution and mixed at 1600 rpm for 3 minutes. Finally, the completion of the mix occurred at 2000 rpm for 2 minutes to ensure maximum homogeneity and reactivity. The paste was then vibrated at a frequency of 3 Hz for at least 10 minutes to eliminate any trapped air bubbles.

Flow table tests were carried out on both GP-0 and GP-H slurries to assess the influence of inclusions on shape retention, with the slump flow diameter recorded. A typical flow-table apparatus was used, equipped with a frustum of cone with dimensions of 40 mm in height, 64 mm in top diameter, and 74 mm in bottom diameter. To facilitate result presentation, flow workability was expressed in terms of the relative slump value (r_s) [12]:

$$r_s = \left(\frac{d}{d_0}\right)^2 - 1 \quad (5.1)$$

where d represents the average mortar flow diameter, and d_0 corresponds to the measure at the bottom diameter of the cone.

Flow measurements were further examined by using a 300 ml funnel with an orifice opening of 12 mm, enabling the measurement of flow time.

The setting time for all formulation was determined using the Vicat apparatus to evaluate the influence of each addition and its potential synergistic effects on the curing of geopolymers. Isothermal calorimetry was employed to estimate the geopolymerization process of each formulation and the heat of geopolymerization and heating rate were monitored using a Calmetrix model I-Cal HPC calorimeter over a period of 7 days at intervals of 1 minute. In order to ensure comparability among samples, a consistent paste weight of 50 g was maintained for

each composition.

5.2.3. Casting

For the uniaxial compression tests, samples were shaped into 10 mm cubes using silicone forms to evaluate the effect of each addition on the compressive strength of GP cured at 21°C and 150°C. Cubes with a side length of 50.8 mm, molded in metal molds coated with non-stick adhesive tape, were also prepared for the GP-0 and GP-H formulations.

For flexure tests, prisms measuring 40 x 40 mm² in cross section and 160 mm in length were cast. A notch with a depth of 10 mm ($a/d = 0.25$) and thickness of 2 mm was created by using a steel plate. This method was chosen to prevent crack formation, as cutting the notch after the specimen dried could lead to the development of defects. All surfaces contacted the slurry were pre-coated with non-stick adhesive tape.

5.2.4. Curing

Both the 10 mm cubes and the prismatic samples were cured for 1 day at 21°C, covered with plastic sheets to impede water loss. Additionally, curing was carried out at 150°C in an electric oven. The molds were covered with plastic foil and wrapped in a damp cloth to reduce moisture loss. The heating rate was 5°C/min, and upon reaching the target temperature, the specimens were kept in that temperature for 2 hours to ensure uniformity and sufficient exposure time. Subsequently, the samples were allowed to cool inside the oven until reaching thermal equilibrium with the environment.

The 50.8 mm cube samples were cured in an autoclave (Chandler, model 1910), undergoing various combinations of pressure and temperature: temperatures of 21°C and 150°C were employed with pressures of 0.1 MPa (atmospheric pressure) and 40 MPa, for 1 day, resulting in a total of four different temperature-pressure conditions. The molds were stacked and placed inside a metallic compartment filled with deionized water, subsequently inserted into the pressurizing oil-containing chamber. The equipment was calibrated to reach the target temperature in 4 hours, and the pressure was considered to hit instantly. Post-curing, the samples were allowed to cool down to room temperature before being

removed from the chamber, mitigating potential thermal shock.

All samples were further cured at 21°C and relative humidity of 55% for 28 days, to obtain reference values. To prevent early dehydration and cracking, these specimens were carefully wrapped with transparent acetate sheets.

5.2.5. Mechanical tests

For the 10 mm cubic samples, uniaxial compressive tests were carried out on an INSTRON EMIC 23-100 universal testing machine (max. load cell capacity: 100 kN), at a displacement rate of 0.1 mm/min. The compressive strength was calculated based on the average value obtained from four specimens.

The assessment of uniaxial compressive strength for the 50.8 mm cubic samples was carried out using a servo-hydraulic MTS 810/500 testing machine (max. load cell capacity: 500 kN) at a displacement rate of 0.5 mm/min. Compressive strength was calculated from the average value derived from three specimens.

3-point bending tests were carried out on the same servohydraulic MTS 810/500 testing machine, utilizing a load cell of 1 kN, at a displacement rate of 0.05 mm/min. The span between end supports was set at 150 mm, and the tests were controlled by Crack Mouth Opening Displacement (CMOD) using a clip gauge limited to 10 mm of opening attached to 1.5 mm thick wedge blocks. Flexural strength, reported as the average of values for 3 samples, was calculated using the Equation 5.2 [33]:

$$\sigma_f = \frac{3PS}{2b(w-a)^2} \quad (5.2)$$

where P is the maximum force applied, S is the distance between supports, b is the sample width, w is the sample height, a is the depth of the notch.

The critical crack length was considered equal to the depth of the notch, given the material's ideal brittle nature where the initiation of the crack immediately induces rupture [45]. The critical stress intensity factor (K_{IC}), also known as fracture toughness, was calculated according to the theory of linear elastic fracture mechanics, expressed by the formula [36]:

$$K_{IC} = \frac{3PS}{2bw^2} \cdot \sqrt{\pi a} \cdot f(a/w) \quad (5.3)$$

with:

$$f(a/w) = \frac{1.99 - \frac{a}{w} \left(1 - \frac{a}{w}\right) \left[2.15 - 3.93 \frac{a}{w} + 2.7 \left(\frac{a}{w}\right)^2\right]}{\left(1 + \frac{2a}{w}\right) \left(1 - \frac{a}{w}\right)^{3/2}} \quad (5.4)$$

The maximum load and the critical crack length equal to the notch depth were considered in the analysis.

5.2.6. Porosimetry

Pore size distribution analysis was conducted using the Mercury Intrusion Porosimetry (MIP) technique within the range of 0.003-100 μm . The measurements were performed on monolithic samples using a Porotec Porosimeter PASCAL 140/440 with a Mercury surface tension of 0.48 N/m with a contact angle of 140° and a test pressure between 0 to 400.71 MPa. To prepare the specimens for chemical analysis, they were exposed to isopropanol for seven days to fully remove free pore water and were subsequently dried out by solvent evaporation.

5.2.7. Thermal stability

Thermogravimetric analysis was conducted using a STA 409 cell device from Netzsch, Germany, under an oxygen atmosphere. The analysis was operated with a heating rate of 10°C/min, ranging from 20°C to 1000°C, using a 60 ml/min gaseous flow. Prior to the analysis, all specimens were exposed to isopropanol to remove free pore water and were subsequently dried out by solvent evaporation. Approximately 15 mg of ground geopolymer powder was used for each evaluation.

5.2.8. X-ray diffraction analysis

To evaluate possible phase changes due to the composition and the different curing regimes, X-ray powder diffraction (XRD) was performed in a D8 Discover diffractometer, Bruker AXS, with Bragg-Brentano geometry, copper tube, Ni filter, 40 kV accelerating tension, 40 mA filament current, 2 θ range 10° to 90°, step 0.02°, and acquisition time per step enough to reach 5000 counts. The samples were analyzed with the Fundamental Parameters Rietveld approach using the Topas 5.1, Bruker software.

5.2.9. Microscopic analyzes

The microstructure of the samples was observed using a Scanning Electron Microscope (SEM) model HITACHI-TM3000. The SEM allowed to observe the presence of pores, unreacted phases, and reacted microstructure variations. The analysis was carried out with a voltage of 15 kV. Fractured pieces of geopolymer cube from compressive strength tests were collected for the investigation.

5.3. Results and discussions

5.3.1. Carbon nanotube dispersion

As shown in Figures 5.8(a) and (b), functionalized MWCNTs demonstrated a smaller cluster size than non-functionalized MWCNTs. This enhanced dispersion is further evident in the cuvette cells (Figures 5.8(c) and (d)), where the alkali solution with containing functionalized MWCNTs exhibited better dispersion, characterized by a completely opaque appearance without visible clusters.

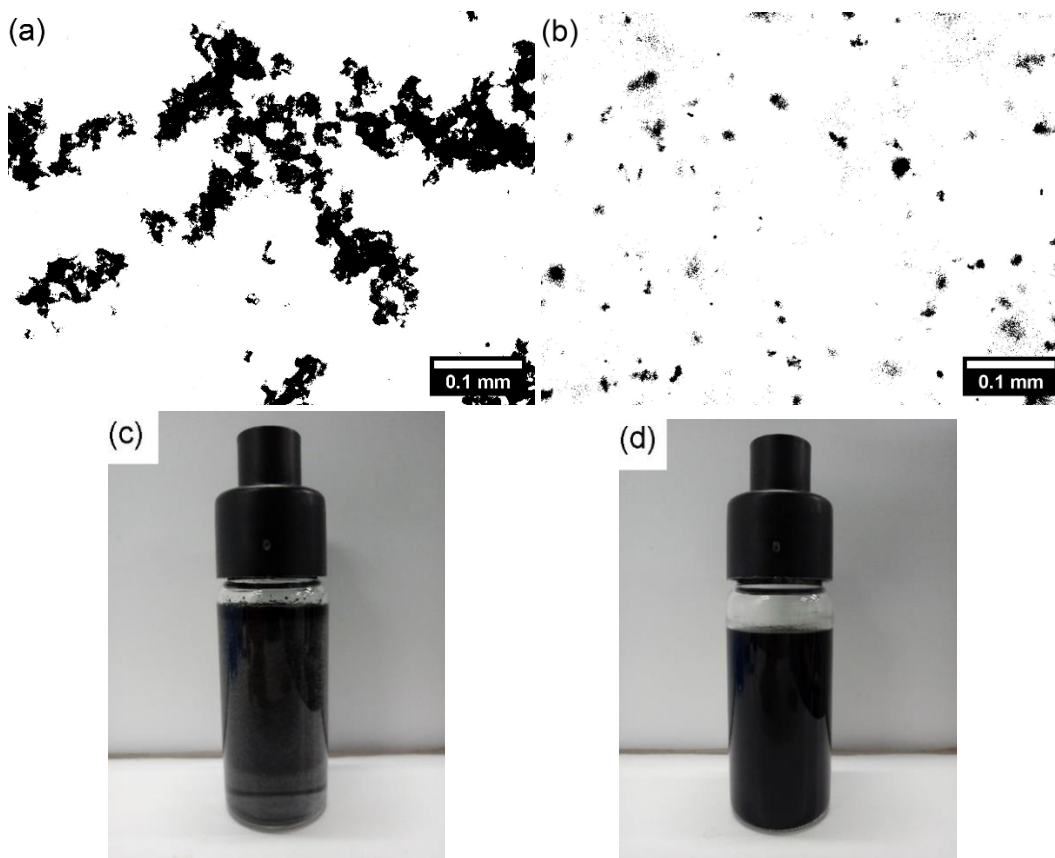


Figure 5.8 – Optical microscopy analysis of MWCNT clusters in alkali solution for (a) non-functionalized MWCNTs and (b) functionalized MWCNTs. MWCNTs dispersed in alkali solution considering: (c) non-functionalized MWCNTs and (d) functionalized MWCNTs.

A more effective approach to analyzing opaque solutions involves assessing backscattered light, as it provides insights into potential reagglomeration and sedimentation over time. Quantitative analysis, derived from the light transmission results, indicated that functionalized MWCNTs provided superior dispersibility and stability (Figures 5.9(a) and (b)) compared to non-functionalized MWCNTs (Figure 5.9(c) and (d)). A lower percentage of light transmission and a smaller variation over time are indicative of better dispersibility and greater stability, respectively. The reduced light transmission values for functionalized MWCNTs also signify increased opacity and a considerable presence of MWCNTs, emphasizing the high dispersibility [34]

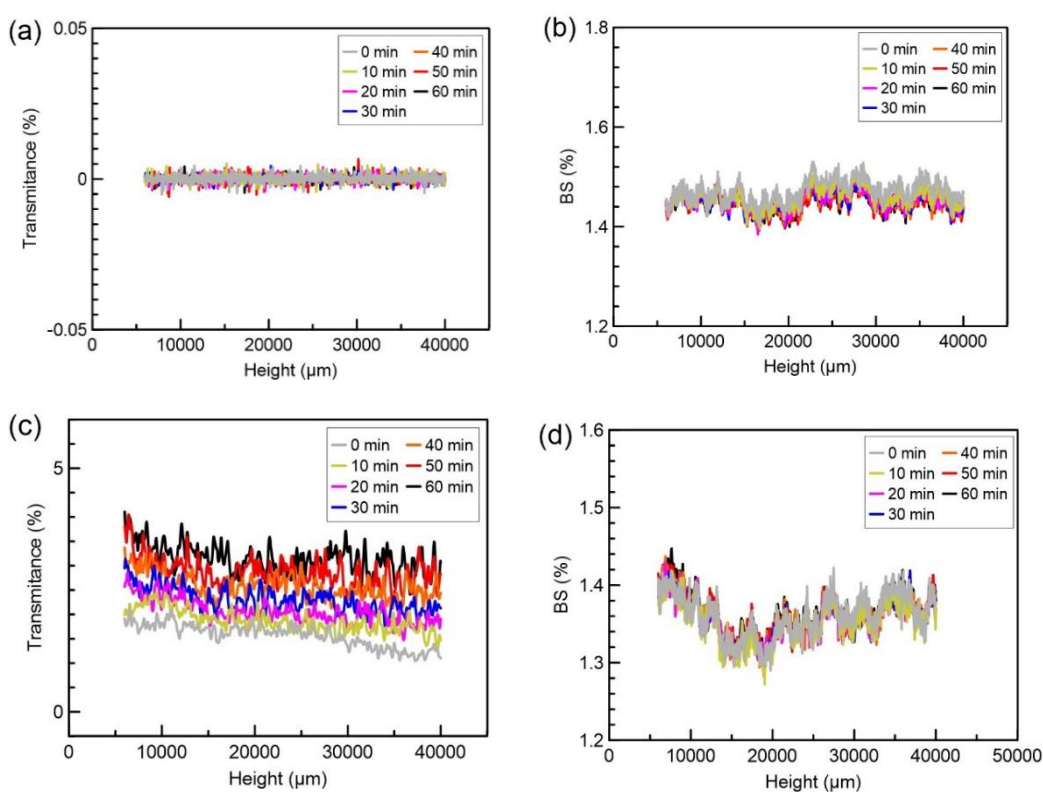


Figure 5.9 – MLS results for: functionalized MWCNTs dispersed in alkali solution: (a) transmitted light and (b) backscattered light; non-functionalized MWCNTs dispersed in alkali solution: (c) transmitted light and (d) backscattered light.

The stability of both types of solutions is evident from the consistent backscattered light readings over time, indicating that the solutions remain stable. This stability can be attributed to the viscosity of the alkali solution, which restrains the mobility of the nanoparticles, a mechanism known as viscous stabilization [34].

Thus, the dispersion of functionalized MWCNT in the alkali solution, achieved without the use of surfactant and sonication, has proven to be effective.

5.3.2. Fresh and transient-state properties

Table 5.8 presents the results of the flow table tests and fluidity time.

Table 5.8 – Fresh properties of the geopolymer (consistency and flowability).

	Slump flow diameter (cm)	Relative slump value (r_s)	Flowability (s)
GP-0	20.5	29.55	12.09
GP-H	17.5	4.59	25.89

The observed increase in mixture fluidity is attributed to the additions made to the paste. This phenomenon can be explained by the reduction in the total water fraction in the mixture resulting from an increase in the solid fraction [3]. This decrease reduces particle mobility, and the density differences between the additions and the binder further contribute [46]. Given that workability is associated with fluidity [40], the initial analysis suggests that GP-0 is more workable than GP-H. Setting time, closely linked to workability, was also considered. The Vicat test results and the key values are presented in Figure 5.10 and Table 5.9, respectively.

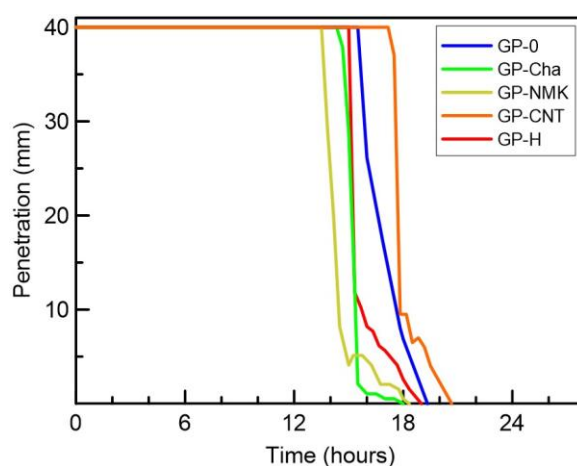


Figure 5.10 – Vicat test at room temperature (21°C) for plain geopolymer (GP-0) and geopolymer with: chamotte (GP-Cha), nano-metakaolin (GP-NMK), carbon nanotubes (GP-CNT) and all these additions together (GP-H).

Table 5.9 – Setting times determined from the curves obtained by the Vicat test for plain geopolymer (GP-0) and geopolymer with: chamotte (GP-Cha), nano-metakaolin (GP-NMK), carbon nanotubes (GP-CNT) and all these additions together (GP-H).

	Initial setting	Final setting
GP-0	18 h 30 min	19 h 10 min
GP-Cha	16 h 30 min	17 h 00 min
GP-NMK	16 h 00 min	18 h 00 min
GP-CNT	19 h 20 min	20 h 30 min
GP-H	17 h 20 min	18 h 40 min

The initial setting time for GP-0 aligns with the value reported by Brandvold *et al.* [42]. However, the final setting time was approximately 6 hours shorter, attributed to the reduced water amount used to prepare the solution that the GP-0 formulation was based off. GP-CNT exhibited a further longer final setting time, indicating that MWCNTs extend the workable period, an advantageous trait for high temperature applications. The inclusion of nanoclay reduced the setting time, possibly linked to accelerated geopolymerization kinetics [12]. Discrepancies among formulation may arise from differences in reactivity, size, shape, and chemical composition of each addition, influencing or not the geopolymerization process [18]. The reduction in setting time for GP-Cha compared to GP-0 is associated with the increased viscosity caused by the granular filler, reducing the liquid/solid fractions of the binder [47].

In the calorimetry results, the initial exothermic peaks observed in the first measurements (Figure 5.11(a)) indicate the partial dissolution of solid particles within the highly alkali solution. Subsequently, the appearance of the second exothermic peak (Figure 5.11(b)) indicates the formation of aluminosilicate species and the consolidation of a wider network [47]. The initial dissolution, as illustrated, was more intense in the presence of the three additions, even surpassing GP-0, possibly due to the synergistic action of the components: chamotte provides sites for deposition of geopolymerization products in addition to filling pores, NMK is more reactive than MK and CNT extend the setting time.

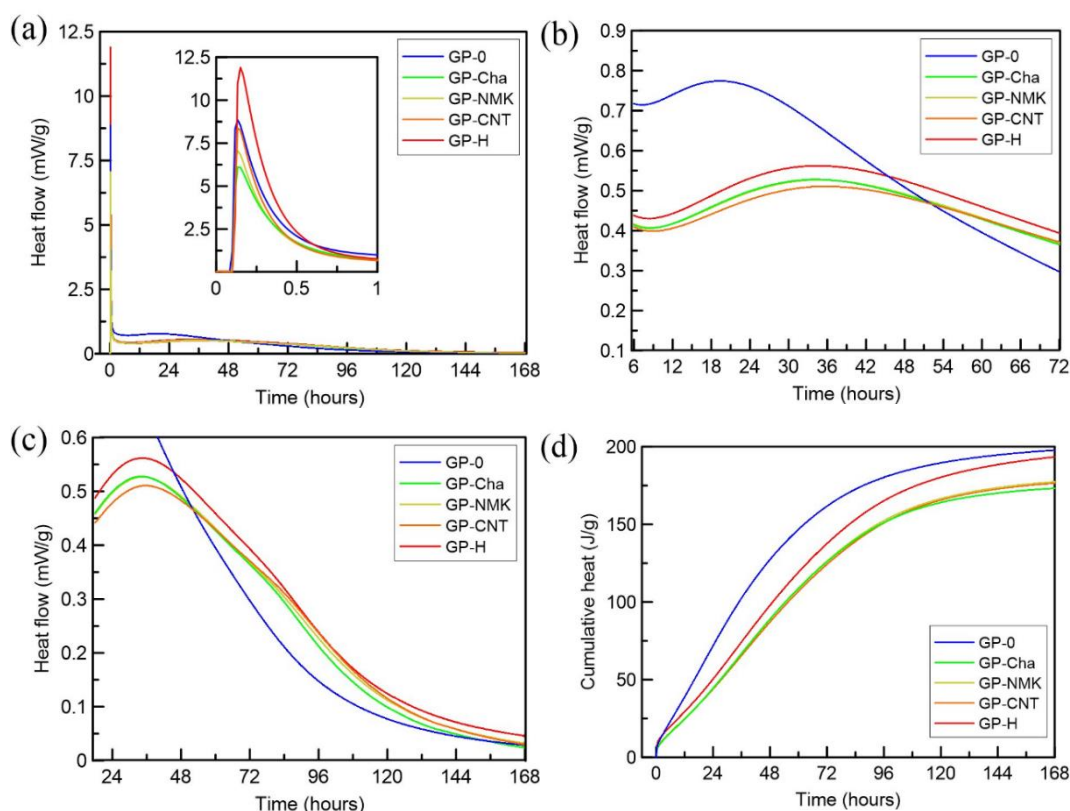


Figure 5.11 – (a) Heat flow of different geopolymer compositions as a function of curing time; (b) Polycondensation peak; (c) Heat flux between 1 and 7 days of curing; (d) Cumulative heat for all geopolymers design

5.3.2. Hardened properties

5.3.2.1. Additions effect

The improvement in compressive strength (Figure 5.12) can be attributed to the dense packing effect, leading to a reduction in both porosity and pore size (Table 5.11) [48]. When the porosity is reduced, more mass is available per unit area under similar loading conditions [49]. The inclusion of Chamotte70-G improved the performance of GP by increasing its thermal stability through crack deflection mechanisms [44], aided by the low coefficient of thermal expansion of this particle [16]. The early-age performance due to the addition of nanoclay-C was a result of its high surface area, small particle size and porous nature, enabling penetration, partial reactivity and increased interlocking with the geopolymer [27]. Additionally, nanoclay-C refines the pores (Figure 5.14) [36]. When tested in 1 day, GP-CNT specimens showed a plastic behavior, reducing by 50% of their original height,

related to their longer setting time. However, at 28 days, GP-CNT samples showed greater strength than GP-0 (Figure 5.12), suggesting excellent dispersion of MWCNTs in the GP [34], without any degradation of mechanical properties. The overall increase in compressive strength at 28 days across all variations may be attributed to the greater development of the geopolymer chain [30].

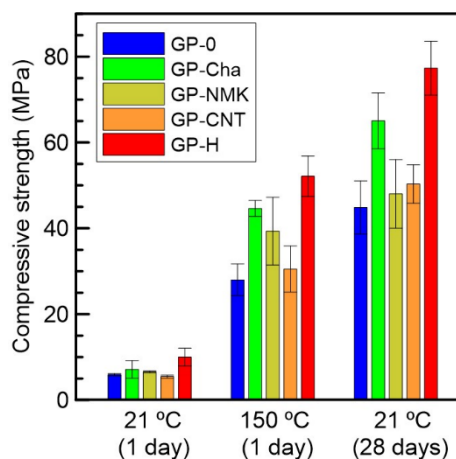


Figure 5.12 – Compressive strength values for different geopolymer formulations molded into 10 mm cubes cured under 21°C and 150°C, at atmospheric pressure.

The XRD results demonstrated that the MWCNTs preserved the amorphous structure of the geopolymer, even at a temperature of 150°C [38], with no significant difference compared to curing at 21°C for GP-0 sample (Figure 5.13(a)). For GP-0 (Figure 5.13(b)), a sharp peak around $2\theta=25^\circ$ is evident, referring to the titanium dioxide (impurity) present in MK [38]. Increasing the curing time from 1 to 28 days for GP-0 did not result in the formation of new reaction products, but a broadening of the peak around 28° suggests progressing reactions [12]. The XRD pattern of GP-H (Figure 5.13(c)) exhibits characteristics of an amorphous matrix with peaks referring to the crystalline particles (Chamotte70-G, Figure 5.3). Notably, there is no change in the general shape of the XRD curve due to the addition of particles, confirming that Chamotte70-G remained inert within the strongly alkaline matrix [8]. The smaller broadening of the peak for GP-H at 28 days compared to GP-0 at the same age indicates that the addition of NMK may have improved the matrix by enhancing geopolymerization and, consequently, increasing the amount of amorphous content [24]. The absence of crystalline product formation (Table 5.10) is closely related to higher compressive strength [5], as shown in Figure 5.12.

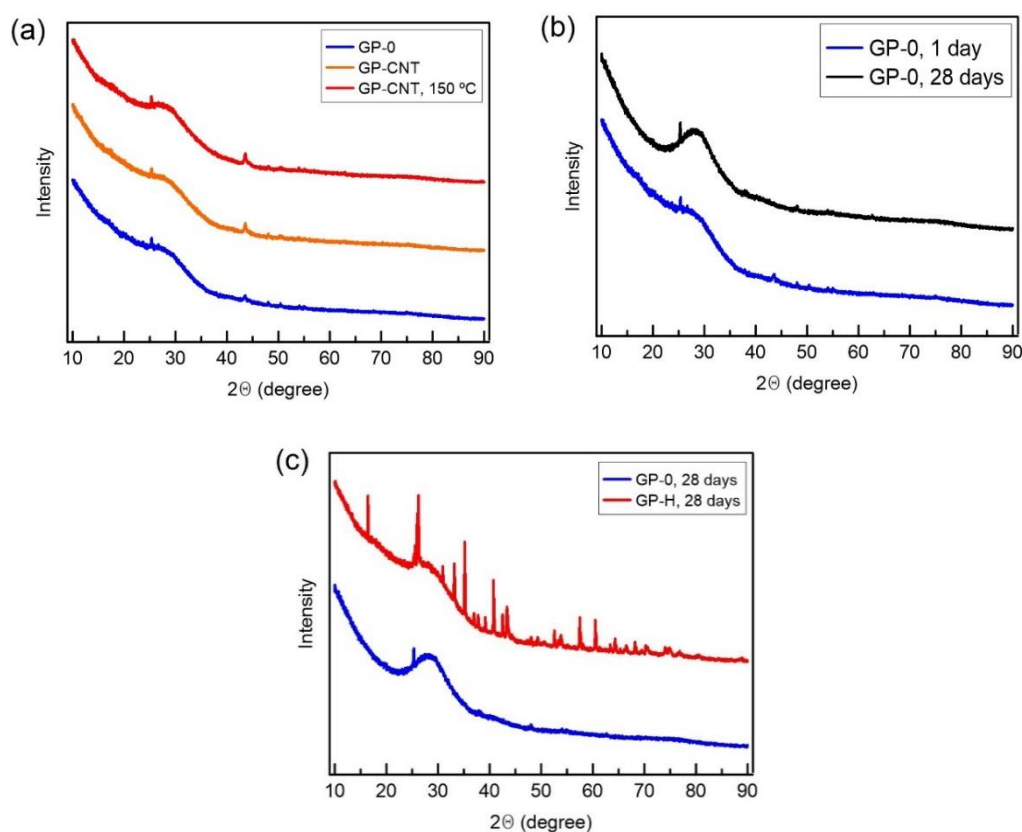


Figure 5.13 – XRD patterns for (a) GP-CNT cured at 21°C and 150°C, for 1 day; (b) GP-0 cured at 21°C for 1 and 28 days; (c) GP-0 and GP-H cured at 21°C for 28 days.

Table 5.10 – Mass distribution and lattice parameters of crystalline phases obtained by XRD analysis for GP-H cured at 21°C for 28 days.

% Mass		Crystallite Size (LVol IB) /nm		Lattice Parameters / Å				
C	M	C	M	C		M		
				a	c	a	b	c
29.7	70.3	102	203	4.76	13.00	7.58	7.70	2.89

C- corundum (Al_2O_3 , ICSD 9770); M – mullite ($\text{Al}_{5.33}\text{Si}_{0.67}\text{O}_{9.33}$, ICSD 66448).

All additions reduced porosity and average pore diameter (Table 5.11) for all curing temperatures analyzed. The additions facilitated the formation of pores predominantly smaller than 100 nm, regardless of the curing temperature (Figure 5.14). Each addition acted differently in reducing the size of the pores: chamotte acted as a filler controlling dehydration and as a barrier in the growth of cracks (mainly at a temperature of 150°C); NMK acted both as a more reactive aluminosilicate source and as a filler (due to its partially amorphous portion);

MWCNTs only acted as filler. A notable impact was observed at a temperature of 21°C for GP-CNT, resulting in a reduction in both porosity and average pore diameter, aligning with findings from Chen and Akono [38]. The influence of curing at 150°C on the increase in average pore size was more pronounced for GP-0. In general, the results of greater densification are well correlated with the values found for compressive strength (Figure 5.12).

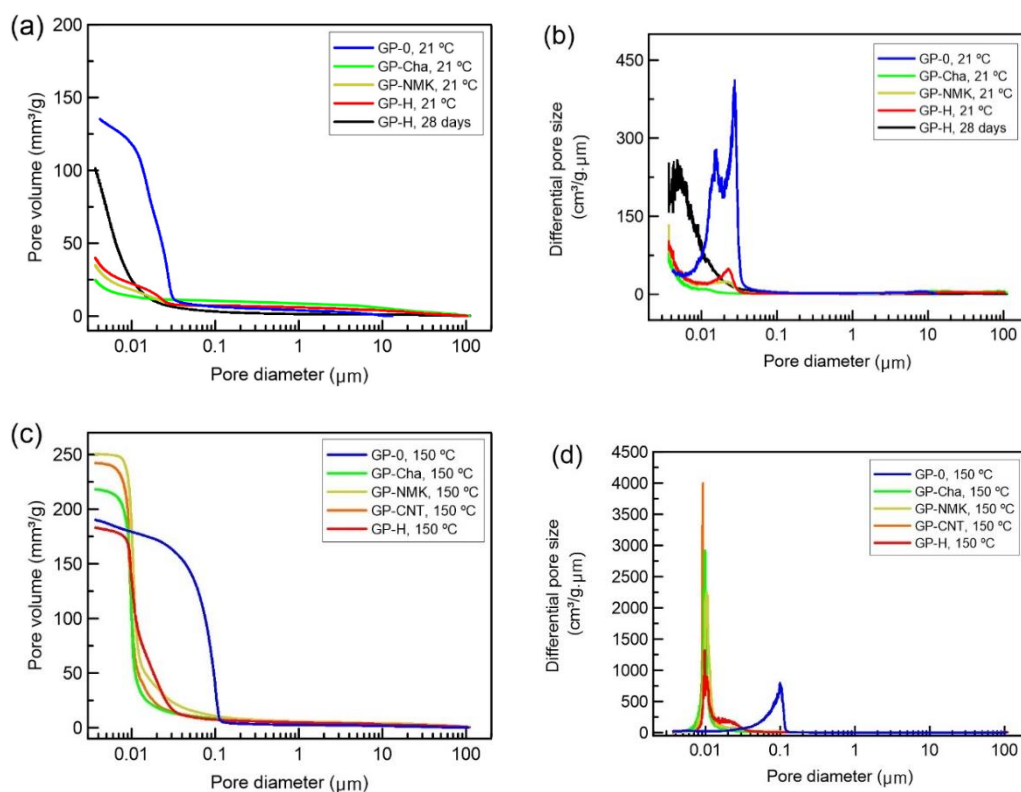


Figure 5.14 – (a) Cumulative pore volume and (b) pore size distribution for geopolymer cured for 1 day at 21°C, considering different geopolymer formulations; (c) Cumulative pore volume and (d) pore size distribution for geopolymer cured for 1 day at 150°C, considering different geopolymer formulations.

Table 5.11 – Porosity and mean pore diameter (d_{50}) for different geopolymer formulations cured at 21°C and 150°C for 1 day.

Sample	21°C		150°C	
	Porosity (%)	d_{50} (μm)	Porosity (%)	d_{50} (μm)
GP-0	22.97	0.019	58.84	0.078
GP-NMK	6.87	0.011	35.59	0.011
GP-Cha	5.29	0.014	34.57	0.010
GP-CNT	3.47	0.004	34.81	0.010
GP-H	8.19	0.013	30.1	0.012

5.3.2.2. Temperature effect

Initially, the flexural tests were scheduled to be carried out after 24 hours of curing at room temperature (21°C). However, GP-H exhibited a fresh appearance after this period, as discussed previously. Consequently, the curing time was extended to 7 days.

Flexural tests results (Figure 5.15) showed that GP is a quasi-brittle material characterized by a high crack growth rate [12, 45], with sudden brittle failure also observed during flexural testing on GP-H. The P-CMOD curve reveals four distinct stages: (1) Linear elastic region [11, 45]; (2) Initiation of deviation from linearity, as the crack starts at the tip of the notch due to the formation of the fracture processing zone (FPZ) [11, 45]; (3) Peak load occurrence, followed by a gradual loss in load-bearing capacity; (4) Rapid decline in load-bearing capacity, signaling instable crack propagation leading to ultimate causes rupture [45].

Crack propagation was swifter in the GP-0 samples, and the presence of branching in the post-peak region for GP-H suggests a slightly greater deformation capacity after cracking [11]. When observing the data in Table 5.12 alongside Figure 5.22, it is noted that K_{Ic} increases with higher compressive strength, consistent with literature [36, 50]. The fracture toughness value for GP-0 aligns with the value reported by Chen and Akono [38], which was $0.57 \text{ MPa}\cdot\sqrt{\text{m}}$. Higher K_{Ic} values indicate more tortuous failure planes due to greater energy consumption [36], a characteristic confirmed by visual inspection of the fracture surfaces (Figure

5.16).

The dehydration of the tested specimens, which caused the formation of cracks, was the primary cause for the decrease in flexural strength observed in GP-H cured at 150°C [16, 18]. This phenomenon was intense for GP-0 to the extent that the samples completely cracked after curing (Figure 5.16(c)), resulting in the complete loss of flexural strength. The changes in flexural strengths after exposure to 150°C partially followed the trend observed in compressive strength. In GP-H, the drop in strength was not significant as the particles mitigated the stresses caused by binder shrinkage [16].

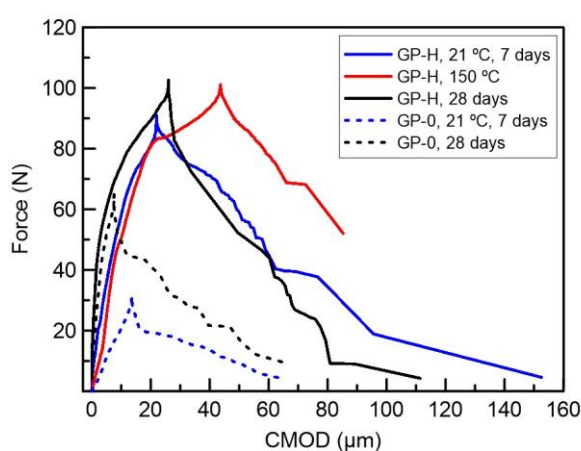


Figure 5.15 – Load x CMOD curves obtained by 3-point bending tests for plain geopolymer (GP-0) and geopolymer with hybrid additions (GP-H) cured at 21°C and 150°C.

Table 5.12 – Fracture toughness (K_{IC}) and flexural strength (σ_f) values obtained by 3-point bending tests for plain geopolymer (GP-0) and geopolymer with hybrid additions (GP-H).

Curing	GP-0		GP-H	
	K_{IC} (MPa. \sqrt{m})	σ_f (MPa)	K_{IC} (MPa. \sqrt{m})	σ_f (MPa. \sqrt{m})
21°C, 7 days	0.43	0.18	1.24	0.53
150°C, 1 day	-	-	1.17	0.50
21°C, 28 days	0.89	0.38	1.40	0.60

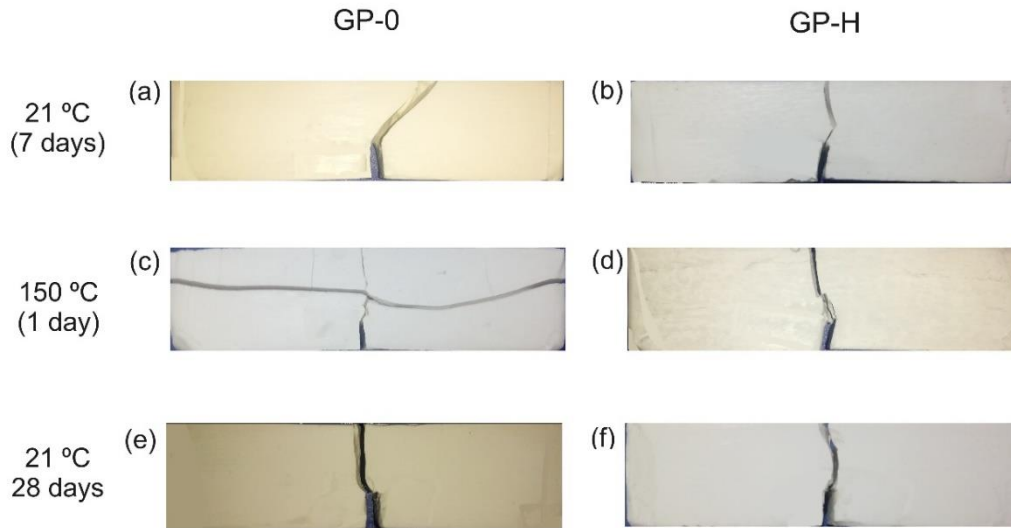


Figure 5.16 – Samples after subjected to 3-point bending tests: (a) GP-0 and (b) GP-H, cured at 21°C for 7 days; (c) GP-0 (cracked completely during curing) and (d) GP-H, cured at 150°C for 1 day; (e) GP-0 and (f) GP-H, cured at 21°C for 28 days.

Despite the impressive mechanical performance, there is an increase in the accumulated pore volume when cured at 150°C (Figure 5.17 and Table 5.11). For the same type of GP, the rise in porosity in temperature cured specimens are attributed to accelerated geopolymerization, excess water removal and dehydroxylation [49]. For GP-H, the lower porosity compared to GP-0 under the same curing conditions is due of both the filling effect and shrinkage control. The pores generated at 150°C are due to excessive water evaporation [51], leading to voids left by the released water [17]. Nevertheless, GP-H maintained its nanoporous characteristics at 150°C, distinguishing it from GP-0.

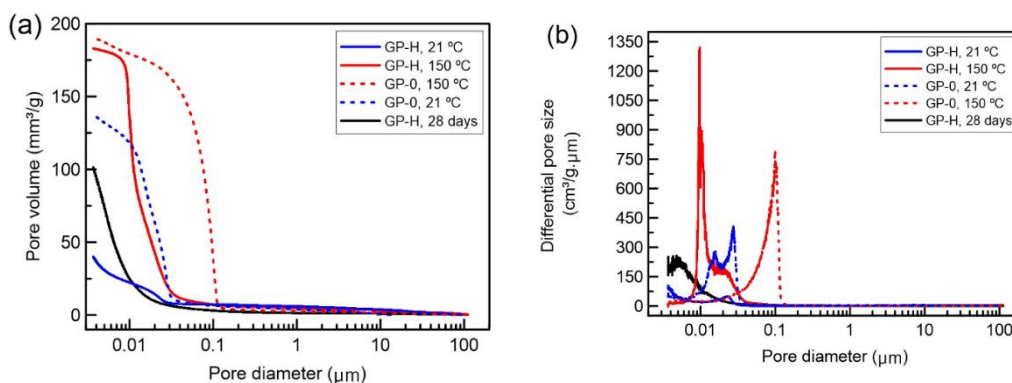


Figure 5.17 – (a) Cumulative pore volume and (b) pore size distribution for GP-0 and GP-H cured at 21°C and 150°C.

The TGA (Figure 5.18(a)) exhibited similar curve shapes, signifying the decomposition of the same products, despite whether it was GP-0 or GP-H, both cured under the same conditions [35]. The DTG curves (Figure 5.18(b)) of GP-0 showed a more substantial weight loss from room temperature to 150°C, attributed to the evaporation of physically adsorbed water. The peaks in this range are sharper for GP-0 and occur at lower temperatures compared to GP-H, reflecting the higher porosity values of GP-0, which diminishes ability to retain water. Between 150°C and 300°C, the rate of weight loss for all samples began to diminish as all physically adsorbed free water evaporated and the pore water began to decompose [24].

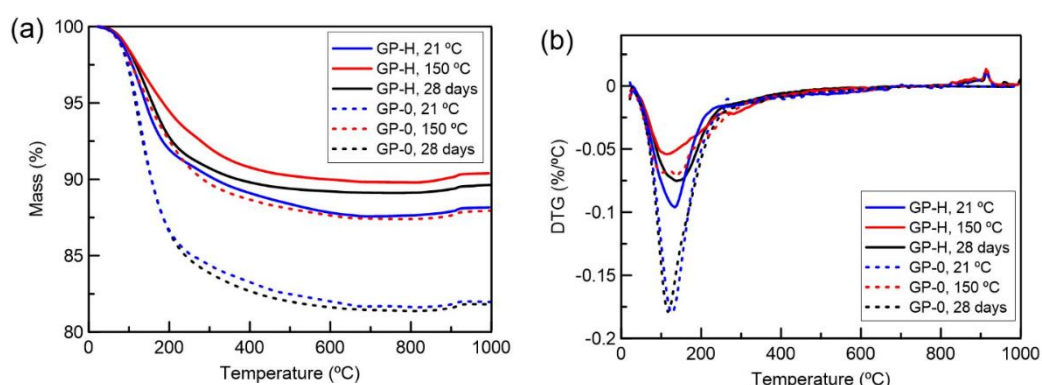


Figure 5.18 – (a) TGA and (b) DTG curves for geopolymer cured for GP-0 and GP-H cured at 21°C and 150°C for 1 day.

5.3.2.3. Pressure effect

The GP-H specimens showed the same plastic behavior as the 10 mm cubic GP-CNT samples. This result clearly demonstrates the effect of MWCNT on the GP setting time, although it does not align with the results of the Vicat test for GP-H (Table 5.9), which presented a faster setting than GP-0. Therefore, it was decided to extend the curing time to 7 days for curing with and without pressure.

Curing GP-H under a pressure of 40 MPa showed a decrease in the compressive strength value compared to plain GP (Figure 5.19). The deterioration of compressive strength in GP-H may be attributed to two reasons: 1) the generation of a porous ITZ between the Chamotte70-G particles and the GP matrix due to the high-pressure intensity; 2) a greater intensity of alkali solution removal, reducing the growth of the geopolymer chain.

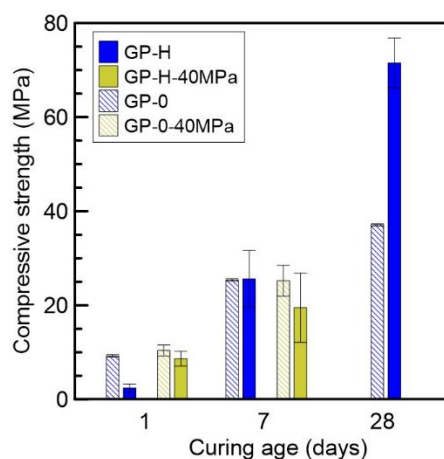


Figure 5.19 – Compressive strength for 21°C and 40 MPa for plain geopolymer (GP-0) and geopolymer with hybrid additions (GP-H).

GP-0 and GP-H exhibit a bimodal pore distribution centered at approximately the same value for curing at 40 MPa (Figure 5.20). However, GP-H has a smaller pore volume (Table 5.13). One possible reason for this could be the filling effect of the nanoparticles in GP-H. Curing under high pressure can increase porosity due to two effects: a greater flow of the alkali solution, resulting in more internal pores, and a significant increase in the volume of microcracks [19].

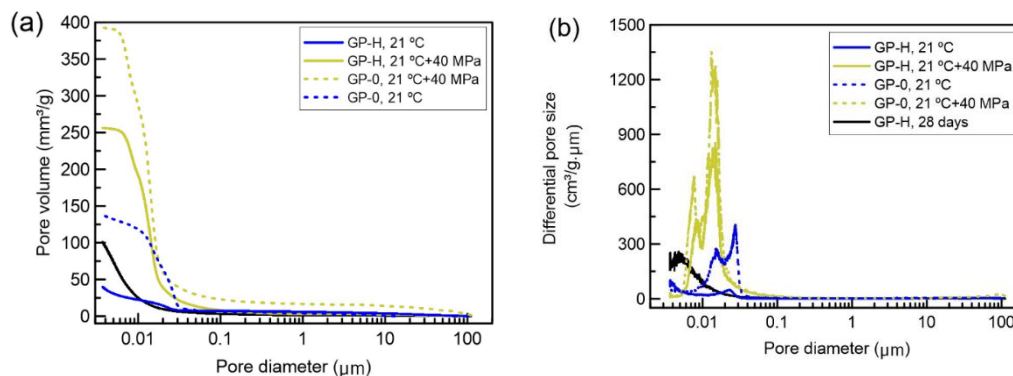


Figure 5.20 – (a) Cumulative pore volume and (b) pore size distribution for GP-0 and GP-H cured at 21°C and 40 MPa.

Table 5.13 – Porosity and mean pore diameter (d_{50}) for GP-0 and GP-H cured at 21°C and 40 MPa.

Sample	21°C		21°C + 40 MPa	
	Porosity (%)	d_{50} (µm)	Porosity (%)	d_{50} (µm)
GP-0	22.97	0.019	46.84	0.013
GP-H	8.19	0.013	33.85	0.012

In the TGA curve (Figure 5.21(a)), the weight loss between 50°C and 200°C is related to the dehydration of the geopolymeric structures [52]. In the DTG curve (Figure 5.21(b)), all samples present peaks centered at around 105°C, related to the evaporation of free water, and from this temperature up to 250°C refers to the loss of adsorbed and weakly bound water. For samples cured at 21°C, GP-H demonstrates greater thermal stability after dehydration and dehydroxylation, probably as a result of Chamotte70-G acting to control shrinkage [2]. However, for samples cured at a pressure of 40 MPa, the thermal stability after 250°C is similar for GP-0 and GP-H, which may indicate that good adhesion between Chamotte-70G and GP matrix was not ensured under this pressure.

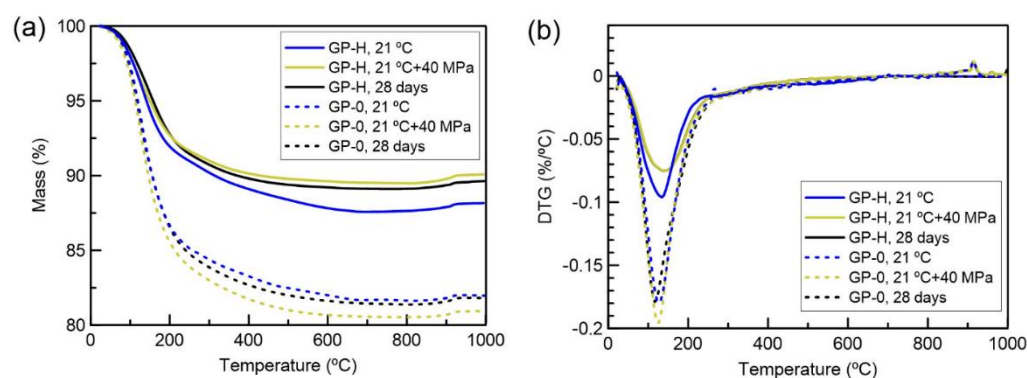


Figure 5.21 – (a) TGA and (b) DTG curves for geopolymer cured for GP-0 and GP-H cured at 21°C and 40 MPa.

5.3.2.4. Combination of temperature and pressure effects

A significant decrease in the compressive strength of GP-0 was observed after exposure to 150°C (Figure 5.22). One of the possible causes is the dehydration of the GP [18]. On the other hand, GP-H presents a significantly higher compressive strength compared to the plain sample, which may be a result of the lower proportion of water in the geopolymer paste [46], causing a limiting the effect of shrinkage when forming the supporting network [3].

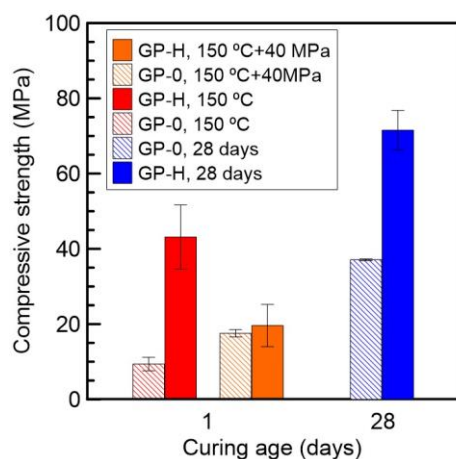


Figure 5.22 – Compressive strength for GP-0 and GP-H molded into 50.8 mm cubes cured at 150°C and 40 MPa.

Another important point to highlight is that when comparing the results in Figure 5.22 with those in Figure 5.12, for curing at 150°C, an increase in specimens dimension led to a decreasing trend in the compressive strength [46]. This phenomenon may occur because the outer regions of the samples, which dry first, shrink before the interior, creating tensile stresses near the surface. Therefore, larger samples experience higher drying gradients introducing more microcracks [3].

For curing at 150°C and 40 MPa, GP-0 and GP-H did not show significant differences in compressive strength values. In this case, the particulate reinforcement may not have been effective due to the high curing pressure, and the concentration of nanoparticles may have been insufficient to densify the ITZ, especially the nanoclay-C, while the amount of MWCNT is insufficient to act as a crack bridging tool.

It is also noteworthy that the higher standard deviation values for GP-H compared to its GP-0 counterparts, when cured at 150°C regardless of pressure, can be attributed to the formation of microcracks around non-shrinkable chamotte70-G particles [3].

Although the average pore size decreased when cured at 40 MPa (Figure 5.23), the volume of microcracks significantly increased, with curing at 150°C further aggravates this situation, [19] deteriorating the final compressive strength value (Figure 5.22). While porosity reduced under pressure, the average pore size increased, probably due to a greater presence of microcracks. The imposition of temperature led to a monomodal pore distribution, but with a smaller mean pore

size for GP-H. The larger pore size in GP-0 is attributed to the higher proportion of water in the starting mixture [14]. The pore size distribution obtained for 150°C + 40 MPa is the same for GP-0 and GP-H (Figure 5.23(b)), indicating the values obtained for GP-H pertain to the intrinsic porosity of the geopolymer matrix [14], at this pressure level.

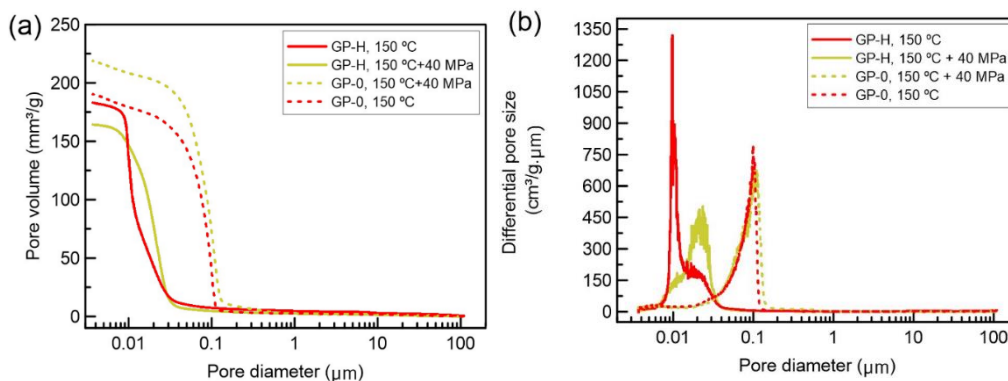


Figure 5.23 – (a) Cumulative pore volume and (b) pore size distribution for GP-0 and GP-H cured at 150°C and 40 MPa.

In the TGA curve (Figure 5.24(a)), the apparent increase in mass about 900 °C may result from structural reorganization [2]. As shown in the DTG curve (Figure 5.24(b)), the curing pressure of 40 MPa resulted in less entrapment of free water in the structure of GP-0 [12]. However, for GP-H, there was virtually no difference between the DTG curves when applying pressure, suggesting that at this pressure level, Chamotte70-G was not an effective reinforcement. Both GP-0 and GP-H lose dimensional stability at around 800°C [12]. Thus, the temperature of 150°C acts only to evaporate part of the free water, while the pressure increases the compressibility of the matrix [53]. The greater compressibility of the matrix in GP-H compared to the Chamotte70-G particles may be one of the reasons for this ineffectiveness of this reinforcement under a curing pressure of 40 MPa.

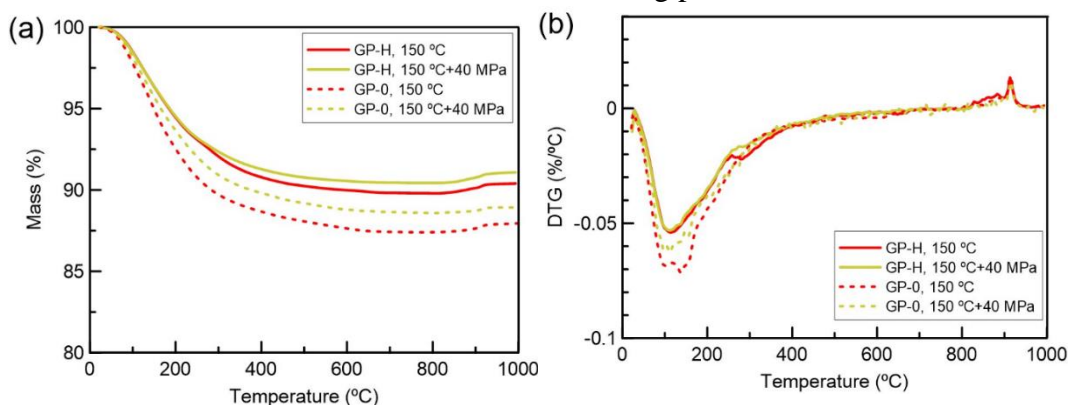


Figure 5.24 – (a) TGA and (b) DTG curves for GP-0 and GP-H cured at 150°C and 40 MPa.

5.3.3. Microstructure

The geopolymerization products represent a heterogeneous material, containing both completely reacted, partially reacted and unreacted particles, as well as pores [5, 52] (Figure 5.25). The structure of the material was less defective after autoclave treatment (Figure 5.25(b)) [54]. Curing under 40 MPa made the particulate structure [19] more evident, forming a condensed microstructure [53].

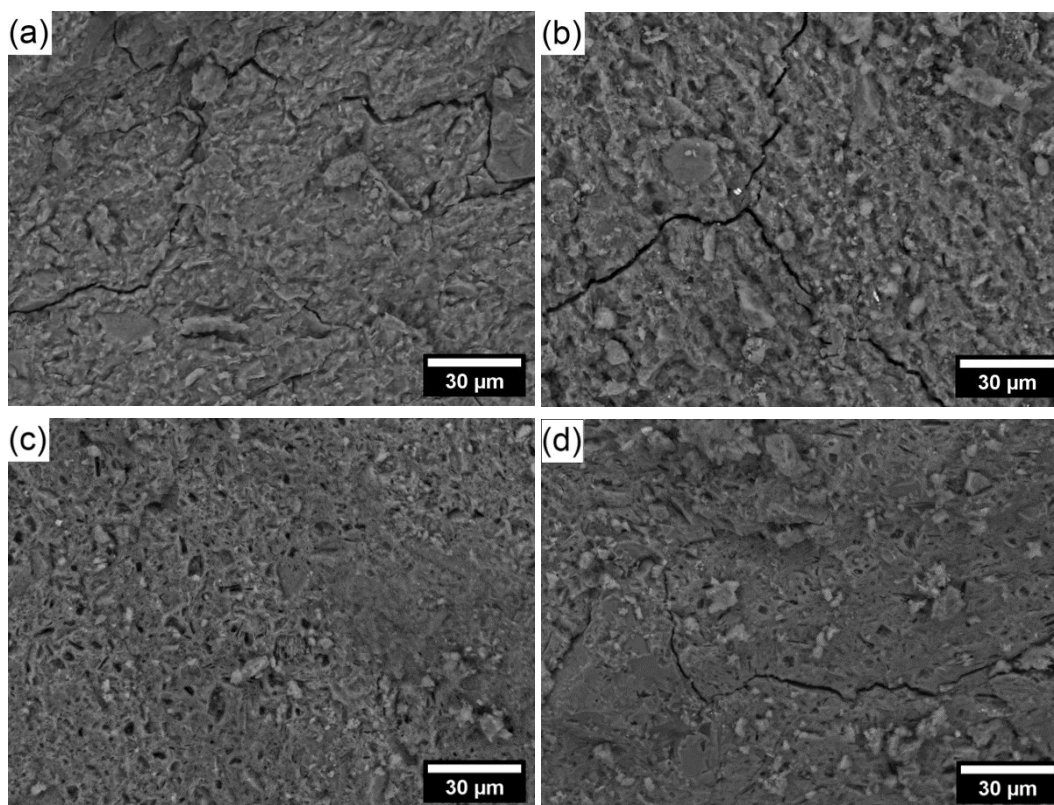


Figure 5.25 – Microstructure of geopolymer with hybrid additions (GP-H) samples cured at (a) 21°C; (b) 40 MPa; (c) 150°C; (d) 21°C (28 days).

A significant change in the microstructure was evident upon curing at 150°C (Figure 5.25(c)). Although pores are evident, the structure appears relatively uniform, indicating a high presence of reacted particles, suggesting that geopolymerization was significantly improved at an early age. This result may be attributed to the nucleation and paper-filling effect of nanoclay [12], which, combined with chamotte70-G, ensured better mechanical behavior compared to GP-0 for the same curing temperature. With the increase in curing time at 21°C, a greater quantity of reacted particles became evident (Figure 5.25(d)), resulting in a densely packed microstructure due to increased dissolution of MK in a highly alkali

solution [8].

5.4. Conclusions

The challenge of dispersing carbon nanotubes for use as reinforcement in geopolymers was overcome using a simple, low-energy technique by selecting functionalized multi-walled carbon nanotubes for dispersion in a strongly alkali solution.

All additions individually contributed to the improvement in the performance of the plain geopolymer. Each addition acted in reducing pore size: chamotte acted as a filler and also in controlling dehydration, nano-metakaolin acted both as a more reactive aluminosilicate source and as a filler (due to its amorphous portion) and carbon nanotubes acted as filler and may have provided new reaction sites due to its high surface energy. The results of greater densification are well correlated with the values found for compressive strength.

However, the effect of the hybrid additions surpassed any separate addition, where the components acted synergistically due to its different functions in the matrix. After curing at 150°C, the GP with hybrid additions significantly enhanced mechanical properties in the order of 350%, compared to plain GP at the same temperature. When subjected to a pressure of 40 MPa, the mechanical performance was minimally affected by the use of hybrid additions.

Overall, the hybrid additions led to pore refinement, increased flexural strength and reduced porosity compared to the single-reinforced samples cured under similar conditions. The results confirm the feasibility of nanoparticles in metakaolin-based geopolymers with the properties required for high-temperature and pressure applications.

5.5. References

1. Musil, S.S., Kriven. W.M. (2014). In Situ Mechanical Properties of Chamotte Particulate Reinforced, Potassium Geopolymer. *J. Am. Ceram. Soc.*, 97 [3] 907–915.
2. Kamseu, E., Rizzuti, A., Leonelli, C., Perera, D. (2010). Enhanced thermal stability in K₂O-metakaolin-based geopolymer concretes by Al₂O₃ and SiO₂ fillers addition. *J Mater Sci* 45. 1715–1724.
3. Kuenzel, C., Li, L., Vandeperre, L., Boccaccini, A.R., Cheeseman, C.R. (2014). Influence of sand on the mechanical properties of metakaolin geopolymers. *Construction and Building Materials* 66. 442–446.

4. Brandvold, A.S., Trindade, A.C.C., Kriven, W.M. (2023). Rheological assessment of metakaolin-based geopolymer composites through squeeze flow. *Journal of the American Ceramic Society*. pp. 4038-4051.
5. Komljenovic, M., Bascarevi, Z., Bradi, V. (2010). Mechanical and microstructural properties of alkali-activated fly ash geopolymers. *Journal of Hazardous Materials* 181. 35-42.
6. Sun, Z., Lin, X., Vollpracht, A. (2018). Pervious concrete made of alkali activated slag and geopolymers. *Construction and Building Materials* 189. 797–803.
7. Kolousek, D., Brus, J., Urbanova, M., Andertova, J., Hulinsky, V., Vorel, J. (2007). Preparation, structure and hydrothermal stability of alternative (sodium silicate-free) geopolymers. *J Mater Sci* 42. 9267–9275.
8. Xiang, J., Liu, L., Cui, X., He, Y., Zheng, G., Shi, C. (2019). Effect of Fuller-fine sand on rheological, drying shrinkage, and microstructural properties of metakaolin-based geopolymer grouting materials. *Cement and Concrete Composites* 104.
9. Muzek, M.N., Zelic, J., Jozic, D. (2012). Microstructural Characteristics of Geopolymers Based on Alkali-Activated Fly Ash. *Chem. Biochem. Eng. Q.* 26 (2). 89–95.
10. Brandão, D., Borges, P.H.R., Ludvig, P., Colão, M. (2023). Geopolymers based on Metakaolin reinforced with Carbon Nanotubes. *Research Square*.
11. Ding, Y., Shi, C-J., Li, N. (2018). Fracture properties of slag/fly ash-based geopolymer concrete cured in ambient temperature. *Construction and Building Materials* 190. 787–795.
12. John, S.K., Nadir, Y., Cascardi, A., Arif, M.M., Girija, K. (2023). Effect of addition of nanoclay and SBR latex on fly ash-slag geopolymer mortar. *Journal of Building Engineering* 66.
13. Panchmatia, P., Olvera, R., Genedy, M., Juenger, M.C.G., Oort, E. (2020). Shrinkage behavior of Portland and geopolymer cements at elevated temperature and pressure. *Journal of Petroleum Science and Engineering* 195.
14. Papa, E., Medri, V., Amari, S., Manaud, J., Benito, P., Vaccari, A., Landi, E. (2018). Zeolite-geopolymer composite materials: Production and characterization. *Journal of Cleaner Production*, 171, 76-84.
15. Saafi, M., Andrew, K., Tang, P.L., McGhon, D., Taylor, S., Rahman, M., Yang, S., Zhou, X. (2013). Multifunctional properties of carbon nanotube/fly ash geopolymeric nanocomposites. *Construction and Building Materials* 49. 46-55.
16. Rovnanik, P., Safrankova, K. (2016). Thermal Behaviour of Metakaolin/Fly Ash Geopolymers with Chamotte Aggregate. *Materials* 2016, 9, 535.
17. Junaid, M.T., Kayalli, O. (2017). Response of alkali activated low calcium fly-ash based geopolymer concrete under compressive load at elevated temperatures. *Materials and Structures*. 50:50.
18. Kohout, J., Koutník, P., Hájková, P., Kohoutová, E., Soukup, A. (2022). Effect of Different Types of Aluminosilicates on the Thermo-Mechanical Properties of Metakaolinite-Based Geopolymer Composites. *Polymers* 2022, 14, 4838.

19. Bai, Y., Guo, W., Wang, J., Xu, Z., Wang, S., Zhao, Q., Zhou, J. (2022). Geopolymer bricks prepared by MSWI fly ash and other solid wastes: Moulding pressure and curing method optimisation. *Chemosphere*, 307.
20. Mathew, G., Joseph, B. (2018). Flexural behaviour of geopolymer concrete beams exposed to elevated temperatures. *Journal of Building Engineering* 15. 311–317.
21. Ikechukwu, A.F., Chibuzor, O.K. (2022). Improving resilient modulus and cyclic crack restriction of preloaded expansive subgrade treated with nano-geopolymer Binder. *Arabian Journal of Geosciences* 15:1340.
22. Samantasinghar, S., Singh, S. (2020). Effects of curing environment on strength and microstructure of alkali-activated fly ash-slag binder. *Construction and Building Materials*, 235.
23. Abdalla, J.A., Thomas, B.S., Hawileh, R.A., Yang, J., Jindal, B.B., Ariyachandra, E. (2022). Influence of nano-TiO₂, nano-Fe₂O₃, nanoclay and nano-CaCO₃ on the properties of cement/geopolymer concrete. *Cleaner Materials* 4.
24. McCoy, M., Betts, J., Norris, A., Saafi, M. Nanotechnology In Construction: Nano Materials And Devices Offer Macro Improvements In Concrete Materials.
25. Sanchez, F., Sobolev, K. (2010). Nanotechnology in concrete – A review. *Construction and Building Materials* 24. 2060–2071.
26. Wang, D-h., Yao, X., Yang, T., Xiang, W-r., Feng, Y-t., Chen, Y. (2021). Controlling the early-age hydration heat release of cement paste for deep-water oil well cementing: A new composite designing approach. *Construction and Building Materials* 285.
27. Ameri, F., Shoaie, P., Zareei, S.A., Behforouz, B. (2019). Geopolymers vs. alkali-activated materials (AAMs): A comparative study on durability, microstructure, and resistance to elevated temperatures of lightweight mortars. *Construction and Building Materials* 222. 49–63.
28. Ravitheja, A., Kumar, N.L.N.K. (2019). A study on the effect of nano clay and GGBS on the strength Properties of fly ash based geopolymers. *Materials Today: Proceedings* 19. 273–276.
29. Rabiaa, E., Mohamed, R. A. S., Sofi, W. H., Tawfik, T.A. (2020). Developing Geopolymer Concrete Properties by Using Nanomaterials and Steel Fibers. *Advances in Materials Science and Engineering*.
30. Khater, H.M., Abd el Gawaad, H.A. (2016). Characterization of alkali activated geopolymer mortar doped with MWCNT. *Construction and Building Materials* 102. 329–337.
31. Assaedi, H., Shaikh, F.U.A., Low, I.M. (2016). Effect of nano-clay on mechanical and thermal Properties of geopolymer. *Journal of Asian Ceramic Societies* 4. 19–28.
32. Davoodabadi, M., Vareli, I., Liebscher, M., Tzounis, L., Sgarzi, M., Paipetis, A.S., Yang, J., Cuniberti, G., Mechtcherine, V. (2021). Thermoelectric Energy Harvesting from Single-Walled Carbon Nanotube Alkali-Activated Nanocomposites Produced from Industrial Waste Materials. *Nanomaterials* 2021, 11, 1095.
33. Rocha, V.V., Ludvig, P., Trindade, A.C.C., Silva, F.A. (2019). The influence of carbon nanotubes on the fracture energy, flexural and tensile behavior of cement-based composites. *Construction and Building Materials* 209.

34. Davoodabadi, M., Liebscher, M., Hampel, S., Sgarzi, M., Rezaie, A.B., Wolf, D., Cuniberti, G., Mechtcherine, V., Yang, J. (2021). Multi-walled carbon nanotube dispersion methodologies in alkaline media and their influence on mechanical reinforcement of alkali-activated nanocomposites. *Composites Part B* 209.
35. Rocha, V.V., Ludvig, P. (2020). Influence of Carbon Nanotubes on the Mechanical Behavior and Porosity of Cement Pastes Prepared by A Dispersion on Cement Particles in Isopropanol Suspension. *Materials* 2020, 13, 3164.
36. Malik, M.A., , Sarkar, M., Xu, S., Li, Q. (2019). Effect of PVA/SiO₂ NPs Additive on the Structural, Durability, and Fire Resistance Properties of Geopolymers. *Appl. Sci.* 2019, 9, 1953.
37. Joshi, A., Montes, C., Salehi, S., Allouche, E., Lvov, Y. (2015). Optimization of Geopolymer Properties by Coating of Fly-Ash Microparticles with Nanoclays. *J Inorg Organomet Polym* 25. 282–292.
38. Chen, J., Akono, A-T. (2021). Influence of multi-walled carbon nanotubes on the fracture response and phase distribution of metakaolin-based potassium geopolymers. *J Mater Sci* 56. 19403–19424.
39. Lu, S-N., Xie, N., Feng, L-C., Zhong, J. (2015). Applications of Nanostructured Carbon Materials in Constructions: The State of the Art. *Journal of Nanomaterials*.
40. Guades, E.J. (2016). Experimental investigation of the compressive and tensile strengths of geopolymer mortar: The effect of sand/fly ash (S/FA) ratio. *Construction and Building Materials* 127. 484–493.
41. Schneider, K., Michel, A., Liebscher, M., Terreri, L., Hempel, S., Mechtcherine, V. (2019). Mineral-impregnated carbon fibre reinforcement for high temperature resistance of thin-walled concrete structures. *Cement and Concrete Composites* 97. 68–77.
42. Brandvold, A.S., Al-Chaar, G.K., Kriven, W.M. (2023). Isolating the effects of thixotropy in geopolymer pastes. *Journal of the American Ceramic Society*. pp. 2797-2807.
43. Siciliano, U.C.C.S., Zhao, J., Trindade, A.C.C., Liebscher, M., Mechtcherine, V., Silva, F.A. Influence of Curing Temperature and Pressure on the Mechanical and Microstructural Development of Metakaolin-based Geopolymers. Submitted to **Construction & Building Materials** on October 24, 2023.
44. Trindade, A. C. C.; Mcnutt, P.; Sood, S. S.; Brandvold, A.; Ozer, A.; Kriven, W. M. (2023). Optimizing the Design Parameters for Chamotte Particle-Reinforced Geopolymers. *JOURNAL OF THE AMERICAN CERAMIC SOCIETY*.
45. Xie, Z.L., Zhou, H.F., Lu, L.J., Chen, Z.A. (2017). An investigation into fracture behavior of geopolymer concrete with digital image correlation technique. *Construction and Building Materials* 155. 371–380.
46. Hamidi, F., Aslani, F., Valizadeh, A. (2020). Compressive and tensile strength fracture models for Heavyweight geopolymer concrete. *Engineering Fracture Mechanics* 231.
47. Kovarik, T., Kullova, L., Rieger, D. (2016). Production of refractory chamotte particle-reinforced geopolymer composite. *IOP Conf. Series: Materials Science and Engineering* 123.

48. Peng, Y., Hu, S., Ding, Q. (2009). Dense packing properties of mineral admixtures in cementitious material. *Particuology* 7. 399–402.
49. Ahmad, M., Rashid, K., Hameed, R., Haq, E. U., Farooq, H., Ju, M. (2022). Physico-mechanical performance of fly ash based geopolymer brick: Influence of pressure - temperature – time. *Journal of Building Engineering*, 50.
50. Sarker, P.K., Haque, R., Ramgolam, K.V. (2013). Fracture behaviour of heat cured fly ash based geopolymer concrete. *Materials and Design* 44. 580–586.
51. Zhao, J., Liebscher, M., Michel, A., Junger, D., Trindade, A.C.C., Silva, F.A., Mechtcherine, V. (2021). Development and testing of fast curing, mineral-impregnated carbon fiber (MCF) reinforcements based on metakaolin-made geopolymers. *Cement and Concrete Composites*, 116.
52. Trindade, A. C. C., Silva, F. A., Alcamandb, H. A., Borges, P. H. R. (2017). On The Mechanical Behavior of Metakaolin Based Geopolymers Under Elevated Temperatures. *Materials Research*, 20(Suppl. 2): 265-272.
53. Ranjbar, N., Kashefi, A., Ye, G., Mehrali, M. (2020). Effects of heat and pressure on hot-pressed geopolymer. *Construction and Building Materials*, 231.
54. Hoang, M.D., Do, Q.M., Le, V.Q. (2020). Effect of curing regime on properties of red mud-based alkali activated materials. *Construction and Building Materials*, 259.

6. Conclusions and Suggestions for Future Works

6.1. Conclusions

This investigation underscores the pivotal role played by $\text{SiO}_2/\text{K}_2\text{O}$ and $\text{H}_2\text{O}/\text{K}_2\text{O}$ molar ratios in the geopolymerization process and early-age strength development. Isothermal calorimetry effectively tracked the geopolymerization progress, while pH measurements demonstrated excellent water resistance and limited leaching through a diffusion mechanism. The total heat released aligned consistently with strength evolution, as monitored by an ultrasonic cement analyzer ($R^2=0.99$), emphasizing the direct correlation between polycondensation and strength gain in metakaolin-based geopolymers.

Furthermore, the ultrasonic cement analyzer confirmed that thermal curing significantly reduces setting time and accelerates early-age strength development. Conversely, the application of external pressure enhanced material reorganization, promoting microstructural compaction and subsequent mechanical property enhancement. Curing pressures of up to 20 MPa demonstrated notable benefits, highlighting the combined influence of pressure and temperature in shaping the physiochemical properties of geopolymers and fostering strength gain.

Addressing the challenge of dispersing carbon nanotubes as reinforcement in geopolymers, a simple, low-energy technique using functionalized multi-walled carbon nanotubes for dispersion in a strongly alkali solution proved effective. Each addition (chamotte, nanoclay and carbon nanotubes) contributed to reducing pore size, with the hybrid additions surpassing the effects of individual reinforcements. Synergistic interactions among components led to pore refinement, increased flexural strength, and reduced porosity compared to the single-reinforced samples under similar curing conditions.

In summary, this study significantly advances knowledge in pressurized thermal curing for rapidly setting geopolymers, providing valuable insights for tailoring geopolymer material design and offering a diverse spectrum of mechanical properties

6.2. Suggestions for future works

Geopolymers are promising for various applications, such as: oil well cementing, brick production, high-tech ceramic sintering and repair materials, offering a potential alternative to conventional materials. However, before widespread application, dedicated research is needed to understand some properties of the geopolymer. The following research suggestions are proposed:

- Assessment of geopolymer slurry in terms of rheological properties;
- Evaluate the effect of nanoparticle concentration on shrinkage (autogenous and drying) and creep behavior;
- Investigate the adhesion properties;
- Evaluate durability in a CO₂ environment, curing under pressure and temperature.